RAPID EVALUATION OF PATHOLOGY USING NONLINEAR MICROSCOPY WITH APPLICATIONS IN BREAST CANCER, PROSTATE CANCER, AND RENAL DISEASE

by

Lucas C. Cahill

BASc Engineering Physics
University of British Columbia, 2015

SUBMITTED TO
THE HARVARD-MIT PROGRAM IN HEALTH SCIENCES AND TECHNOLOGY,
IN PARTIAL FULFILLMENT OF THE REQUIREMENTS
FOR THE DEGREE OF

DOCTOR OF PHILOSOPHY IN MEDICAL ENGINEERING AND MEDICAL PHYSICS
AT THE
MASSACHUSETTS INSTITUTE OF TECHNOLOGY

June 2021

Signature of Author: _____
Harvard-MIT Program in Health Sciences and Technology
May 18, 2021

Certified by:_____
James G. Fujimoto, PhD
Elihu Thomson Professor of Electrical Engineering
Thesis Supervisor

Accepted by: _____
Emery N. Brown, MD, PhD
Director, Harvard-MIT Program in Health Sciences and Technology
Professor of Computational Neuroscience and Health Sciences and Technology

Rapid evaluation of pathology using nonlinear microscopy with applications in

breast cancer, prostate cancer, and renal disease

by

Lucas C. Cahill

Submitted to the Harvard-MIT Program in Health Sciences and Technology
on May 18, 2021 in Partial Fulfillment of the
Requirements for the Degree of Doctor of Philosophy in
Medical Engineering and Medical Physics

Abstract

Frozen section analysis (FSA) is used intraoperatively for rapid evaluation of surgical tissue. In FSA, excised tissue is rapidly frozen, sectioned using a microtome, stained with hematoxylin and eosin (H&E), and evaluated by a pathologist. FSA requires ~20 minutes for the first specimen to be evaluated and the specimen size is limited by the equipment and personnel available. In some tissues that have a high lipid content (such as breast), freezing is difficult and adds artifacts that can affect interpretation. Techniques that enable fresh surgical specimen evaluation without freezing or microtoming can reduce the time and labor required for intraoperative tissue analysis. Nonlinear microscopy (NLM) is a fluorescence microscopy technique that provides subcellular resolution images of tissue using a femtosecond laser to excite fluorescence at the laser focus. Tissue does not need to be microtomed enabling visualization of freshly excised tissue. Exogenous fluorophores can be used to visualize cellular components such as nuclei and cytoplasm/stroma and multiple specimens can be stained in parallel without the restrictions of tissue size associated with FSA. NLM could dramatically reduce the time required for tissue evaluation compared with FSA.

In this thesis, we developed and validated NLM evaluation techniques for breast and prostate cancer and renal disease. The studies in this thesis were performed in close collaboration with the Beth Israel Deaconess Center. We developed a rapid, robust fluorescent staining protocol for NLM imaging with a compact, low cost ytterbium laser and validate it on fresh breast tissue. A randomized controlled trial was designed and initiated to assess the rate of indication for repeat breast surgeries in a study group of patients receiving intraoperative NLM evaluation vs a control group of patients receiving no intraoperative evaluation. We also developed techniques for NLM evaluation of fresh prostatectomy tissue and prostate biopsies and performed blinded readings of NLM images to assess accuracy. An optical clearing and staining technique for rapid three-dimensional analysis of renal biopsies was developed. Overall, this thesis aims to provide a new approach for intraoperative/intraprocedural consultation with NLM, potentially enabling more accurate, rapid, and simplified surgeries/procedures.

Thesis Supervisor: James G. Fujimoto

Title: Elihu Thomson Professor of Electrical Engineering

Acknowledgements

I would first like to thank Prof. Jim Fujimoto for his invaluable support and mentorship. He has taught me so much about research, engineering, and science and how to investigate new ideas, write proposals, and obtain funding.

I am incredibly grateful to everyone at Beth Israel Deaconess Medical Center. This thesis would not have been possible without the support of Dr. Seymour Rosen. Dr. Rosen has been a major contributor to the content of this thesis and is a strong supporter not only of my research but also my career and personal development. The commitment that he has to advancing scientific and clinical research and his unparalleled mentorship will inspire me throughout my career. I would also like to thank Dr. James Connolly. He has constantly and consistently supported me throughout the many challenges and setbacks during our technology development and clinical studies, and has enabled the success of much of the technology described in this thesis. Dr. Liza Quintana has also been critical in the development of NLM for breast pathology and has become an expert in NLM evaluation of surgical margins. Dr. Tejas Mehta has supported and advocated for the breast margin evaluation clinical studies since their initiation and has been an invaluable contributor to this work. Dr. Mary Jane Houlihan's enthusiasm for improving breast surgeries and her ability to recruit patients saved the breast clinical study in the early days, for which I am forever grateful to her. I gratefully acknowledge Dr. Yaileen Guzman Arocho and Dr. Yubo Wu who have taught me so much about pathology, always have been reliable team members, have perfected tissue preparation and NLM imaging, and have been great friends. Dr. Yue Sun, who I have only been able to work with in the later stages of my PhD, has been crucial to the success of the prostate work in this thesis. I very much appreciate Dr. Andrew Wagner and Dr. Peter Chang, who have enthusiastically supported and enabled the development of NLM technology for prostatectomies. Dr. Leo Tsai and Dr. Boris Gershman have been central to developing and advocating for techniques for rapid biopsy evaluation. I'd like to acknowledge all of the other BIDMC pathology residents and staff, who have helped me in so many different ways throughout my time at BIDMC. I would also like to extend a special thanks to all the research subjects who participated in the studies in this thesis.

I would like to extend my deepest gratitude to all of my colleagues at MIT. In particular, I am extremely grateful to Tadayuki Yoshitake, who I have worked with to develop and conduct the studies presented in this thesis throughout my entire degree. He has been an incredible colleague and friend. I would like to thank Prof. Michael Giacomelli, who, as a postdoc when I first started in the lab, taught me much about research and technology development and continues to be a constant source of insight and experience. Dr. Oscar Carrasco-Zevallos has also been a source of mentorship and experience and has helped extend the work in this thesis to new areas. A special thanks to Prof. Chi-Kuang Sun, who supported and worked with me on one of my first projects in the lab. I am also grateful to Dr. Kaicheng Liang, Dr. Hsaing-Chieh Lee, and Jason Zhang who were wonderful office mates. Dorothy Fleischer has been an incredible help in all administrative things in the lab and without her, we would not be able to conduct research.

Lastly, I would like to extend my deepest gratitude to my family. My parents, Kelly and Silva Cahill, have advised, encouraged, and inspired me throughout my graduate studies as they have my whole life. My siblings, Erica, Riley, and Dylan, have also continued to support me. And my wife, Andrea, has been extremely supportive of me throughout my graduate studies. She has directly helped me through conversations about my work and has inspired me through her success in her career, mentorships, and personal relationships. Her kindness, caring and understanding personality, and steadfast devotion has helped me through so much of the work in this thesis.

Table of contents

Chapter 1
Introduction

1.1. INTRODUCTION TO CLINICAL PROBLEM

Evaluation of paraffin-embedded histology by a pathologist is the gold standard for assessing surgical tissue and determining a definitive diagnosis for many diseases.[1] To prepare tissue for examination by a trained pathologist on a trans-illuminating histology microscope, the tissue undergoes several laborious and time-consuming steps. The tissue is first fixed in formalin, dehydrated in increasing concentrations of alcohol, and embedded in paraffin. The tissue in the paraffin block is then sectioned into 2-5 μm thin sections with a microtome, mounted on a glass slide, and stained with dyes such as hematoxylin and eosin (H&E). These time-consuming steps preclude using paraffin-embedded histology for evaluating tissue in time-sensitive scenarios such as surgery.

Frozen section analysis (FSA) is commonly used in surgeries for more rapid evaluation of tissue such as in cases of surgical margin evaluation. In FSA, the tissue is frozen rapidly rather than being formalin fixed, dehydrated, and embedded in paraffin. FSA typically requires ~20 minutes for the first specimen to be evaluated and the specimen size is limited by the equipment (cryostat) and personnel available.[2,3] In order to avoid excessively prolonging surgical time, FSA is typically restricted to a small number of specimens representing a limited fraction of the suspicious areas or surgical margins. Furthermore, in some tissues that have a high lipid content (such as breast), FSA is not regularly used since difficulty in freezing can add artifacts that affect interpretation.

Techniques that enable fresh surgical specimen evaluation without freezing or microtoming can reduce the time and labor required for intraoperative tissue analysis. Nonlinear microscopy (NLM) is a fluorescence microscopy technique that provides subcellular resolution, high contrast images of tissue using a scanned femtosecond laser by exciting fluorescence at the laser focus.[4] Tissue does not need to be microtome sectioned for imaging and therefore NLM enables rapid visualization of freshly excised surgical tissue or biopsies.[5] Exogenous fluorophores can be used to visualize structures of interest such as nuclei and cytoplasm/stroma and multiple specimens can be stained in parallel without the restrictions of tissue size or composition associated with FSA.[6–8] This could dramatically reduce the time required for NLM compared with FSA.

NLM has several advantages over other fluorescent optical techniques used to image surgical specimens, such as structured illumination microscopy[9,10], microscopy with UV surface excitation[11], light sheet microscopy[12], and confocal microscopy[13]. NLM can image below the specimen surface at adjustable depths of up to 100 μm[14], avoiding surgical and other surface debris.[15] NLM also achieves superior contrast and image quality compared with other imaging modalities, making it particularly well-suited for visualizing nuclear and cytoplasmic/stromal detail necessary for evaluating pathology.[16–18] Furthermore, recent studies in our group showed that NLM has high concordance with conventional paraffin embedded histology for evaluation of breast surgical specimens.[19]

1.2. PRELIMINARY STUDIES

1.2.1. NONLINEAR MICROSCOPY IMAGING OF BREAST CANCER

In preliminary studies, three pathologists performed a blinded reading on NLM images of breast pathologies in fresh surgical specimens and corresponding paraffin H&E images.[19] Freshly

excised breast tissue that was no longer required for diagnoses was collected from Beth Israel Deaconess Medical Center (BIDMC) Department of Pathology using protocols approved by Massachusetts Institute of Technology (MIT) and BIDMC's Institutional Review Board committees. The fresh tissue was dissected to expose areas of interest and stained with acridine orange for 30 seconds. A benchtop NLM instrument with a Ti:Sapphire laser (Mira Optima 900-F) tuned to 740 nm was used to image the tissue. The laser was scanned over the specimen with an 8 kHz resonant scanner and galvanometer. Photomultipliers (PMTs) detected the nuclear signal from the acridine orange and the second harmonic generation (SHG) /autofluorescence from the collagen. The acridine orange provided a signal analogous to hematoxylin and the SHG provided a signal analogous to eosin. The specimens were fixed in formalin and paraffin H&E sections were made of faces corresponding to the NLM imaging surface.

A total of 179 specimens from 50 patients were imaged. An example of a specimen showing ductal carcinoma in situ (DCIS) is shown in **Figure 1.1** in NLM (A) and paraffin H&E (B). Three pathologist then read the NLM and paraffin H&E images in a training and reading phase. In the training phase, pathologists reviewed 30 paired NLM and paraffin H&E data sets to gain familiarity with the technique. The pathologists then read 138 NLM data sets and assigned a diagnosis to each one. After a wash out period, the pathologists read the corresponding paraffin H&E sections and again assigned a diagnosis to each one. The results showed a 95.4% (90.3-98%; 95% confidence intervals) sensitivity and 93.3% (89.3-95.9%) specificity for differentiating benign tissue vs carcinoma (DCIS, invasive ductal carcinoma (IDC), and invasive lobular carcinoma (ILC)) (**Figure 1.2**). These promising results motivated additional investigation and translation of NLM into clinical use.

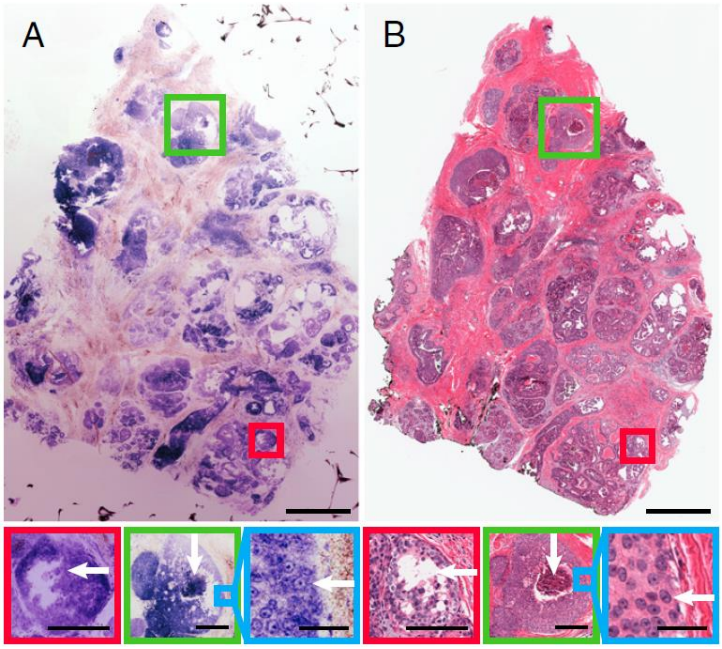

Figure 1.1. Example images of a human breast specimen with ductal carcinoma in-situ. (A) An NLM image displayed in an H&E color scale and (B) the corresponding paraffin H&E slide. (Scale bar = 1 mm.) Finger-like projections of neoplastic cells invading the duct lumen are indicative of micropapillary DCIS (red box). (Scale bar = 250 μm.) Irregular-shaped cavities with cellular debris and comedo plug are indicative of comedo DCIS (green box). Scale bar = 250 μm. Individual cell nuclei at the periphery of the comedo DCIS exhibit prominent nucleoli consistent with high-grade DCIS (blue box). Scale bar = 50 μm.[19]

		95% Confidence	
Benign vs. DCIS/IDC/ILC		Lower limit	Upper limit
Sensitivity, %	95.4	90.3	98.0
Specificity, %	93.3	89.3	95.9
Accuracy, %	94.1		
PPV, %	89.4		
NPV, %	97.1		

Figure 1.2. Average sensitivity and specificity of three pathologists for distinguishing between benign breast tissue vs DCIS and invasive carcinoma using NLM.

1.2.2. CLINICAL NONLINEAR MICROSCOPE

A standard bench-top NLM instrument was used for the breast preliminary studies described in the previous section. To translate this technology into the clinic, we designed an NLM instrument with functionality and ergonomics optimized for pathology laboratory use (Figure 3).[14,20] A Ti:Sapphire laser (Chameleon Ultra, Coherent, Inc.) was used as the light source. An automated objective changer with a 10x, 0.45 NA objective and a 5x, 0.25 NA objective was used to view tissue at variable magnification. Stained specimens were imaged in an inverted configuration with translation controlled by linear motor stages. Fluorescence from nuclear and stromal/cytoplasmic stains, and signals were detected and displayed in an H&E color scale using a graphic processor unit. A white light camera was integrated with the NLM instrument to record a gross view of the specimen.

The NLM instrument operates in two modes: *real-time NLM mode* which emulates the procedure pathologists use to evaluate paraffin slides with a standard microscope and *auto-scan NLM mode* which emulates a digital slide scanner. In *real-time mode*, the pathologist examines the specimen on a computer display showing NLM images at 16 frames/second, while translating the specimen to select the NLM field of view. The 5x objective is used for rapid inspection to identify regions of interest while the 10x objective is used to detect pathology. A fiducial marker is displayed on the white-light gross image of the specimen indicating the current position of the NLM image. The NLM images, depths, gross image, and fiducial position are saved for post-procedural analysis. In *auto-scan NLM mode*, a digital NLM image of the entire specimen is generated by automatically acquiring a series of overlapping, high magnification regions. The NLM frames are stitched together and viewed analogously to a whole slide image from a digital

slide scanner. The auto-scan NLM mode only acquires a limited number of image depths, however it enables multiple readers to evaluate NLM image data offline.

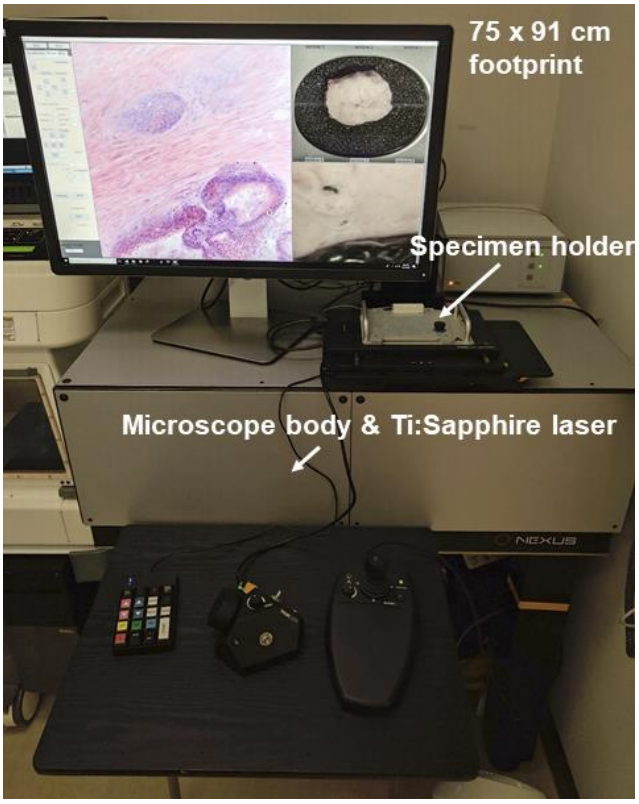

Figure 1.3. A photograph of the NLM instrument. Fluorescence signals are displayed in a color scale resembling H&E. A white light image (right) of the gross specimen and a high magnification NLM view (left) of a region of interest are displayed. After imaging, the specimen is processed for H&E histology.

1.3. SCOPE OF THESIS

In this thesis, we develop and validate NLM evaluation techniques for several clinical scenarios. The studies in this thesis are performed in close collaboration with the Departments of Pathology, Surgery, Radiology, and Urology at Beth Israel Deaconess Center (BIDMC). Overall,

this thesis aims to provide a new approach for intraoperative/intraprocedural consultation with NLM, potentially enabling more accurate, rapid, and simplified surgeries/procedures.

In **Chapter 2**, we develop a rapid, robust fluorescent staining protocol for NLM imaging with a compact, low cost ytterbium laser and validate it on fresh breast tissue.

In **Chapter 3**, we develop technology and methods for a prospective 98 patient interventional randomized controlled trial at BIDMC on patients who will receive a lumpectomy for breast cancer. A pathologist evaluates breast surgical margins with NLM intraoperatively to provide real-time surgical feedback. The hypothesis is that NLM evaluation of surgical margins will reduce the rate of indication for repeat surgeries. We are currently recruiting patients to participate in this study at BIDMC.

In **Chapter 4**, we develop and characterize NLM for evaluation of fresh prostate tissue. Three pathologists perform a blinded reading on NLM images of 122 specimens from 40 patients to assess the accuracy of detecting cancer in prostatectomy specimens. We evaluate prostate surgical margins on patients who have underwent a prostatectomy to demonstrate future potential for intraoperative interventional studies.

In **Chapter 5**, we assess the feasibility of rapid intraprocedural biopsy analysis using NLM. A total of 170 biopsies were collected from 63 patients who underwent targeted in-bore MRI or MRI-ultrasound fusion biopsy. Genitourinary pathologists evaluated the biopsies on an NLM instrument in real time then subsequently by FFPE histology and diagnoses were compared.

In **Chapter 6**, we develop staining and optical clearing techniques for rapid three-dimensional analysis of renal biopsies.

Chapter 2
Rapid virtual H&E histology of breast tissue using a compact nonlinear microscope

2.1. INTRODUCTION

Breast cancer is the second most common form of malignancy in American women, with over 300,000 cases diagnosed annually.[21] The standard of care for early-stage breast cancer is breast conserving therapy (BCT) which includes surgery to remove the tumor followed by adjuvant radiation therapy and possibly chemotherapy to eradicate residual disease.[21,22] Unfortunately, due to the difficulty assessing tumor margins during surgery and the desire to conserve breast tissue for aesthetic outcome, up to 40% of all women who receive BCT require repeat surgeries due to positive or close margins[23–28], resulting in increased morbidity, worsened cosmetic outcomes, delayed radiotherapy and greatly increased healthcare costs. Formalin fixed, paraffin embedded hematoxylin and eosin (FFPE H&E) histopathology is the gold standard for evaluating breast surgical margins, however, the multi-hour processing time of fixation, embedding, microtoming and staining, precludes rapid evaluation of histology. Frozen section analysis (FSA) enables rapid tissue processing and evaluation, but has reduced accuracy when compared to standard FFPE H&E and is particularly challenging in fatty tissue due to freezing artifacts and physical sectioning difficulties.[29,30] Furthermore, both of these techniques are labor-intensive, resulting in substantial pressure from both the Centers for Medicare and Medicaid Services and private insurers to control costs.[31]

Therefore, new technologies for rapid and cost-effective histological evaluation of surgical pathology could improve breast cancer treatment, while reducing health care costs by reducing re-

excision rates. Optical sectioning microscopy enables rapid, high resolution imaging of freshly excised tissue specimens by imaging a selected narrow depth range within tissue without requiring physical sectioning on a microtome.[32] Confocal fluorescence microscopy (CFM)[33–37], structured illumination microscopy (SIM)[38,39], stimulated Raman scattering[40], and nonlinear microscopy (NLM)[19,41,42] have all been reported to enable optical sectioning and histological evaluation of pathology in freshly excised, unfixed tissue without microtoming. Of these methods, NLM is uniquely attractive because nonlinear fluorescent excitation enables high resolution imaging through overlaying tissue, blood or cellular debris into surgical specimens at extremely high imaging rates relative to other methods. Furthermore, recent studies have demonstrated a high rate of concordance with conventional paraffin embedded histopathology for the evaluation of breast surgical specimens.[19]

Unfortunately, NLM typically requires femtosecond Titanium:Sapphire (Ti:Sapphire) lasers, which are large, fragile, expensive, and require regular maintenance. Alternatively, a few previous works have used high power amplified fiber laser systems[43,44], which are more compact, but still relatively costly. A more cost-effective alternative is to use lower power, unamplified femtosecond ytterbium fiber lasers that operate at 1 μm wavelengths. These lasers are widely used for industrial applications because of their low cost, compact size, and excellent reliability, important requirements for an intraoperative diagnostic tool. Furthermore, a 1 μm wavelength is advantageous because there is less signal attenuation than for shorter wavelengths, enabling deeper imaging into tissue[45–47] analogous to serial sectioned histology. Subsurface imaging is important in intraoperative scenarios where the specimen surfaces typically have contamination due to electrocautery, surgical ink or debris from specimen handling, making pathologies difficult to visualize.

Reproducing the established diagnostic features of H&E stained tissue using fluorescence NLM requires nuclear specific contrast with stromal counterstaining analogous to hematoxylin and eosin. These fluorescent stains must be spectrally separable from each other to discriminate between structures, rapidly penetrate live tissue, avoid interference with subsequent histological processing or assays, and be cost-effective. 4',6-diamidino-2-phenylindole (DAPI), a blue nuclear fluorophore, has been used with eosin, a strong red fluorophore, to provide H&E-like contrast in fluorescence microscopy.[48] However, DAPI does not reliably and uniformly stain viable (freshly excised) tissue and two photon excitation of DAPI requires shorter wavelengths (two photon excitation maximum at ~0.7 μm) and therefore cannot be used with inexpensive ytterbium fiber lasers. Acridine orange (AO) is a common nuclear stain that has been used in CFM[49], SIM[39], and NLM[19]. AO rapidly binds to DNA, has a broad absorption spectrum and high quantum yield. Second harmonic generation (SHG),[19] which was used in the preliminary study described in Section 1.2.1. and eosin[50] have been combined with AO to provide stromal contrast, however, the former requires high incident powers and has poor specificity for eosinophilic structures and the latter overlaps emission spectra with AO making separation of signal complicated. Sulforhodamine 101 (SR101) is a low cost, red fluorescent fluorone stain with a structure closely related to that of eosin. SR101 stains cytosol and collagen similarly to eosin[51] and rapidly penetrates through live tissue. Furthermore, the red emission makes it spectrally-separable from AO, while the large two photon absorption at 1 μm lowers laser power requirements.

In this chapter, we describe a technique for rapid histological evaluation of freshly excised, unfixed breast tissue specimens using fluorescence NLM with a compact, low cost fiber laser (**Figure 2.1**). A rapid staining procedure using AO and SR101 generates images analogous to FFPE H&E slides at video-rate (16 frames per second). We demonstrate that the fluorescent stains

are extracted to undetectable levels by standard tissue processing using a commercial histology processor (ethanol dehydration followed by xylene) and do not affect HER2 amplification status via fluorescent in situ hybridization (FISH) assay. We present a comparative study of freshly excised, unfixed breast tissue pathology using virtual H&E nonlinear microscope images and standard FFPE H&E.

The work in this chapter was first published in Laboratory Investigations.[8] This work was done in collaboration with Michael G. Giacomelli, Tadayuki Yoshitake, and James G. Fujimoto at Massachusetts Institute of Technology, Hilde Vardeh, Beverly E. Faulkner-Jones, and James L. Connolly at Beth Israel Deaconess Medical Center and Harvard Medical School, and Chi-Kuang Sun at National Taiwan University. The work was supported in part by the National Institutes of Health R01-CA178636, R01-CA075289-19, F32-CA183400-02 and Air Force Office of Scientific Research FA9550-12-1-0551 and FA9550-15-1-0473.

2.2. MATERIALS AND METHODS

Tissue preparation

To demonstrate rapid imaging for real-time histological evaluation of breast tissue, breast tissue not required for diagnostic purposes was collected from patients undergoing mastectomy or lumpectomy. All research was performed according to protocols approved by Massachusetts Institute of Technology Committee on the Use of Humans as Experimental Subjects and Beth Israel Deaconess Medical Center Committee on Clinical Investigations and Institutional Review Board. The requirement for informed consent was waived by both committees because specimens were de-identified discarded human tissue, not required for clinical diagnosis.

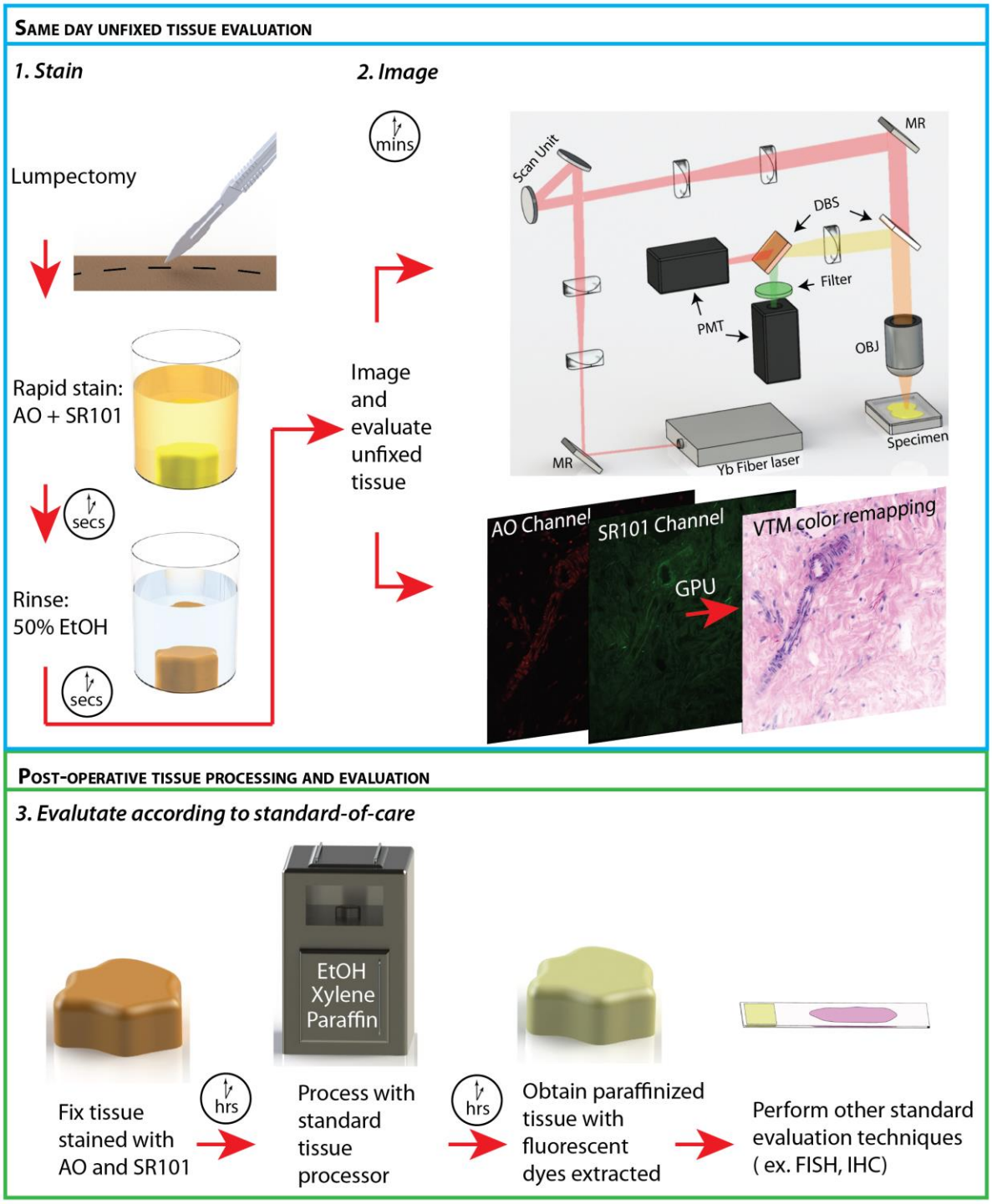

Figure 2.1 The method for processing and evaluating breast tissue using the rapid staining and imaging technology. *Stain:* Freshly excised, unfixed tissue was stained in an acridine orange (AO), sulforhodamine 101 (SR101) solution and rinsed of excess stain using a 50% ethanol/ 50% water solution. *Image:* The light source, an ytterbium fiber laser, was scanned on to the sample

through a 20X objective (OBJ) with resonant and non-resonant galvanometer actuated mirrors (scan unit). Fluorescent light from the specimen was separated from the two photon excitation light via a dichroic beam splitter (DBS) and further separated into components of fluorescent emission from AO and SR101 via a second DBS. Light was collected using a photomultiplier tube (PMT) for each channel. The PMT channels were rendered as virtual H&E images on a graphics processing unit (GPU) and displayed in real time. (MR: Mirror). *Evaluate according to standard-of-care:* Stained tissue was formalin fixed and underwent standard paraffin embedded histology processing using a commercial tissue processor (Tissue Tek VIP 5, Sakura, CA, USA), which includes ethanol dehydration, xylene rinsing, and paraffin infiltration. The standard processing extracted AO and SR101 to levels undetectable with NLM microscopy. Subsequent tissue evaluation can be performed in order to guide treatment and assess surgical outcome.

Unfixed, inked surgical specimens were procured within hours of surgery, dissected to reveal representative pathology and stained in a solution of 160 μM AO and 65 μM SR101 dissolved in 1:1 water: ethanol for 2 minutes, then rinsed in 1:1 water: ethanol for 20 seconds. The 1:1 water: ethanol solution for staining is necessary to prevent the crystallization of SR101 that occurs when AO and SR101 are mixed together in pure water. With a 2-minute staining time, AO and SR101 penetrated up to 400 μm from the surface into the tissue, although staining times as short as 30 seconds enable deep volumetric NLM imaging (**Figure 2.9**). The stained specimens were transferred to a modified histology processing cassette with a glass coverslip on the front to provide a flat imaging surface for NLM. After NLM imaging, the specimens were fixed in 10% (vol/vol) neutral buffered formalin while immobilized against the coverslip to maintain tissue orientation of the imaged surface, then processed, paraffin embedded, physically sectioned, and stained with H&E. The H&E slides were scanned and linearly scaled to match the size of the freshly excised, unfixed tissue (as recorded by optical encoders on the NLM precision microscope

stage prior to fixation) to account for minor tissue deformation (< 10%) due to paraffin embedding and microtoming.

Image acquisition

Figure 2.1 shows a schematic diagram of the NLM instrument. The light source was a 1.03 μm wavelength ytterbium fiber laser (Origami-10, OneFive, Regensdorf, Switzerland) generating 170 fs pulses at 100 MHz repetition rate with an average output power of 210 mW. The laser beam was scanned with an 8 kHz resonant scanner (16 kHz bi-directional line scan rate) and a perpendicular galvanometer scanner through a 20X, 1.0 NA water immersion objective (XLUMPFL20XW 1.0 NA, Olympus, Tokyo, Japan). The incident average power was ≤65 mW on the specimen and the fluorescent emission light from the AO and SR101 was collected with a dichroic beam splitter (DBS) (590 nm cutoff) and directed to two photomultiplier tubes (PMT; H7422-40p, Hamamatsu, Japan). An additional 540±20 nm bandpass filter was used in the AO channel to reduce autofluorescence. 1024 x 1024 pixel frames with a 490 μm x 490 μm field of view were acquired at 16 frames per second and mosaicked by a linear motor translating stage (MLS203, Thorlabs, NJ, USA). Images at planes below the specimen surface could be acquired by adjusting the objective focus.

Image processing

Fluorescent NLM images were rendered into an H&E color display using a computer algorithm called virtual trans-illumination microscopy (VTM).[6] In VTM, the concentration of dye or fluorophore is estimated based on the fluorescence intensity and converted to a transillumination absorption using the Beer-Lambert law, which relates dye concentration to absorption. This enables physically realistic rendering of epi-detected NLM images as FFPE transillumination H&E images in real time and at video rate[6], enabling the microscope to be operated like a conventional

histological microscope. However, to compare NLM images to FFPE H&E slide images, frames from each specimen location were recorded with 10-fold averaging at constant magnification and then stitched into mosaic images to create large field of view single plane images at a given depth below the specimen surface. This process takes approximately 4.75 seconds per mm^2, which is an artificially long delay and only required for comparison to FFPE H&E sections. In a clinical setting, the instrument would be operated in real-time mode analogously to a conventional histological microscope, without requiring mosaicking.

Reading and analysis

NLM and corresponding FFPE H&E images were read by experienced breast pathologists (HV, JLC) to assess if features on NLM required for diagnosing breast cancer were visible and to confirm that NLM images do not exhibit artifacts which confound diagnosis.

2.3. RESULTS

Normal human breast tissue

Figure 2.2 shows (a) an NLM image and (b) a corresponding FFPE H&E slide of normal breast tissue. Characteristic features of normal breast tissue were seen on both the NLM and FFPE H&E images. Within the tissue, terminal duct lobular units (TDLUs) in the NLM images (**Figure 2.2**, green and **Figure 2.2** brown) and the FFPE H&E images (**Figure 2.2**, blue and **Figure 2.2**, orange) show clear correspondence. Individual acini (NLM: **Figure 2.2**, yellow; FFPE H&E: **Figure 2.2** pink) and larger nonterminal ducts (NLM: **Figure 2.2**, purple; FFPE H&E: **Figure 2.2** gray) are identifiable on NLM and match the FFPE H&E image. Areas of normal adipocytes and

collagen are both clear in NLM and FFPE H&E (inset in green and blue and in **Figure 2.2**a and b, respectively).

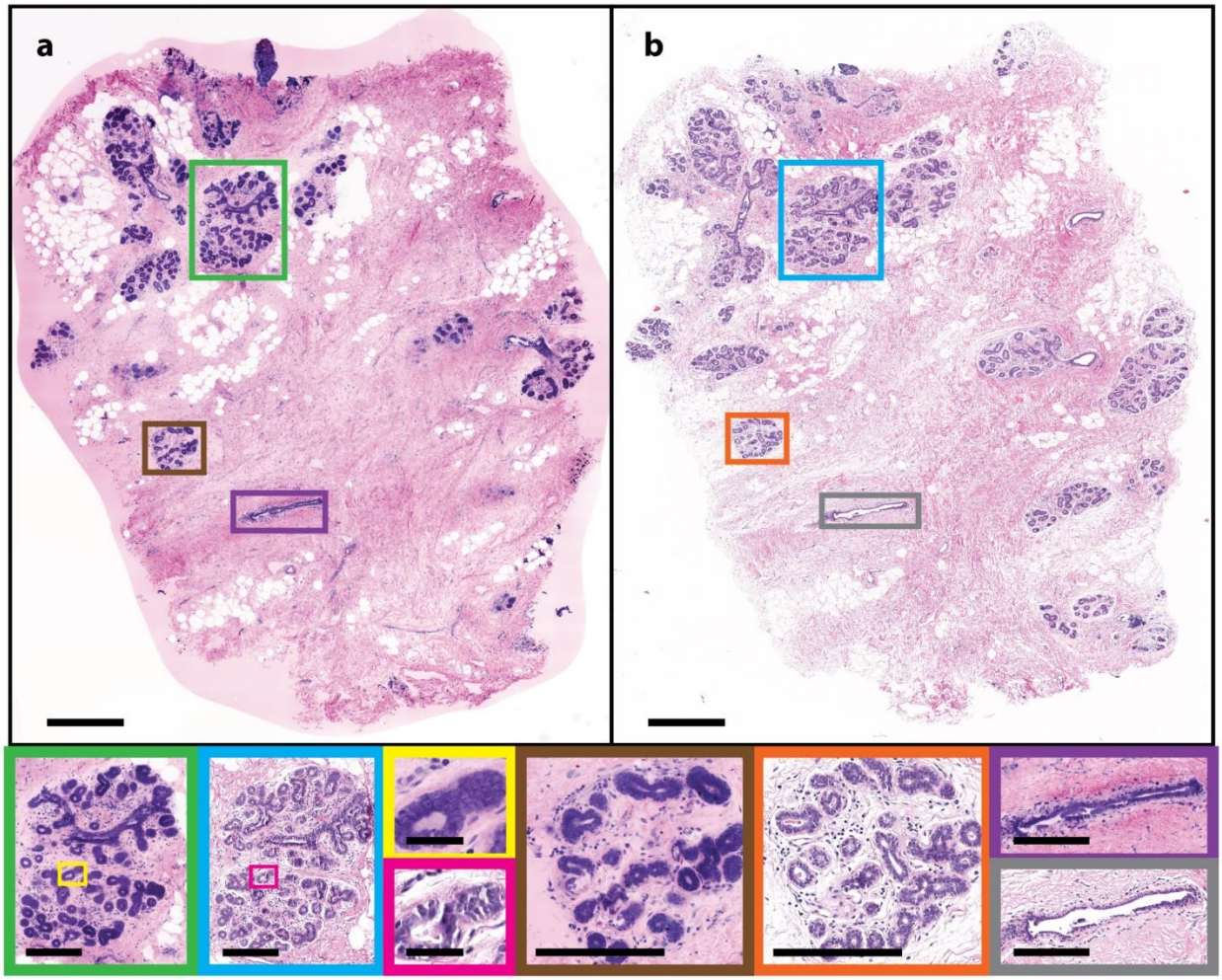

Figure 2.2. Normal human breast tissue. (a) NLM and (b) FFPE H&E histology images (500 µm scale bar). Normal TDLUs (NLM: green and brown box; FFPE H&E: blue and orange box) (250 µm scale bar), individual acini (NLM: yellow box; FFPE H&E: pink box) (50 µm scale bar) and larger ducts (NLM: brown box; FFPE H&E: gray box) (250 µm scale bar) are shown magnified. NLM: https://slide-atlas.org/link/zmhbwg. FFPE H&E: https://slide-atlas.org/link/noazj9.

Invasive ductal carcinoma

Invasive ductal carcinoma (IDC) accounts for more than three quarters of all breast cancers [52]. IDC is diagnosed when cancer cells break through the basement membrane of ducts and infiltrate the surrounding breast stroma. This pathology is characterized by malignant cells with variable prominent glandular structures infiltrating the breast parenchyma. **Figure 2.3** shows (**a**) an NLM image with (**b**) a corresponding FFPE H&E image of an IDC specimen. Areas of malignant cells can be seen in the NLM images (**Figure 2.3**, green) and FFPE H&E images (**Figure 2.3**, blue) with areas of hyalinized stroma. Both images show infiltrating nests and glands of malignant cells, characteristic of IDC (NLM: yellow; FFPE H&E: pink). There are inflamed vessels (**Figure 2.3**, NLM: brown; FFPE H&E: orange) indicated by an increase in the endothelial cell size and an exudative infiltrate of lymphocytes. In the NLM image, like the FFPE H&E image, typical malignant cell features, such as irregular shape and size of cells are evident.

Invasive lobular carcinoma

Invasive lobular carcinoma (ILC) is the second most common histological type of breast cancer.[53] ILC begins in lobules of the breast and invades the surrounding stroma. **Figure 2.4** shows an (a) NLM image and (b) a corresponding FFPE H&E image of ILC. Classic ILC patterns of invasive lobular malignant cells infiltrating the surrounding breast stroma in a single file pattern are seen in the corresponding NLM (**Figure 2.4**, purple and brown) and the FFPE H&E images (**Figure 2.4**, blue and orange). The single file strands of malignant cells are highlighted in the inset of **Figure 2.4** outlined in yellow (NLM) and pink (FFPE H&E). Additionally, inflammatory infiltrates of lymphocytes, a typical response to a disease process such as cancer, along with a cross-sectional cut through a vessel, can be seen in NLM (**Figure 2.4**, green) and FFPE H&E (**Figure 2.4**, gray).

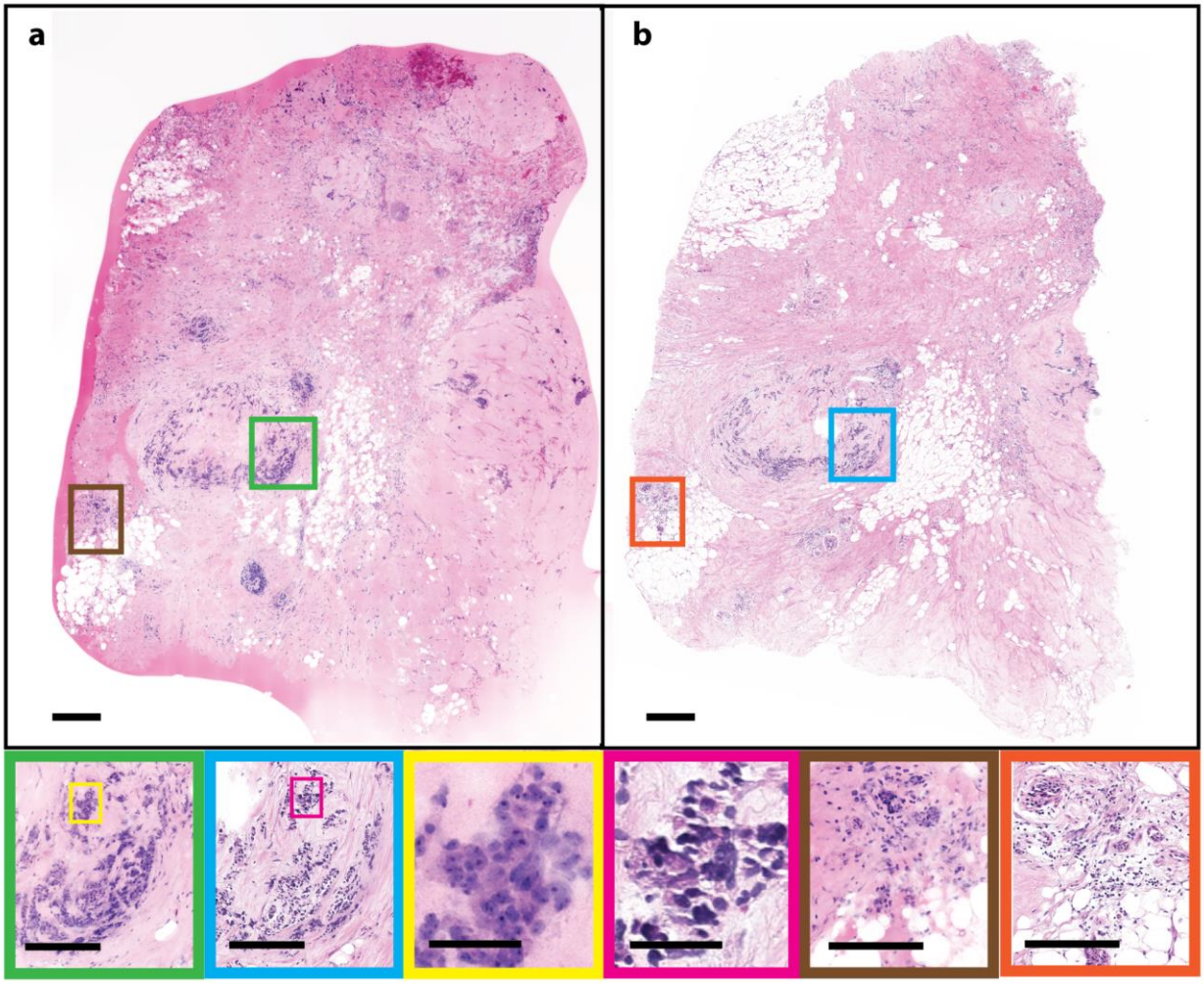

Figure 2.3. Human breast tissue showing invasive ductal carcinoma. (a) NLM and **(b)** FFPE H&E images (500 µm scale bar). Malignant cells are shown in the NLM (green) and FFPE H&E images (blue) (250 µm scale bar) infiltrating the breast stroma, with a high power view shown in yellow (NLM) and pink (FFPE H&E) (50 µm scale bar); inflamed vessels with a lymphocytic infiltrate are shown in brown (NLM) and orange (FFPE H&E) (250 µm scale bar). NLM: https://slide-atlas.org/link/tfdr77. FFPE H&E: https://slide-atlas.org/link/zatgkv.

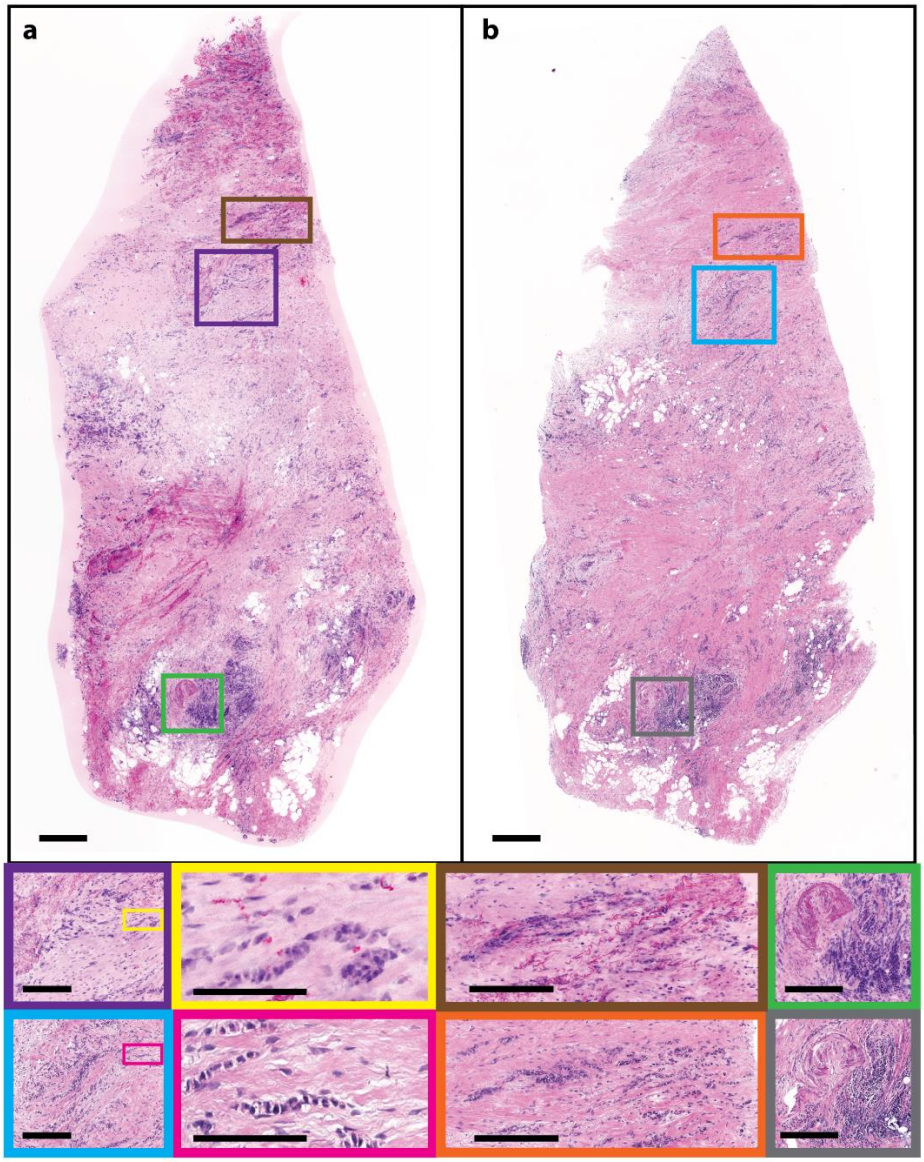

Figure 2.4. Human breast tissue showing invasive lobular carcinoma. (**a**) NLM image of freshly excised, unfixed human breast tissue with evident ILC and (**b**) corresponding FFPE H&E histology (500 µm scale bar). Many individual rows of malignant cells are in the NLM (purple and brown) and FFPE H&E images (blue and orange) (250 µm scale bar). A high power view of the ILC single file pattern is shown in yellow (NLM) and pink (FFPE H&E) (100 µm scale bar). A corresponding lymphocytic infiltration in the NLM and FFPE H&E images is shown in green and gray, respectively (250 µm scale bar). NLM: https://slide-atlas.org/link/ghg3vq. FFPE H&E: https://slide-atlas.org/link/h7vtjp.

NLM at multiple depths for serial optical sectioning

NLM can generate images at different depths in tissue which are analogous to serial sectioned histology, decreasing the requirements on specimen flatness during imaging and enabling imaging through tissue surface artifacts due to electrocautery or debris from specimen handling. **Figure 2.5** shows images acquired at multiple depths to 100 μm below the tissue surface acquired with a constant laser power and detector gain. The detector gain was optimized for surface imaging. Digital gain in post processing was applied to the frames to match the average frame intensity throughout the stack of frames. This data shows that even with constant laser power and gain, it is possible to visualize tissue features 100 μm below the tissue surface.

Extraction of AO and SR101 during histological processing

Both SR101 and AO have high solubility in typical histology solvents such as ethanol and xylene and are expected to be extracted during processing. To assess the extraction of SR101 and AO as the result of routine histological processing, representative specimens of freshly excised, unfixed breast tissue were divided in half. The transected face of one half was stained with AO and SR101, while the matching face was unstained. The tissue was then fixed in formalin and processed using standard tissue processing on a vacuum infiltrating processor (VIP) (Tissue Tek VIP 5, Sakura, CA, USA). The last tissue processing step is paraffin infiltration, however, paraffin is highly optically scattering, while infiltration produces geometric distortion of tissue. For purposes of comparison, the VIP was programmed to terminate prior to the paraffinization step (**Table 2.1**). To provide images of unstained control tissue for comparison, second harmonic generation (SHG) contrast generated with an 800 nm Ti:Sapphire laser was used to image tissue without staining.

Solution	70% EtOH	85% EtOH	95% EtOH	95% EtOH	95% EtOH	100% EtOH	xylene	xylene	xylene
Time (mins)	45	45	45	45	45	45	45	40	40

Table 2.1 The tissue processing program for the vacuum infiltrating processor used to extract exogenous stains from the tissue.

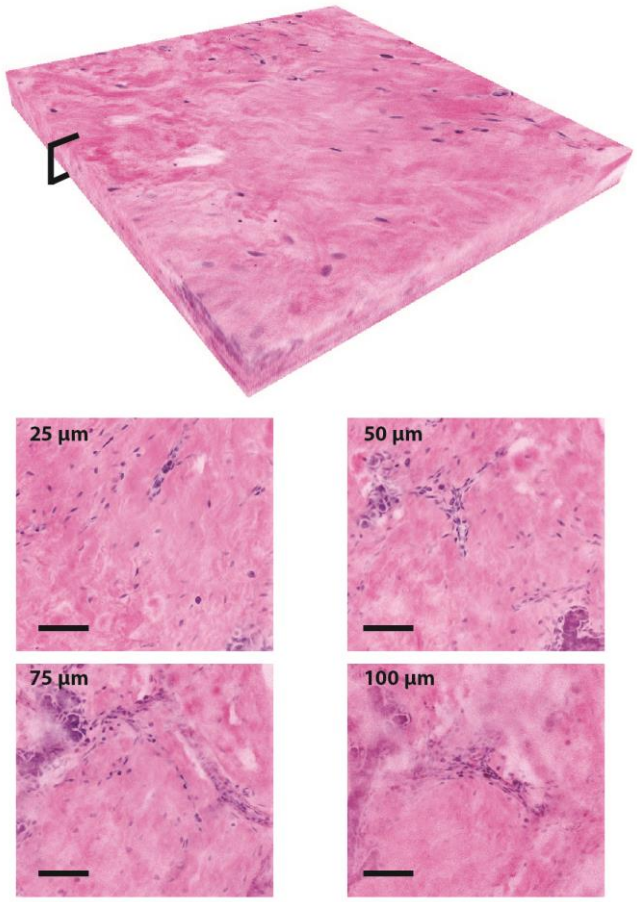

Figure 2.5. A 500x500x100 µm three-dimensional stack of NLM images demonstrating imaging at different depths in normal breast tissue. The volumetric reconstruction shows image data from the surface to 100 µm deep with digital gain applied to the images in post processing to match the average frame intensity without changing incident laser power or detector gain (scalebars: 100 µm). Selected NLM images from 25 µm, 50 µm, 75 µm, and 100 µm depths are shown.

NLM images acquired with the same laser power and detector gain of the stained and unstained halves of the tissue are shown in **Figure 2.6**a prior to tissue processing (fluorescence: column 1, SHG: column 2) and after tissue processing (fluorescence: column 3, SHG: column 4). No fluorescence signal is detectable after tissue processing. The SHG images before and after tissue processing confirm that the images were acquired at roughly the same depth plane. Higher magnification regions of **Figure 2.6**a are shown in **Figure 2.6**b. Additionally, **Figure 2.6**b shows images acquired with 20x higher detector gain. These images show a small amount of background autofluorescence, primarily from weak green fluorescent emission of collagen fibers. Within the background fluorescence, no nuclei are discernable. Enlarging a region with nuclei prior to processing shows a weak uniform signal due to autofluorescence leakage into the AO channel rather than the intensity spikes due to bound AO seen in the images acquired before processing (**Figure 2.6**c). **Figure 2.7** shows the fluorescence spectrum of xylene used to process AO-stained tissue compared to a reference spectrum of AO taken before processing, indicating that xylene extracts AO from tissue without quenching AO fluorescence.

The reduction in fluorescent signal can be quantified by taking the ratio of the median normalized pixel intensities of the tissue before and after tissue processing for each dataset and each channel (**Table 2.2**). We found that the autofluorescence from the tissue is ~1,300 times lower than the AO-stained nuclei in the AO channel and ~12,800 times lower than the SR101 stained tissue in the SR101 channel. Because AO-stained nuclei are not present in the tissue after processing, we conclude that the intensity of AO staining is at least 1,300 times less than before tissue processing and the intensity of SR101 staining is at least 12,800 times less than before tissue processing. This reduction represents an upper bound on the maximum possible residual fluorescent signal that can be quantified given the autofluorescent background, however, since no

residual nuclei can be observed even in regions with no apparent collagen, it is likely that the actual reduction is substantially higher.

	Before Tissue Processing	After Tissue Processing	Ratio (Before: After)
Median Intensity of AO channel	1	7.6×10^{-4}	1,316
Median Intensity of SR101 channel	0.128	1.0×10^{-5}	12,800

Table 2.2. The ratio of fluorescent signal before and after tissue processing using a vacuum infiltrating processor suggests that the AO signal is reduced by at least 1,326 times and the SR101 signal is reduced by at least 12,800 times.

Verification of noninterference with fluorescence in situ hybridization

To verify that extraction of AO and SR101 would enable HER2/neu FISH assays of fluorescently stained tissue, representative specimens of freshly excised, unfixed breast tissue were divided in half. One half was stained with the AO and SR101 protocol described earlier while the other was left unstained as a control. The tissue was then processed for standard FISH and examined by a trained pathologist (**Figure 2.8**). FISH processing was done using PATHVysion HER2 probes (Abbott) and DAPI as a counterstain. The ratio of HER2:CEP 17 signals was calculated to be approximately 1 for both the treated and control tissue, which is negative for HER2 amplification. AO and SR101 fluorescence was not detectable in the FISH and there were no observable differences between the control and AO/SR101 stained tissue specimens. An analysis of the integrity of RNA and DNA after NLM preparation is discussed in Section 4.3.5.

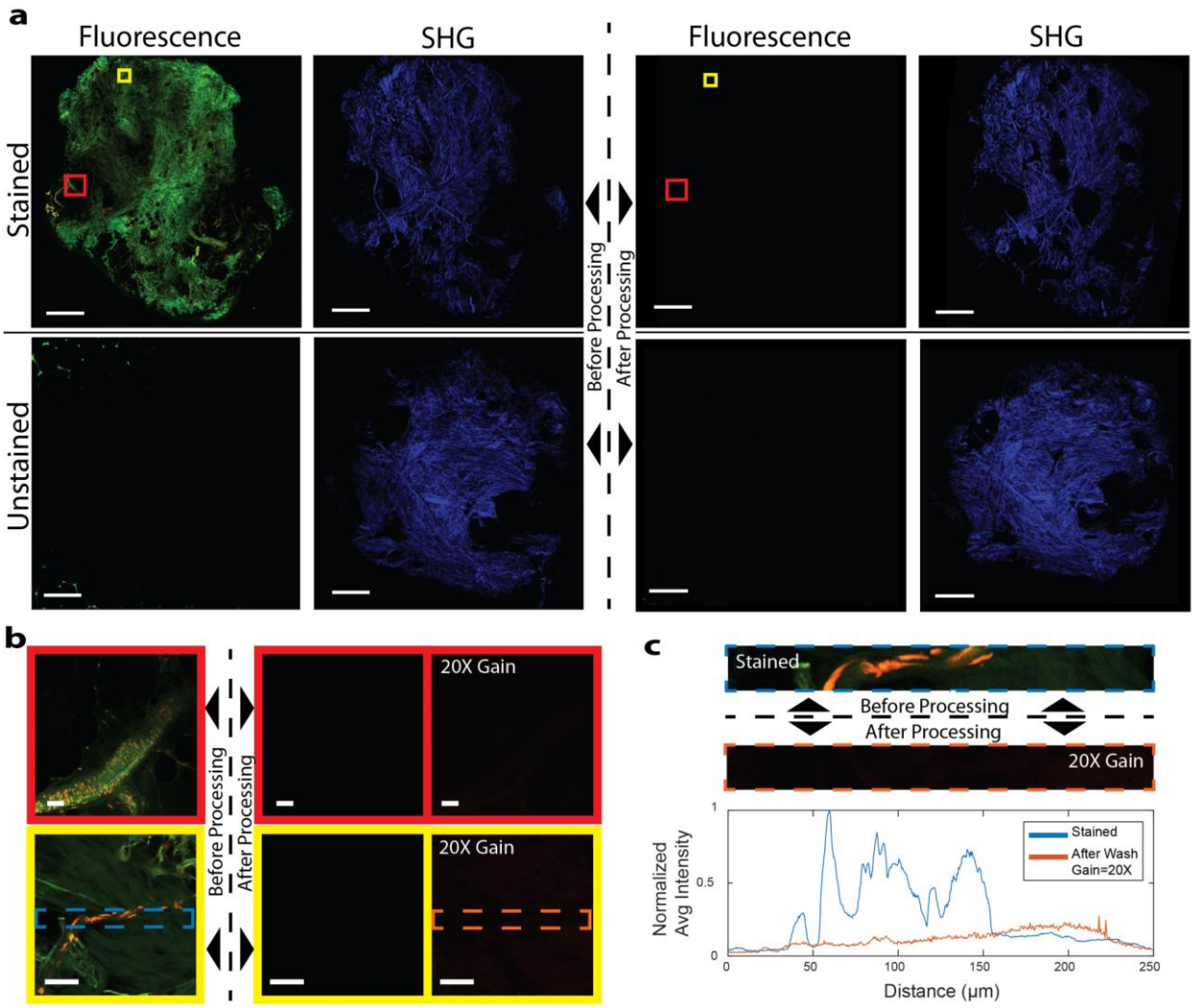

Figure 2.6. AO and SR101 are washed out to undetectable levels after standard tissue processing. (a) NLM fluorescent and SHG images before (first and second column) and after (third and fourth column) fixation and standard tissue processing of stained and unstained tissue. (Scale bars: 0.5 mm). **(b)** High magnification fluorescent images of select areas of (a) before processing (left), after processing (center), and after processing with 20 times the detector gain (right) (scalebars: 50 μm) **(c)** A representative plot of the normalized average intensity of the AO channel from a frame in (b) before processing and after processing at 20X detector gain. The spikes in the 'stained' tissue correspond to fluorescence emitted from AO in nuclei. There are no corresponding spikes in the 'after wash' graph and instead, there is a uniform background fluorescent signal present.

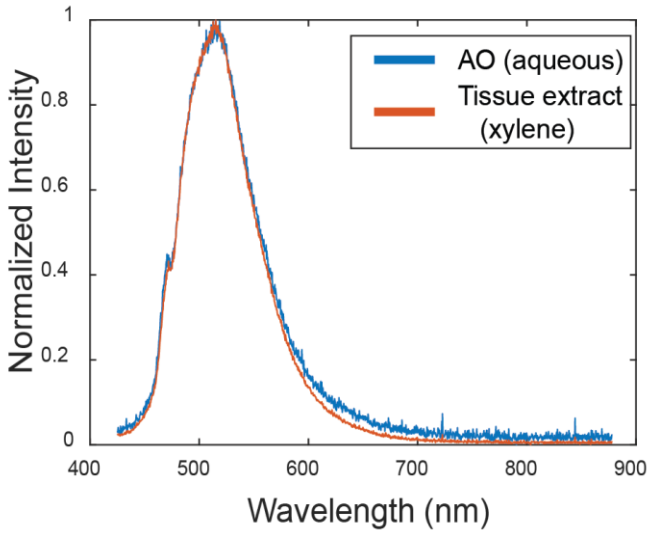

Figure 2.7. The fluorescence spectrum of xylene solvent used to extract the AO from tissue. Comparing the xylene spectrum to a control AO spectrum demonstrates that xylene extracts AO from the tissue without quenching fluorescence.

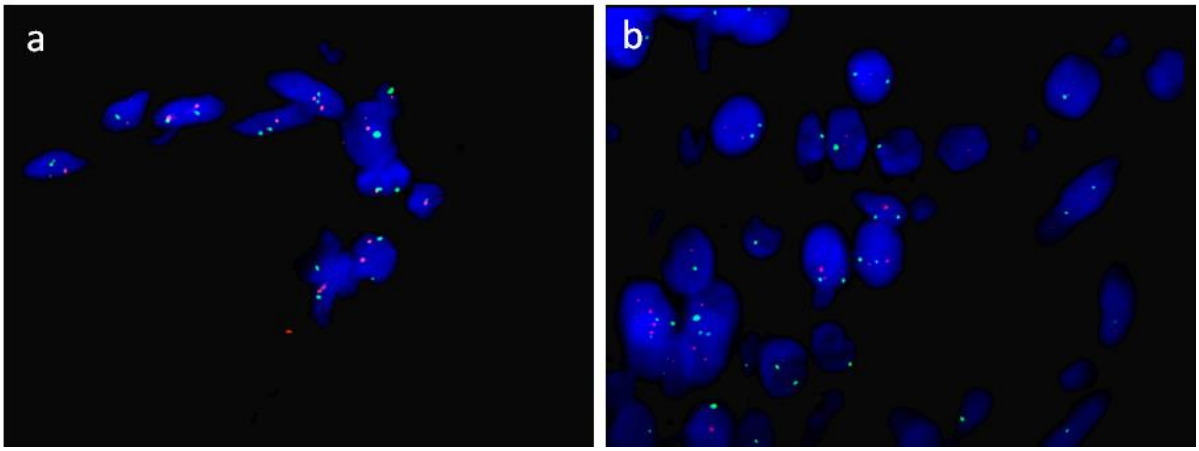

Figure 2.8. HER2/neu FISH scoring is not affected by the AO/SR101 staining procedure. Representative 100X fluorescent microscope images of a breast specimen divided in half and prepared for HER2/neu FISH analysis. FISH processing was done using PATHVysion HER2 probes and DAPI as a counterstain. (a) Tissue that was not stained with fluorescent stains prior to FISH processing, and (b) tissue that was stained with AO/SR101 prior to FISH processing. DAPI fluorescence is shown in blue, the CEP 17 DNA probe is green, and the HER2/neu probe is orange. AO and SR101 were not present in the tissue and there were no observable differences between the control and AO/SR101 stained tissue during tissue scoring and evaluation. These specimens were both scored as negative for HER2 amplification.

2.4. DISCUSSION

NLM is attractive for intraoperative evaluation of pathology because it can optically section thick tissue, eliminating the labor-intensive and time-consuming embedding and physical sectioning step required for both paraffin sections and FSA, enabling real-time histological evaluation of excised tissue to guide surgery. NLM has been demonstrated to achieve high sensitivity and specificity for discrimination of normal and malignant breast tissue.[19] Furthermore, the use of fluorescent contrast agents has several advantages, including rapid staining of live tissue, high NLM imaging speeds, high contrast, and, using the protocol described here, low fluorophore cost and compatibility with subsequent histological processing. However, the widespread use of fluorescence imaging and optical sectioning for histological evaluation of breast surgical pathology has been limited by substantial differences in the appearance of fluorescence images from standard FFPE H&E images, lack of suitable fluorescent contrast agents, high cost and complexity of lasers, and concerns about interference with subsequent diagnostics following fluorescent stained. In this report, we have overcome these limitations and developed a protocol for NLM fluorescent nuclear staining with stromal counterstaining, combined with a VTM rendering algorithm[6] to generate video rate virtual H&E images of freshly excised, unfixed tissue.

The study of representative breast surgical specimens presented here demonstrates a high degree of correspondence between FFPE H&E and real-time NLM for normal breast tissue and common types of breast carcinoma. Review by pathologists with expertise in breast cancer pathologies confirmed that diagnostically important features such as normal TDLUs (including benign individual acini and ducts) and normal fibrous and adipose stromal parenchyma, inflammation and biopsy site changes, invasive carcinoma with infiltrating nests, glands and singly or single filing of malignant cells as well as in-situ lobular and ductal carcinoma are present in

NLM images associated with pathologies identified on standard FFPE H&E histology. Despite minor differences between NLM and FFPE images such as geometric distortion and tissue shrinkage during to fixation and physical sectioning, previous work has shown that NLM has near-equivalent sensitivity to conventional histology, indicating that minor differences in artifacts do not significantly impact interpretation of breast pathology.[19] Further, quantitative image analysis of paraffin tissue sections indicates that both AO and SR101 have an extremely high degree of colocalization with hematoxylin and eosin, respectively (**Figure 2.11**, **Table 2.3**), indicating that our stains are a good approximation of conventional H&E stains. Future clinical studies will be required to demonstrate improvements in surgical outcomes, however, the results presented here strongly suggest that NLM can provide diagnostic information equivalent to FFPE H&E histology.

This chapter demonstrates that stains enabling near-equivalent images to standard paraffin embedded histology can be rapidly applied to tissue and then extracted to undetectable levels by standard histological processing. Intraoperative assessment of breast tissue margins using the proposed protocol requires treating diagnostically relevant tissue with fluorescent stains. It is therefore important to minimize any impact on the tissue characteristics to prevent interference or reduced testing accuracy in subsequent immunohistochemical, fluorescent in situ hybridization or other genetic tests that are necessary to maintain standards of patient care. A key advantage of the proposed protocol is that the fluorescent agents are selected to be highly soluble in conventional histology solvents. SR101, like eosin, is weakly bound to the tissue and highly soluble in methanol and is therefore extracted during formalin fixation. The less alcohol soluble AO is retained during fixation and dehydration, but extracted during xylene rinsing. The ability to apply stains and then extract them to undetectable levels using standard processing methods that are already validated

for IHC and genetic assays is essential to incorporating advanced nonlinear imaging techniques into existing clinical workflows.

An advance towards clinical translation of fluorescence NLM presented in this chapter is the replacement of complex, tunable Ti:Sapphire lasers with unamplified fixed-wavelength fiber lasers by selecting contrast agents compatible with low power, 1 μm excitation. While heroic efforts have been made to operate Ti:Sapphire lasers in the clinic[54], these systems are large and fragile, require regular maintenance, active cooling, vibration isolation, substantial warm-up time which precludes their use in routine clinical practice. In contrast, fiber lasers are compact and robust, do not require regular maintenance, cooling, vibration isolation and power on rapidly. Consequently, system complexity, size, weight and cost are all greatly reduced. For example, the femtosecond fiber laser used here only occupies 12" x 4" x 4" space and although the benchtop microscope used for this study occupies an additional 24" x 30" x 20", the fiber laser technology is small enough to enable NLM microscopes of comparable size to conventional light microscopes.

Another major advantage of NLM imaging at 1 μm wavelength is the increased light penetration and imaging depth in tissue compared with NLM at shorter wavelengths or confocal microscopy (**Figure 2.9**). Combined with rapid fluorescent stains with good tissue permeation, operation at 1 μm enables visualization of tissue up to 100 μm from the surface without adjusting incident power or detector gain, equivalent to 25 serial paraffin sections (**Figure 2.5**) without the processing delay and expense associated with taking sequential paraffin sections. The operator is able to view subsurface features in different regions of interest by panning and adjusting focal depth to evaluate the three dimensional structure of tissue in real time. In conventional breast histology, sequential serial paraffin sections are rarely taken due to the cost and time required to

prepare and evaluate sequential slides. The ability to easily evaluate pathology in 3D is therefore unique to optical sectioning and may enable improved diagnostic sensitivity.

The ability to image below the surface of specimens may also be an important for intraoperative breast surgery applications because tissue surfaces often have contamination artifacts. Surgical tissue specimens typically have electrocautery, loose or displaced cells from excision or grossing, strongly fluorescent fibers from gauze, paper tissue or cutting boards, and other foreign material on the tissue surfaces. This are not be present on FFPE H&E slides due to the tissue processing and microtoming which removes surface contaminants. Imaging modalities such as confocal microscopy have limited imaging range below tissue surfaces which may limit their diagnostic effectiveness in the presence of surface contamination. NLM can perform subsurface imaging to avoid surface contamination artifacts which can be especially important for evaluating areas of dense, highly scattering cells such as in IDC.

In addition to the morbidity and the patient distress associated with incomplete resection and repeat surgeries, the cost of breast cancer treatment increases with each additional surgery, resulting in a substantial economic burden[55–57]. Consequently, there is currently a shift towards a value-based insurance payment method to incentivize increased quality of care, for example, reducing hospital readmissions, in order to control costs.[58] The adoption of methods to assess margins intraoperatively promises to enable a reduction in the treatment cost while improving patient outcomes.

2.5. SUPPLEMENTARY INFORMATION

Penetration depth of AO and SR101

Rapid penetration of AO and SR101 is important for time sensitive clinical procedures such as intraoperative tumor margin assessment. To investigate penetration times, freshly excised, unfixed breast tissue was stained with AO and SR101, rinsed with 50% ethanol (EtOH), rapidly frozen to prevent further diffusion and to make the tissue rigid, and transected to expose the staining depth into the tissue. Mosaiced fluorescence NLM images of the transected tissue stained for varying times are shown in **Figure 2.9**. Even with a short 30 second staining time, AO and SR101 penetrated up to 400 μm, which is greater than the typical maximum imaging depth using 1 μm wavelength NLM.

Subsurface imaging depth using NLM at 1 μm wavelength

Figure 2.10 shows a plot comparing the natural log of the normalized average intensity of the SR101 channel versus depth in images acquired using a Ti:Sapphire laser (Mira, Coherent, USA) operating at 780 nm wavelength versus a femtosecond fiber laser (Origami-10, OneFive, Switzerland) at 1 μm for a breast tissue specimen with IDC. The 1/e decay constant of intensity vs depth in the images acquired at 1 μm wavelength was 52% greater than the decay constant of the frames acquired at 780 nm wavelength.

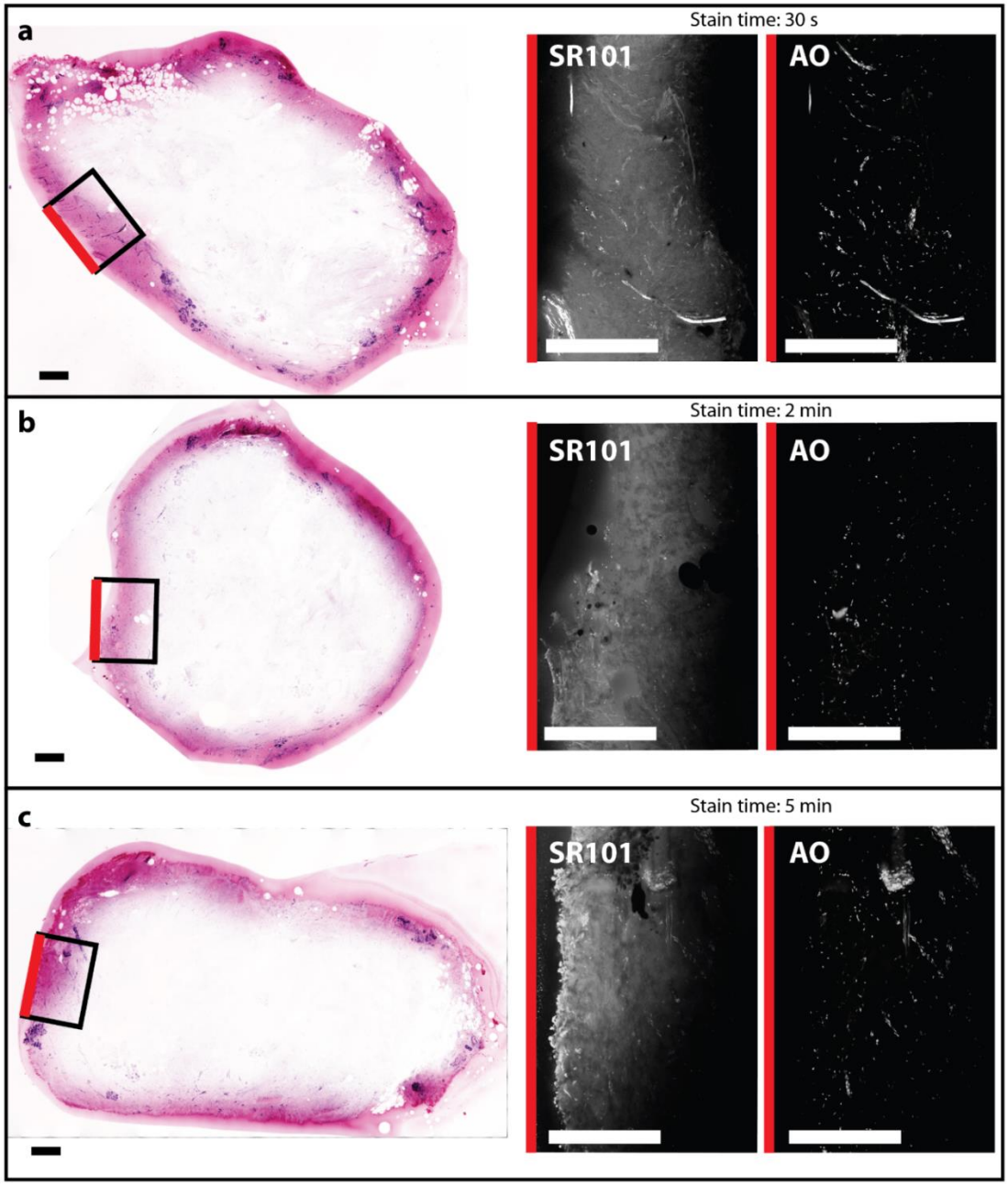

Figure 2.9. The penetration depths of AO and SR101 in freshly excised, unfixed tissue with different staining times. NLM images of freshly excised, unfixed breast tissue that was immersed in AO and SR101 for **(a)** 30 seconds, **(b)** 2 minutes, and **(c)** 5 minutes, rapidly frozen and cut in cross-section to expose the unstained center tissue (0.5 mm scale bar in all images). The SR101 channel (inset, left) and the AO channel (inset, right) are shown separately in grey-scale to highlight the penetration depths into the tissue of each stain. The penetration of both AO and SR101 is greater than 400 µm around the tissue circumference for all immersion times.

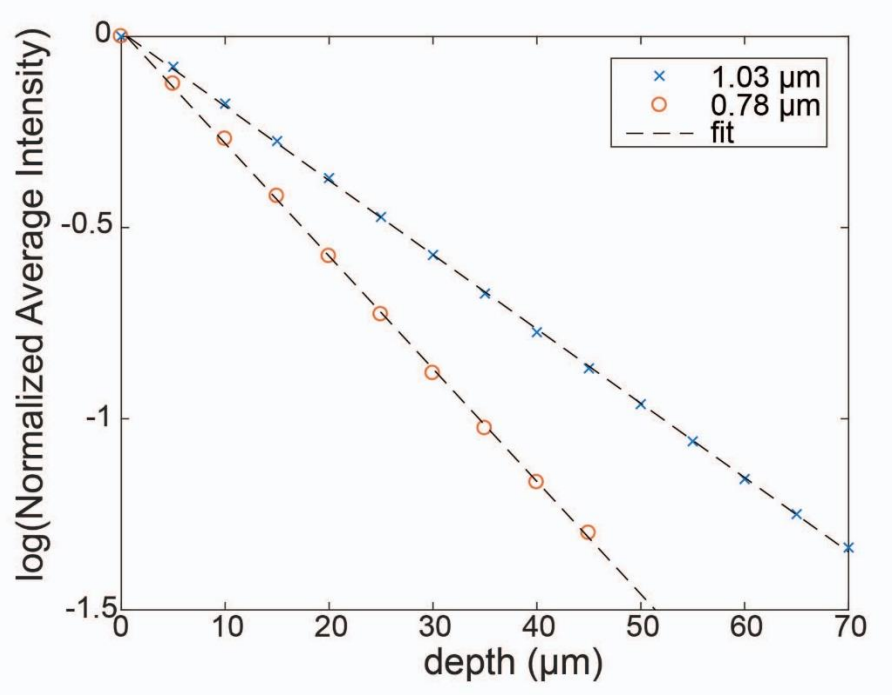

Figure 2.10. The natural log of normalized average intensity plotted vs depth below the surface of a breast tissue specimen with IDC acquired using a 780 nm wavelength Ti:Sapphire and a 1 μm fiber laser. The 1/e attenuation constants of the 780 nm and 1 μm intensities are 33.9 μm and 51.5 μm, respectively, indicating a 52% reduction in image signal attenuation when using 1 μm over 780 nm wavelength for NLM.

Colocalization of AO/SR101 staining protocol and FFPE H&E

Quantitative comparisons of staining characteristics between AO/SR101 stained freshly excised, unfixed tissue and FFPE H&E stained tissue are difficult because NLM imaging and FFPE cutting planes are typically tens of microns apart due to the tissue loss when facing paraffin blocks and the combination of fixation and microtoming which geometrically distorts the tissue. To quantitatively assess the colocalization of AO/SR101 with H&E, we cut additional ~4 μm paraffin sections from tissue specimens used in this study. Paraffin sections were mounted on glass slides, deparaffinized and then stained with either AO or SR101. The deparaffinized sections were imaged

with NLM and then stained to produce hematoxylin or eosin stained slides for comparison to the NLM images as shown in **Figure 2.11**.

The NLM images were rendered as virtual H&E images for comparison. After staining, the FFPE H&E slides were scanned using a slide scanner. The images were down sampled by a factor of 4 to a 2 μm square pixel size to facilitate image registration, minimize the effects of misregistration, reduce the effects from differences in resolution between the slide scanner and NLM objectives, and to more closely approximate the resolution typically used to evaluate breast pathology (a 5-10X light microscope air objective). The NLM images and slide scanned images were then registered using rigid registration. In the hematoxylin stained slide, the unstained portion of the tissue which is visible in the slide scanner images, was removed by subtracting the red channel from the blue channel. This was not required for the eosin stained slide because almost the entire tissue was stained with eosin, making optical diffraction artifacts insignificant. Because there is an unknown gamma correction and tone mapping applied to the images from the commercial slide scanner software, a gamma correction was applied to the hematoxylin and eosin images to maximize correlation coefficients. The degree of correlation between the images was assessed using Pearson correlation coefficient on a per pixel basis on 3 deparaffinized sections stained with AO/hematoxylin (from 2 different samples) and 3 deparaffinized sections stained with SR101/eosin (from 2 different samples). The average Pearson correlation coefficient between AO and hematoxylin stained slides was 0.85 with 0.04 standard deviation computed over 150 million pixels, and the SR101 and eosin stained slide's average correlation coefficient was 0.82 with a standard deviation of 0.03 computed over 195 million pixels (**Table 2.3**).

	AO and Hematoxylin	SR101 and Eosin
Pearson Correlation Coefficient ± standard deviation (entire deparaffinized sections)	0.85 ± 0.04	0.82 ± 0.03
Number of Pixels (millions)	150	195

Table 2.3. Pearson correlation coefficient between tissue stained with AO and hematoxylin and tissue stained with SR101 and eosin.

Since diagnosis and classification of breast cancer is sensitive to local nuclear features such as size, shape, and number of cells, we assessed local variations in correlations by subdividing the AO/hematoxylin stained slides into 4.2 megapixel frames (2048 x 2048) and computing colocalization statistics for these smaller regions. Over these subdivided regions totaling 150 megapixels, the mean Pearson correlation coefficient was 0.84 with standard deviation 0.04. This is nearly identical to the correlation coefficient computed over entire deparaffinized sections suggesting that there is high correlation between AO and hematoxylin both over entire deparaffinized sections as well as locally within deparaffinized sections.

Crystallization of acridine orange and sulforhodamine 101

Crystal formation was observed in solutions of acridine orange and sulforhodamine 101. Crystal formation prevents uniform mixing of the staining solution, introduces unknown solution concentration variations, reduces staining consistency, and appears as aggregated fluorescent dye on stained tissue (**Figure 2.12**).

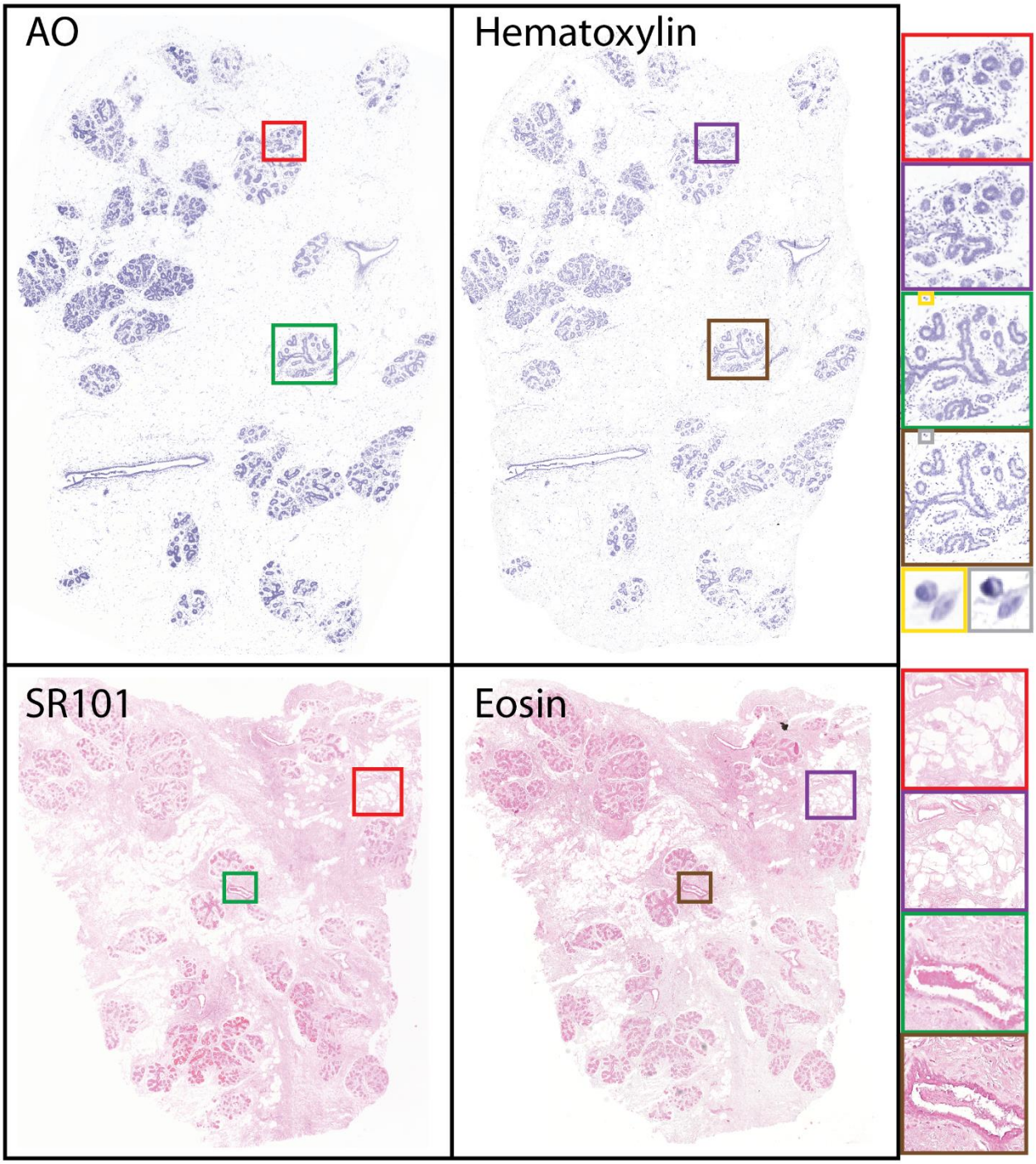

Figure 2.11. Comparison between AO/SR101 and H&E staining on a FFPE section. *Top row:* FFPE deparaffinized section with AO staining imaged with NLM (left) and the same deparaffinized section with hematoxylin staining imaged with a standard microscope (right). *Bottom row:* A second FFPE deparaffinized section with SR101 staining imaged with NLM (left) and the same deparaffinized section with eosin staining imaged with a standard microscope (right).

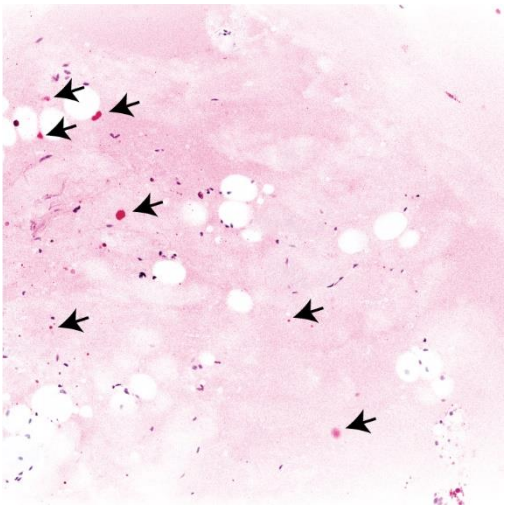

Figure 2.12. Example NLM image of breast tissue that was stained with a solution of acridine orange and sulforhodamine 101 that had crystal formation. The black arrows indicate aggregates of fluorescent dye, which should not be present in the tissue.

In order to measure the stability of acridine orange and sulforhodamine 101 in solution, various solvents were investigated. Acridine orange (40 µg/ml) and sulforhodamine 101 (40 µg/ml) were combined in separate solutions with the following solvents: tap water, phosphate-buffered saline (PBS), distilled water with 10% dimethyl sulfoxide (DMSO), 5% acetic acid (vinegar), formalin, and 50% ethanol (EtOH). The solutions were mixed with a vortex mixer for 10 seconds then left for 12 hours.

Images of the solutions are shown in **Figure 2.13**. Crystal formation is seen macroscopically in all solutions except in the solution that uses 50% ethanol as the solvent. The 50% ethanol solution was also analyzed with NLM and no crystal formation was seen microscopically.

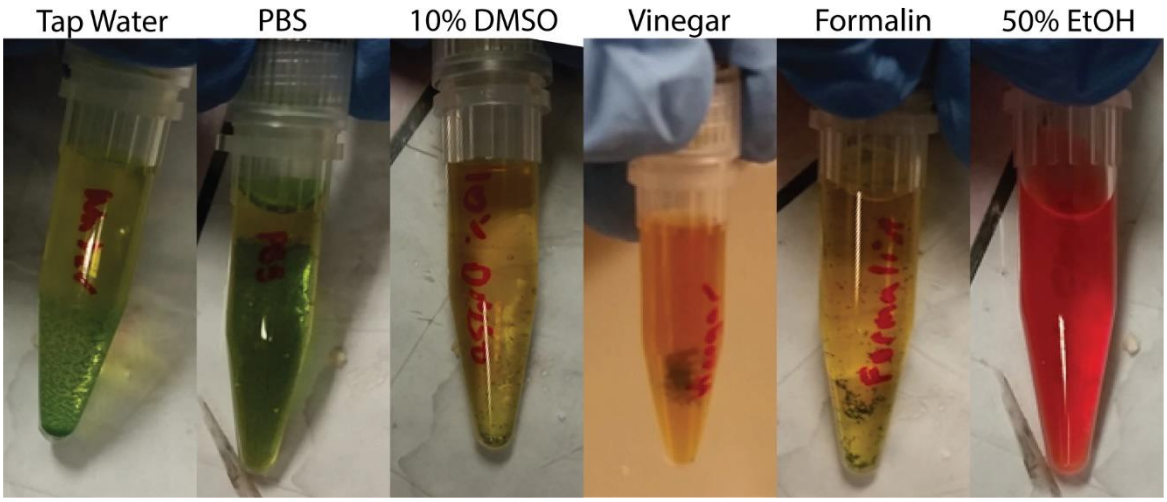

Figure 2.13. Solutions of acridine orange and sulforhodamine 101 in various solvents. Crystal formation can be seen macroscopically when the solvent is tap water, phosphate-buffered saline, water with 10% DMSO (by volume), vinegar, and formalin. No crystal formation is seen macroscopically or microscopically when using 50% ethanol (EtOH) in water.

To investigate if the concentration of ethanol affects the formation of crystals, acridine orange (40 µg/ml) and sulforhodamine 101 (40 µg/ml) were combined in separate solutions with 25% ethanol, 37% ethanol, and 50% ethanol as the solvent. Macroscopic crystals were not seen in any of the solutions. However, many crystals were seen microscopically (on NLM imaging) in the 25% ethanol solution. Very few crystals were seen in the 37% or 50% ethanol solutions. Out of caution, and in order to ensure longer term stability of the staining solution, we used 50% ethanol as the solvent in our staining solutions for evaluating freshly excised specimens.

Chapter 3
Intraoperative NLM evaluation of surgical margins on lumpectomy patients

3.1. INTRODUCTION

Up to 40% of all women who receive breast conserving therapy (BCT) require repeat surgeries from positive or close margins[23–28] resulting in increased morbidity, worsened cosmetic outcomes, delayed radiotherapy and increased healthcare costs. Formalin-fixed paraffin embedded (FFPE) H&E is the gold standard for evaluating breast surgical margins, however, it is too slow for intraoperative evaluation. Frozen section analysis (FSA) enables rapid tissue processing and evaluation, but has reduced accuracy when compared to standard FFPE H&E and is particularly challenging in fatty tissue due to freezing artifacts and physical sectioning difficulties.[29,30] This, along with the high sensitivity and specificity (95.4% and 93.3%, respectively) of nonlinear microscopy (NLM)[19] for differentiating benign breast tissue vs carcinoma and the rapidity at which NLM enables tissue evaluation, suggests that BCT may benefit from intraoperative evaluation of surgical margins using NLM.

In this chapter, we describe an ongoing study (ClinicalTrials.gov: NCT02926729) investigating NLM for intraoperative assessment of breast cancer surgical margins. This collaborative study between BIDMC Pathology, Surgery, Radiology, and MIT will develop and validate NLM for intraoperative assessment of breast surgical margins with the goal of reducing repeat surgeries. A 98-patient randomized controlled trial design, with two evenly distributed control and study arms, will be described. The primary endpoint of this study is the rate of repeat surgeries in the study group of patients receiving intraoperative NLM evaluation followed by

postoperative paraffin H&E histology vs the control group of patients receiving only postoperative paraffin H&E evaluation. Preliminary results will be discussed but since this study is still ongoing, endpoints will not be analyzed.

This study uses the clinical NLM instrument described in Section 1.2.2. The NLM instrument uses a Ti:Sapphire laser (Chameleon Ultra, Coherent, Inc.) at 1030 nm wavelength and not the ytterbium fiber laser described in Chapter 2. The NLM instrument developed in Section 1.2.2. was developed with a tunable Ti:Sapphire laser to enable flexibility in excitation wavelength and power for investigation of different imaging protocols. The increased flexibility of this NLM instrument was important for protocol development. Since robust imaging protocols were developed to be compatible with the fixed 1030 nm wavelength of ytterbium lasers in Chapter 2 and validating studies, such as the ones described in this and subsequent chapters, are performed at 1030 nm, future versions of the clinical NLM instrument will be able to use lower cost, reliable ytterbium lasers.

This work was done in collaboration with James G. Fujimoto, Tadayuki Yoshitake, Michael G. Giacomelli, and Oscar M. Carrasco-Zevallos at Massachusetts Institute of Technology and James L. Connolly, Liza M. Quintana, Tejas Mehta, Mary Jane Houlihan, Monica G. Valero, Yaileen D. Guzman-Arocho, and Rebecca Gelman at Beth Israel Deaconess Medical Center and Harvard Medical School. The work was supported in part by the National Institutes of Health R01-CA178636-05, R01-CA075289-20, F32-CA183400-02, Air Force Office of Scientific Research AFOSR contracts FA9550-12-1-0551 and FA9550-15-1-0473, the MIT Broshy Graduate Fellowship in Medical Engineering and Science, and the MIT Termeer Medical Engineering Graduate Fellowship.

3.2. MATERIALS AND METHODS

Study objectives

The primary objective of this study is to assess the reduction of histopathological indication for repeat breast cancer surgery following *ex vivo* NLM imaging of surgical specimen margins to provide information for possible additional intraoperative excision (shaving), as compared to randomized control patients. The secondary objective of this study is to estimate the sensitivity and specificity of margin evaluation using NLM imaging performed in real time during surgery as compared to conventional histopathology.

Patient recruitment

A total of 98 patients who are scheduled to undergo a lumpectomy for breast cancer at BIDMC are being recruited to participate in this study. Informed consent is obtained for all study participants. All research is being performed according to protocols approved by Dana-Farber/Harvard Cancer Center Institutional Review Board and Massachusetts Institute of Technology Committee on the Use of Humans as Experimental Subjects. This study is registered on ClinicalTrials.gov as NCT02926729, at Dana-Farber/Harvard Cancer Center's IRB as Protocol 16-145, and at Massachusetts Institute of Technology's Committee On the Use of Humans as Experimental Subjects.

The eligibility criteria for study participation is as follows:

Inclusion criteria:

- Woman over the age of 21 scheduled to undergo lumpectomy for breast cancer at BIDMC.
- Core needle biopsy positive for invasive breast cancer or ductal carcinoma in situ (DCIS).
- Estrogen receptor (ER) positive on core needle biopsy, or if receptor negative, have evaluable ER with positive internal control on core biopsy.

- Progesterone receptor (PR) positive on core needle biopsy if biopsy indicates invasive cancer, or if receptor negative on biopsy indicating invasive cancer, have evaluable PR receptor with positive internal control on core biopsy.
- HER2 IHC and/or FISH ordered on core biopsy, if biopsy indicates invasive cancer.
- Oncotype DX or other DNA testing performed on core biopsy or not requested.

Exclusion Criteria:

- Contraindicated for radiation therapy.
- Pregnancy. (Pregnant women will be excluded from this study because radiation therapy is contraindicated during pregnancy.)
- Current invasive cancer or DCIS at the site of a previous surgery.
- Any systemic neoadjuvant (or preoperative) therapy between the core biopsy and lumpectomy.
- Involvement in another therapeutic trial for breast cancer at Dana Farber or elsewhere.
- Risk of poor cosmetic outcome after initial lumpectomy and possible additional excision, as assessed by a study surgeon.
- Recommendation for mastectomy based on radiology.
- Patients that have complex DCIS as indicated on radiology, which would require excising a large tissue volume.
- No or equivocal ER, PR or HER2 testing performed prior to surgery if biopsy indicates invasive cancer.
- No or equivocal ER testing performed prior to surgery if biopsy indicates ductal carcinoma in situ.

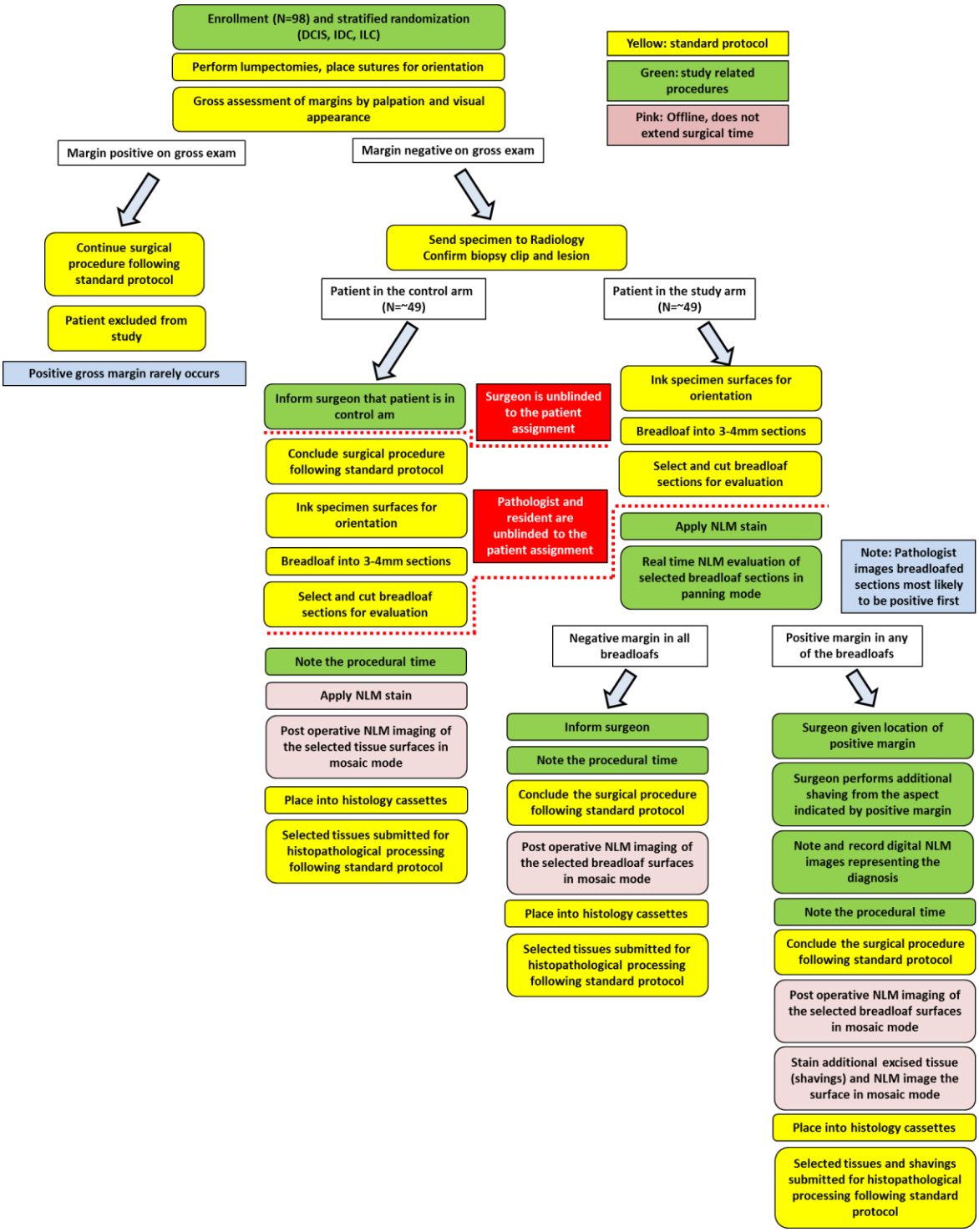

Figure 3.1. Summary of intraoperative evaluation of breast cancer surgical margins study design. From Dana-Farber/Harvard Cancer Center IRB Protocol 16-145.

Study protocol

A summary of the study protocol is shown in **Figure 3.1**. Eligible participants are randomly assigned to the control or study arm to remove treatment selection bias due to factors such as age, race/ethnicity, and tumor size, type and grade. Randomization is stratified into invasive ductal carcinoma, invasive lobular carcinoma, and DCIS groups. Block randomization within the groups is used to balance the assigned arms across groups over time. A study surgeon performs a lumpectomy on patients enrolled in the study blinded to the arm that the patient is in. After excision, the surgeon places sutures in the surgical specimen for orientation following standard procedures. The surgeon examines the gross lumpectomy specimen by palpation and visual inspection to assess the margins. If the surgeon believes that tumor may have been missed based off this assessment, additional shavings around the surgical cavity may be taken as per standard of care.

The excised tissue is transported from the operating room to the radiology breast imaging laboratory via pneumatic tube. The specimen is imaged with x-ray using a surgical specimen radiography system (BioVision, Faxitron Bioptics, LLC), and checked by a study radiologist for the presence of the target lesion and/or biopsy clip and its position relative to the surgical margin following standard procedures. In the event that surgical or radiologic examination of the gross specimen indicates taking additional surgical shavings, data from these shavings are excluded from the study analysis. NLM assessment of additional surgical shavings could increase the number of specimens to be imaged and may excessively prolong surgical times, so the data from these cases are excluded.

Following radiography, the surgical specimen is grossed according to standard pathology protocols. First, the surfaces of the specimen are inked with different colors for orientation using

tissue marking inks. The tissue marking inks are commercial surgical inks that have been mixed with small fluorescent plastic beads to enable visualization under NLM (see details below). The surgical specimen is then cut into 3-4 mm breadloafed slices. The breadloafed slices are selectively sampled for histological evaluation according to standard institutional protocols. For a specimen with invasive ductal carcinoma (IDC), standard protocol samples each ~1 cm of the longest dimension of the specimen with a typical total of 5-10 breadloafs, such that all margin aspects are represented at least once in the breadloafed slices. For a specimen with ductal carcinoma in situ (DCIS), it is recommended that all breadloafed slices are examined. Therefore, larger DCIS specimens have a larger number of breadloaf slices to evaluate (the number of sections varies but typically DCIS specimens generate 10 to 20 breadloaf sections). The pathology fellow, resident or technician are blinded to the patient status during this standard procedure of specimen breadloafing and selection of breadloafed slices for postoperative histological assessment in order to prevent any selection bias.

The study surgeon is informed of the patient randomization assignment immediately following radiography in order to avoid prolonging the surgery. The pathology fellow, resident or technician is informed of the patient randomization assignment following selection of breadloafed slices. The patient assignment is communicated by study staff not blinded to the patient assignment. For patients in the control arm, the surgeon does not receive intraoperative NLM feedback and concludes surgery according to standard protocols.

For patients in the study arm, the selected breadloafed slices are evaluated by a pathologist in real time using the NLM instrument. After NLM evaluation, the pathologist informs the surgeon whether invasive cancer was seen at the margin or DCIS was seen within 2 mm of the surgical margin (the convention for close margins used by BIDMC). Based on this information, the

surgeon may decide to perform additional shavings from the lumpectomy cavity. The study surgeon then concludes the surgery following standard procedures. The selected breadloafed slices and any additional shavings are then submitted for postoperative histopathological processing and evaluation of FFPE histology following standard protocols. Digital images, diagnoses, and imaging time will be recorded during real-time evaluation of the specimens.

Following postoperative histopathological processing, histology slides from the selected breadloafed slices as well as surgical shavings are evaluated by a pathologist. The surgical margin status and recommendation for repeat surgery are determined using standard clinical postoperative histopathology protocols.

The diagnostic accuracy of the NLM imaging will be defined as the rate of true positives and true negatives on NLM imaging compared to postoperative histopathology. The intraoperative accuracy will be determined by comparison of the individual intraoperative margin assessments with the matched diagnosis from the postoperative histopathology evaluation of the specimen margins.

Patient follow up

The study surgeon performs routine follow up with each patient as per the standard of care. During this time, the surgeon notes any complications, such as infections, for adverse event reporting. Study follow up extends until routine postoperative care is concluded or one month, whichever is less.

Sample size

The primary objective is to demonstrate a reduction in the indication for repeat surgeries for close or positive margins in the NLM imaging group versus a randomized control group. Using a one-sided 0.05 Fisher exact test, with 47 patients per arm, there would be 90% power to decide the

control arm has a significantly larger percent of patients with positive or close margins than the NLM arm if the true percentages of positive margins were 30% for the control and 6% for the study arm. We believe these fractions are realistic based on our preliminary data and the approximate rate of repeat surgery for BIDMC.

The secondary objective is to assess the diagnostic accuracy of intraoperative NLM compared to postoperative histopathology. If the true prevalence of positive/close margins is 30%, then the expected number of patients with positive/close margins is 14, and there is an 80% chance of having at least 12 patients with histologic positive/close margins on which to evaluate NLM sensitivity. If all 12 patients have positive/close margins on NLM, the 95% CI for sensitivity would be 78-100%. Similarly, there is an 80% chance that specificity would be based on at least 33 patients; if none of them had positive/close margins on NLM then the 95% CI for specificity would be 91-100%.

Finally, we expect that approximately 4% of the patients randomized on this study will have grossly positive margins (by palpation or by visual examination) prior to NLM imaging. These patients will be given standard therapy for grossly involved margins, will not be treated according to this protocol, and will be excluded from the analysis. For this reason, the accrual goal of this study will be approximately 4% more than the sample size needed for the power specified above, for a total of 98 patients.

Detailed specimen preparation

Inking protocol

During tissue grossing, six different colored tissue marking inks are applied to the surface of the specimen to orient the specimen back to the surgical cavity (**Table 3.1**). The tissue marking inks are fixed onto the specimen with vinegar. Black marks the anterior margin, violet: posterior,

blue: superior, green: inferior, orange: medial, and yellow: lateral. Commercial tissue marking inks are used in standard pathology practice. However, these tissue marking inks can be difficult to visualize using NLM due to their inconsistent or non-existent fluorescence emission at the excitation and detection wavelengths used in the NLM instrument. Black, violet, blue, and green tissue marking inks are weakly or non-fluorescent. Orange and yellow ink have strong fluorescence emission that can saturate the NLM photomultiplier tubes (PMTs). It was found that orange ink from Mercedes Scientific and yellow ink from Thermo Fisher Scientific have the lowest fluorescent emission from several commercial vendors and do not saturate the NLM PMTs and are therefore used in this study.

Margin	**Ink Color**	**Ink brand**	**Bead Color**
Anterior	Black	Cancer Diagnostics, Inc (CDI, SKU: 0728-1)	Red
Posterior	Violet	CDI, SKU: 0728-7	Green
Superior	Blue	CDI, SKU: 0728-2	Red
Inferior	Green	CDI, SKU: 0728-3	Green
Medial	Orange	Mercedes scientific, MER DYE2OZO	Red
Lateral	Yellow	Thermo Fisher Scientific, REF 5000Y	Green

Table 3.1. Tissue marking ink used to orient breast specimens. Red and green beads appear in separate NLM color channels. To better differentiate tissue marking ink colors, red and green beads are alternated on adjacent inks.

To ensure that inks had a consistent appearance when visualized using NLM, small red and green fluorescent beads (5% of mass of surgical ink, Technoglow UVP-RRD-E and UVP-GRN-E) are mixed into the commercial inks. Alternating red and green beads are mixed into inks that are adjacent to each other on the specimen so that they appear in different NLM channels (red

appears in the sulforhodamine 101 channel and green appears in the acridine orange channel). The fluorescent beads were chosen due to their solubility in xylene, which is used during the post-operative tissue paraffinization process, so that they do not interfere with post-operative FFPE evaluation.

Tissue grossing and staining

After applying the tissue marking inks, a pathology fellow or resident breadloafs the breast tissue into 3-4 mm thick specimens with a scalpel. The unprocessed specimens are stained in a 50% ethanol solution containing acridine orange (40 µg/ml; #10050, Electron Microscopy Sciences) and sulforhodamine 101 (40 µg/ml; S7635, Sigma-Aldrich) for 2 minutes. Acridine orange provides contrast similar to hematoxylin and sulforhodamine 101 stains cytosol and stroma similar to eosin.[51] Multiple specimens can be stained in parallel reducing tissue preparation time. The specimens are then rinsed for 30 seconds in saline to remove excess dye and placed on a specimen holder with a glass window (glass thickness of 400 µm) for imaging with a nonlinear microscope. A standard webcam, mounted below the specimen holder, provides a real time video stream of the surface of the glass window. The video stream aids the pathology fellow or resident in ensuring the specimens are flat against the surface of the glass and that all surgical ink is visible. Foam (0.5" thick, 30 pores per inch reticulated polyurethane, item number 88622, United States Plastic Corp.) is used to gently compress the specimens against the glass to ensure contact with the glass and a flat imaging surface. Formalin is added to the specimen holder to start fixing the specimens. The specimen holder is transferred to the NLM instrument. In parallel with the pathologist's evaluation of the initial breadloafed slices, the pathology fellow or resident stain subsequent breadloafed slices in order to minimize the time required to evaluate all specimens.

Imaging protocol

The nonlinear microscope[14] uses a short-pulsed Ti:Sapphire laser (Chameleon Ultra, Coherent, Inc.) at 1030 nm wavelength to excite acridine orange and sulforhodamine 101 fluorescence in a narrow focus, providing visualization of a thin section without physical sectioning. The microscope has two interchangeable objectives: a 10x, 0.45 numerical aperture (CFI Plan Apo Lambda, Nikon) and a 5x, 0.25 numerical aperture objective (Fluar, Carl Zeiss). Fluorescent light from acridine orange and sulforhodamine 101 is detected using two PMTs (H7422-40p, Hamamatsu). A white light camera is integrated into the nonlinear microscope to record a gross view of the specimen.

Specimens are evaluated on the nonlinear microscope in real time in a method similar to the procedure pathologists use with a standard microscope to evaluate histology. Pathologists examine the specimens on a computer monitor showing nonlinear microscopy images at 16 frames/second while translating the specimen to select the nonlinear microscopy field of view. Images resembling FFPE H&E are generated from nonlinear microscopy by displaying the fluorescence signals from the nuclear (acridine) and stromal (sulforhodamine) detector channels in an H&E color scale using an algorithm called Virtual Transillumination Microscopy.[6] A fiducial marker is displayed on the white-light gross image of the specimen indicating the current position of the nonlinear microscopy image to aid in navigation. The objectives can be rapidly changed for variable magnification and focus depth adjusted for visualizing tissue below the specimen surface. The evaluation, including nonlinear microscopy images at known positions, are saved for post-procedural analysis and training. In this mode of operation, a pathologist can rapidly and efficiently evaluate large specimen areas, similar to slide evaluation on a standard histology microscope.

Post-operative processing

After NLM evaluation, the tissue is submitted for standard post-operative tissue processing. Several procedures are used to minimize the difference between the intraoperative NLM imaging plane (which is at the specimen surface) and the post-operative FFPE H&E evaluation plane (which can be cut below the specimen surface) so that the same areas of the margins are being evaluated. First, formalin fixation is started while the specimens are in contact with the glass surface of the specimen holder during NLM imaging. This creates a flat surface when transferring the specimens from the specimen holder to tissue cassettes to complete fixation and paraffin processing. Second, when the specimens are being embedded after tissue processing, the flat surface that was evaluated on NLM instrument is pressed against the embedding mold to ensure that it is parallel to the surface of the paraffin block. Lastly, the microtome blade is carefully aligned to the paraffin block surface to ensure that the sections are parallel to the surface of the block, and the first section in the block that includes all margins is used for FFPE evaluation.

A pathologist evaluates the FFPE histology according to standard practice. Initially, one FFPE H&E slide is evaluated per specimen with additional levels or special stains requested as needed. The results are used to inform treatment decisions and are compared to NLM.

3.3. PRELIMINARY RESULTS

The clinical study is still ongoing and therefore analysis of study results and objectives will not be reported in this chapter. Three example study cases are described to highlight the advantages and difficulties with this study thus far.

Case 1: Invasive ductal carcinoma

In case 1, the patient was diagnosed with invasive ductal carcinoma on biopsy. She was enrolled in this study and underwent a lumpectomy to remove the cancer. This patient was randomized into the study arm. The excised specimen weighed 7 grams and fit into 8 standard histology cassettes (3 x 2.5 x 0.4 cm/cassette). Specimen preparation and NLM analysis required a total of 22 minutes with specimen inking and grossing requiring 9 minutes and NLM evaluation of all surgical margins requiring 13 minutes. During NLM evaluation, the pathologist detected DCIS less than 1 mm from the anterior surgical margin. DCIS less than 2 mm from the surgical margin would typically warrant additional excisions at that margin. However, this patient had no more tissue anterior to the specimen and therefore no additional tissue was removed. The intraoperative NLM finding of DCIS < 1mm from the anterior surgical margin was also seen on post-operative FFPE H&E. The patient did not undergo repeat surgery.

Case 2: Invasive ductal carcinoma

In case 2, the patient was diagnosed with invasive ductal carcinoma on biopsy. She was enrolled in the NLM study and underwent a lumpectomy to remove the cancer. This patient was randomized into the study arm. The excised specimen weighed 10.5 grams and fit into 25 standard histology cassettes. Specimen preparation and NLM analysis required a total of 24 minutes with specimen inking and grossing requiring 11 minutes and NLM evaluation of all surgical margins requiring 13 minutes. During NLM evaluation, the pathologist detected invasive ductal carcinoma touching the inferior surgical margin. The surgeon resected additional tissue from the inferior margin with guidance from the pathologist. The additional resected tissue was not evaluated with NLM. The inferior surgical margin on the original specimen was also found to be positive for invasive ductal carcinoma on post-operative FFPE H&E. The new inferior surgical margin from

the additional resection was negative for carcinoma. In this case, NLM evaluation with intraoperative feedback saved the patient from having to undergo a repeat surgery.

Case 3: Invasive lobular carcinoma

In case 3, the patient was diagnosed with invasive lobular carcinoma on biopsy. She was enrolled in the NLM study and underwent a lumpectomy to remove the cancer. This patient was randomized into the study arm. The excised specimen weighed 33.5 grams and fit into 9 standard histology cassettes. Specimen preparation and NLM analysis required a total of 28 minutes with specimen inking and grossing requiring 11 minutes and NLM evaluation of all surgical margins requiring 17 minutes. During NLM evaluation, the pathologist detected invasive lobular carcinoma touching the inferior surgical margin and within microns of the medial surgical margin. Typically, only invasive carcinoma touching the surgical margin would warrant a repeat surgery, however to be conservative, the surgeon decided to resect additional tissue at both the inferior and medial margins. The additional resected tissue was not evaluated with NLM. The inferior surgical margin on the original specimen was also found to be positive for invasive lobular carcinoma on post-operative FFPE H&E. The closest invasive lobular carcinoma was found to be 2.5 mm away from the medial margin on FFPE H&E, which was discordant with the NLM evaluation. The new inferior and medial surgical margin from the additional resection were negative for carcinoma. In this case, NLM evaluation with intraoperative feedback saved the patient from having to undergo a repeat surgery.

3.4. DISCUSSION

The clinical trial described in this chapter ensures that all subjects in the study and control arm receive the clinical standard of care for surgical margin assessment and the recommendation for repeat surgeries. The only deviation from the standard of care occurs when the pathologist detects positive or close margins upon NLM imaging of the specimens for the patients in the study group. In these cases, the study surgeon is informed by the pathologist and may perform additional surgical shavings in an attempt to achieve a negative margin. Following the conclusion of surgery, the patient receives standard postoperative care. This includes monitoring for immediate complications such as a reaction to anesthesia, deep vein thrombosis or bleeding, as well as long-term complications such as infection. Any complications noted for both control and experimental subjects are recorded. Lumpectomy is a well-tolerated procedure and serious complications are uncommon. No serious adverse events have been reported in the initial study subjects.

The nonlinear microscope and imaging methods have been developed for increased speed, reduced training requirements, and minimal changes to specimen processing. The nonlinear microscope is operated in real time during surgery reproducing the functionality of a conventional histology microscopy. The pathologist can pan around the specimen and rapidly change imaging magnifications. The NLM images are displayed in an H&E format and surgical inks are made visible by dissolvable fluorescent beads. The microscope operates at video rate and has a rapidly translatable stage enabling comprehensive evaluation of entire surgical margins in surgically feasible times. The specimens are carefully fixed, processed, and cut to minimize the differences between the NLM evaluation plane at the specimen surface and the FFPE H&E slide.

In the three example cases described in the results section, 2 subjects were saved from a repeat surgery due intraoperative NLM feedback and additional margin resections. In the third case,

additional tissue was resected at the medial margin based on intraoperative NLM feedback that invasive carcinoma was near that margin. However, based on post-operative FFPE H&E analysis, the additional tissue resection at the medial margin was unnecessary. The reason for the discrepancy in the position of invasive carcinoma found on NLM versus FFPE H&E (within microns on NLM versus 2.5 mm from the margin on FFPE H&E) is likely due to a difference in evaluation planes. Even though the protocol described attempts to minimize these differences by carefully controlling the plane of evaluation, it is almost impossible to achieve perfect co-registration of NLM and FFPE H&E since tissue processing, paraffin embedding, and microtome sectioning can all introduce alterations in the slide that is eventually evaluated on FFPE H&E.

In the three example cases, the intraoperative NLM evaluation required 22, 24, and 28 minutes from tissues of various sizes. The evaluation times depend on several complex and interconnected factors including the size of the specimen, the number of breadloafed slices evaluated, the complexity of disease, the proximity of the disease to the margin, the focality of the disease, and the experience of the pathologists. For example, in cases where the tumor is well delineated and far from the margin and the specimen has few suspicious glandular or ductal structures, the pathologists can rapidly and easily evaluate margins regardless of size of the specimen. However, if carcinoma is near margins in many places, the pathologists require additional time to review margins. The evaluation times reported here are only preliminary results and analysis of all results will be required. It is important to note that the duration of NLM evaluation does not directly translate into the duration of surgical delay. In lumpectomies of patients with invasive carcinoma, lymph node dissection is performed after removing the tumor. Therefore, NLM evaluation can be performed while other surgical procedures are taking place.

Intraoperative evaluation of breast cancer surgical margins using NLM is a promising method for reducing repeat surgeries. However, the full study described in this chapter will need to be completed before statistical analysis of the results can be performed. The full study results will be reported when all 98 patients have been enrolled and the data has been analyzed.

Chapter 4
NLM evaluation of prostatectomy specimens

4.1. INTRODUCTION

Prostate cancer is the highest incidence malignancy in the U.S. male population, with a projected estimated 248,000 new cases and 34,000 deaths attributed to the disease in 2021.[59] Treating localized prostate cancer with radical prostatectomy provides good oncological outcomes and long-term survival benefits.[60,61] Nerve-sparing radical prostatectomies are favored if cancer does not involve the neurovascular bundles as patients have better recovery of sexual function and urinary continence.[62–71] However, identifying patients eligible for nerve-sparing can be challenging using existing preoperative staging methods, leading to a higher rate of non-nerve sparing radical prostatectomies than necessary.[72–75] Comprehensive intraoperative evaluation of prostate surgical margins using frozen sections has been shown to increase rates of nerve-sparing radical prostatectomies, while decreasing positive surgical margin rates.[76,77] However, comprehensive frozen section assessment of margins is time and labor intensive, which is impractical and expensive for many hospitals.[76,78] Techniques that can rapidly evaluate fresh surgical specimens without freezing and microtome sectioning are therefore needed.

Prostate specimen imaging has been investigated using optical techniques such as structured illumination microscopy[9,10], optical coherence tomography[79–82], microscopy with UV surface excitation[11], light sheet microscopy[12], and confocal microscopy[13]. Initial results using these methods have been promising, however studies have largely focused on feasibility and larger scale validation of tissue handling methods, imaging, and quantitative diagnostic accuracy are necessary. Compared with other methods NLM has the advantage that it can image without

physical sectioning, so images are acquired rapidly without loss or destruction of tissue. NLM can image at depths of up to 100 μm[8,14,83,84], avoiding surgical debris, surface artifacts, or areas of electrocautery.[15] This capability is analogous to serial sectioning in histology, except that image depth can be continuously and rapidly adjusted, providing the pathologist with additional information beyond frozen sections. Nonlinear microscopy achieves superior contrast and image quality compared with other imaging modalities[12,15,83,84], making it particularly well-suited for visualizing nuclear and cytoplasmic/stromal detail.

In Chapter 2 and Chapter 3, we demonstrated that NLM can be used to evaluate fresh breast tissue surgical specimens.[6,8,19] Other groups have used NLM to identify prostate architecture in both rat[85,86] and human[87], however, NLM has not been used to evaluate fresh prostate tissue with nuclear and stromal/cytoplasmic contrast generating images analogous to paraffin H&E slides. In Section 4.2. , we describe a method for preparing and imaging centimeter-scale, fresh prostate tissue using NLM. We compare NLM imaging of fresh and fixed, benign and malignant prostate tissue with paraffin embedded H&E slides. In Section 4.3. , we use the results from Section 4.2. to perform a multi-pathologist blinded reading study of NLM images from 122 freshly excised prostate tissue specimens to assess the accuracy of NLM for detecting carcinoma. The work in this chapter was first published in Modern Pathology in separate two papers. Section 4.2. was published as "Comparing histologic evaluation of prostate tissue using nonlinear microscopy and paraffin H&E: a pilot study" by Cahill, *et al.*.[7] Section 4.3. was published as "Nonlinear microscopy for detection of prostate cancer: analysis of sensitivity and specificity in radical prostatectomies" by Cahill, *et. al.*.[88]

This work was done in collaboration with Tadayuki Yoshitake, James G. Fujimoto, Michael G. Giacomelli, and Oscar M. Carrasco-Zevallos at Massachusetts Institute of Technology and

Yubo Wu, Douglas I. Lin, Huihui Ye, Cecilia Ponchiardi, Andrew A. Wagner, and Seymour Rosen at Beth Israel Deaconess Medical Center and Harvard Medical School. The work was supported in part by the National Institutes of Health R01-CA178636-05, R01-CA075289-20, F32-CA183400-02, Air Force Office of Scientific Research AFOSR contracts FA9550-12-1-0551 and FA9550-15-1-0473, the MIT Broshy Graduate Fellowship in Medical Engineering and Science, and the MIT Termeer Medical Engineering Graduate Fellowship.

4.2. COMPARING HISTOLOGIC EVALUATION OF NLM AND PARAFFIN H&E

4.2.1. INTRODUCTION

In Section 4.2. , we describe a method for preparing and imaging centimeter-scale, fresh prostate tissue in minutes using nonlinear microscopy with exogenous fluorescent contrast agents and virtual H&E color display. We compare nonlinear microscopy imaging of fresh and fixed, benign and malignant prostate tissue with paraffin embedded H&E slides.

4.2.2. MATERIALS AND METHODS

Tissue Preparation

Seventy specimens (15 cancer, 55 benign) of fresh and fixed prostate tissue (**Table 4.1**) were collected from 24 patients who underwent a prostatectomy. All research was performed according to protocols approved by Beth Israel Deaconess Medical Center Committee on Clinical Investigations and Institutional Review Board and Massachusetts Institute of Technology Committee on the Use of Humans as Experimental Subjects. Informed consent was waived by both committees.

Specimens (patients)	Fresh	Fixed	Total
Cancer	13 (8)	2 (2)	15 (10)
Benign	24 (7)	31 (7)	55 (14)

Table 4.1. Summary of prostate tissue specimens evaluated using nonlinear microscopy and corresponding paraffin H&E.

Fresh and fixed tissue specimens were stained in acridine orange (40 µg/ml) and sulforhodamine 101 (SR101 40 µg/ml) in a 1:1 ethanol:water solution for 2 minutes and rinsed for 30 seconds in phosphate-buffered saline (**Figure 4.1**A). Acridine orange provides nuclear contrast, analogous to hematoxylin, while sulforhodamine 101 provides stromal and cytoplasmic contrast analogous to eosin. These fluorescent stains are advantageous because they rapidly penetrate fresh tissue, can be removed to undetectable levels with standard histology solvents[8], and can be excited at a wide range of wavelengths, making them amenable to nonlinear microscopy. Unsectioned tissue was placed on a glass coverslip and compressed with biopsy foam to provide a flat imaging surface.

Image acquisition and processing

Nonlinear microscopy was first used to image the unsectioned prostate tissue in real-time (**Figure 4.1**B), by translating the specimen in the x-y plane, with interchangeable magnification objectives, analogously to the way a traditional light microscope is used to view slides.[14] The specimen z axis was actuated up and down to focus at different depths up to 50 to 100 µm below the prostate tissue surface (enabling serial sectioning without having to physically section). H&E color display was adjustable to suit user preference. This method can enable rapid evaluation of margins as well as focal pathology, since specific regions of interest can be quickly selected and examined under operator control.

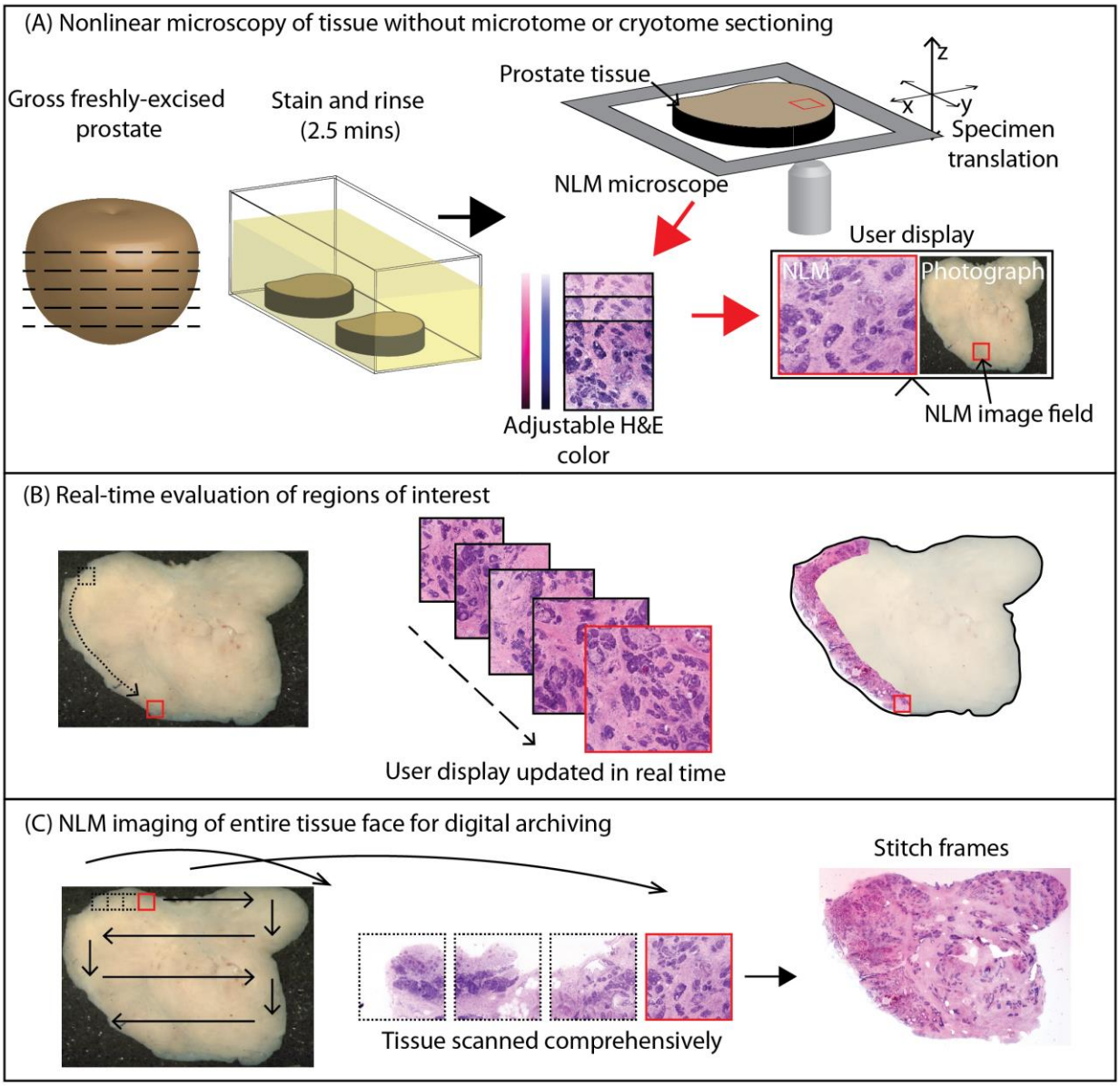

Figure 4.1 Method for evaluating prostate specimens using nonlinear microscopy. (A) The prostate specimens were transected, cross sections were rapidly stained with acridine orange and sulforhodamine 101, rinsed and then placed on the nonlinear microscope stage. 10X and 20X objectives were used to visualize the tissue. The tissue was translated in the x, y, and z direction to examine the entire cross section of tissue (whole mount) up to 100 µm in depth (analogous to serial sectioning). The H&E color display was generated using the acridine orange and sulforhodamine 101 fluorescence signals. The user display showed a photograph (right side) of the prostate cross section and a high magnification nonlinear microscopy (NLM) image (left side) of

a user selected region of interest (marked in red). (B) For real time intraoperative consultation, the user can translate the specimen in the x-y direction to rapidly view different regions and change the focus in the z direction to view different depths. The images can be recorded to create a digital record. (C) Nonlinear microscopy can also automatically image the entire specimen cross section by stitching multiple high magnification fields. This operating mode is too time consuming for intraoperative consultation, but is useful for digital archiving purposes (analogous to slide scanning) and for comparing nonlinear microscopy images to standard paraffin embedded H&E slides.

A nonlinear microscopy image of the entire tissue cross section was also acquired by imaging multiple high magnification overlapping regions (**Figure 4.1**C), at or slightly below the tissue surface. The frames were stitched using Microsoft Image Composite Editor. This produces a digital archive image which can be viewed analogously to a whole slide image generated by a slide scanner. Operating in this scanning mode requires significant delay in evaluation and is not feasible for real-time analysis, but enables comparison of nonlinear microscopy images with paraffin embedded H&E as well as archiving and assessment by multiple readers.

Nonlinear microscopy images were acquired using either a 10x, 0.45 numerical aperture (NA) air objective (CFI Plan Apo Lambda, Nikon) or a 20x, 1.0 NA water immersion objective (XLUMPFL20XW 1.0 NA, Olympus) in one of three microscope configurations previously described[8,14] and shown in **Table 4.2**. In all configurations, a Ti:Sapphire laser was used. A 590 nm high-pass dichroic beam splitter split the fluorescent emission light through two emission filters (ET540/40m, Chroma Technology and FF01-650/60, Semrock) onto two photomultiplier tubes (H7422-40p, Hamamatsu) to detect the acridine orange and sulforhodamine 101 fluorescence.

Objective lens mag. (immersion)	**Frame size** (mm)	**Pixel size** (μm)	**Excitation wavelength** (nm)
20x (water)	0.512x0.512	0.5	780
10x (air)	1.08x1.08	0.75	780
10x (air)	2.048x2.048	1	1030

Table 4.2. Nonlinear microscope configurations.

After nonlinear microscopy imaging, the fresh prostate tissue specimens were fixed in formalin for a minimum of 12 hours on the glass coverslip to maintain orientation and limit tissue shrinkage. Both the tissue specimens that were imaged fresh and fixed by nonlinear microscopy were then processed for standard paraffin embedded histology by pressing the imaged face into the embedding mold to maintain specimen flatness, microtomed into 5 μm sections, and stained with hematoxylin and eosin. The paraffin H&E slides were scanned with a digital slide scanner (20x magnification, Aperio) then the image size was scaled and rotated to match the nonlinear microscopy images and correct for minor shrinkage due to dehydration and paraffinization.

Tissue evaluation

Three genitourinary pathologists evaluated H&E slides and nonlinear microscopy images in an unblinded observational reading. The main analysis was done by SR, who has over 25 years of experience. Nonlinear microscopy digital images were viewed in OpenSeadragon, a web-based viewer that enables variable magnification review. Paraffin H&E slides or scanned slides were evaluated using a histology microscope or with OpenSeadragon. Similarities and differences between nonlinear microscopy and paraffin H&E were characterized.

4.2.3. RESULTS

Nonlinear microscopy enables visualization of normal prostate architecture, benign conditions, and prostate carcinoma.

Prostate architecture

Examples of prostate tissue architecture acquired using nonlinear microscopy on freshly excised, unfixed specimens and corresponding paraffin H&E slide images are shown in **Figure 4.2**. An outer layer of flattened cuboidal basal cells (blue arrow) and an inner secretory layer (orange arrow) of columnar cells with abundant cytoplasm and mainly uniform nuclei positioned basally are clearly visualized in benign ducts (**Figure 4.2**, A and B). Neural bundles with ganglion cells, with their abundant cytoplasm, appear similar in nonlinear microscopy images (**Figure 4.2**, C) and paraffin H&E slides (**Figure 4.2**, D). The appearance of stroma in nonlinear microscopy images of freshly excised, unfixed tissue (**Figure 4.2**, E) is denser than that of paraffin H&E sections (**Figure 4.2**, F). The fixation, dehydration, and physical sectioning required to obtain a paraffin H&E slide is most likely responsible for these differences. Additional differences between nonlinear microscopy and paraffin H&E include the prominent pink appearance of inner elastic lamina of arteries in nonlinear microscopy (**Figure 4.2**, G) that is not present on paraffin H&E (**Figure 4.2**, H).

A comparison of normal prostate architecture visualized by nonlinear microscopy imaging of fixed tissue that was not processed or microtomed for paraffin histology versus standard H&E stained paraffin sections is shown in **Figure 4.3**. An artery (**Figure 4.3**, A and B), characterized by its spindle shaped smooth muscle cells with elongated nuclei, is shown alongside a vein. The lumens of these vessels are filled with red blood cells. In typical analysis of paraffin sections using an ordinary microscope, colors other than the pink and blue from hematoxylin and eosin are seen. Nonlinear microscopy images are generated using only two discrete fluorescent color channels, so the red blood cells do not appear red as they do in the paraffin H&E sections, and instead appear pink. Ejaculatory ducts display characteristic mucosal folds and pseudostratified columnar

epithelium in nonlinear microscopy (**Figure 4.3**, C) matching that of the corresponding paraffin H&E (**Figure 4.3**, D). Of note, nonlinear microscopy images of fixed tissue that was not processed or microtomed for paraffin histology did not have apparent differences from nonlinear microscopy images of freshly excised, unfixed specimens. The use of fixed tissue increased tissue availability and enabled us to assess the possibility of using nonlinear microscopy for examining smaller tissue fragments (core biopsies) which could be fixed while being imaged.

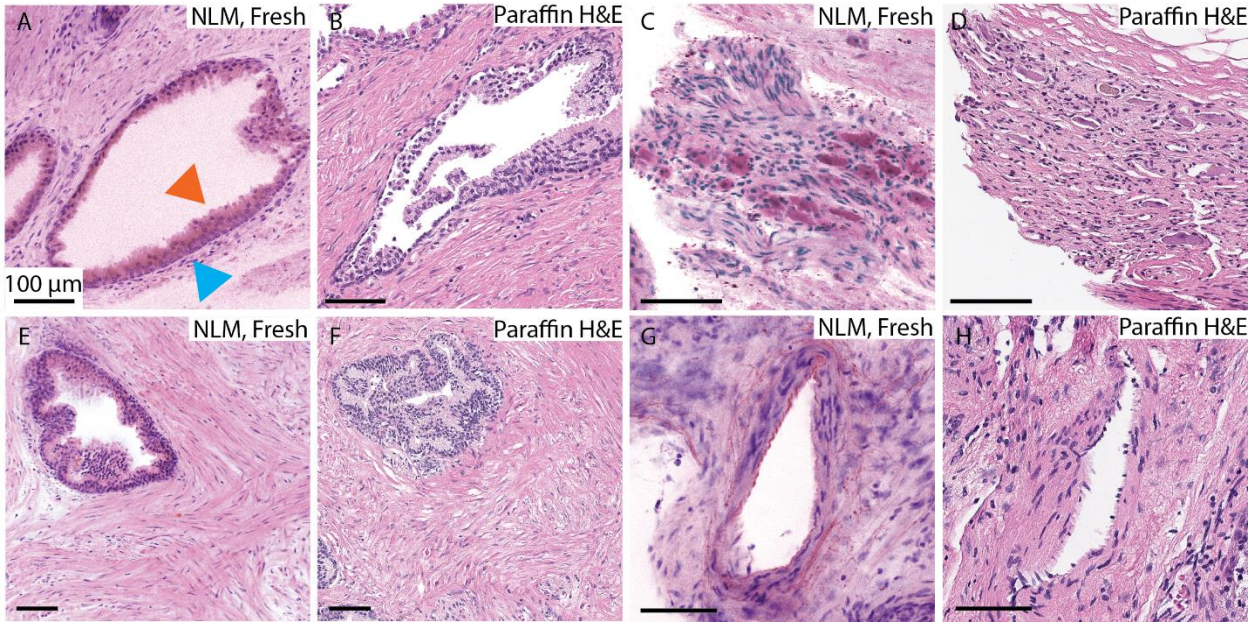

Figure 4.2. Examples of prostate tissue architecture visualized using nonlinear microscopy imaging of freshly excised, unfixed specimens that were not physically sectioned versus corresponding standard paraffin embedded H&E slides after standard histological processing. (A) Nonlinear microscopy and (B) paraffin H&E of benign ducts with basal (blue arrow) and secretory (orange arrow) layers (20x objective), (C) nonlinear microscopy and (D) paraffin H&E of a neural bundle (10x objective, 0.75 µm pixel), (E) nonlinear microscopy of stroma (10x objective, 0.75 µm pixel) with (F) corresponding paraffin H&E, and (G) nonlinear microscopy and (H) paraffin H&E of an artery (10x objective, 1 µm pixel). All scale bars are 100 µm.

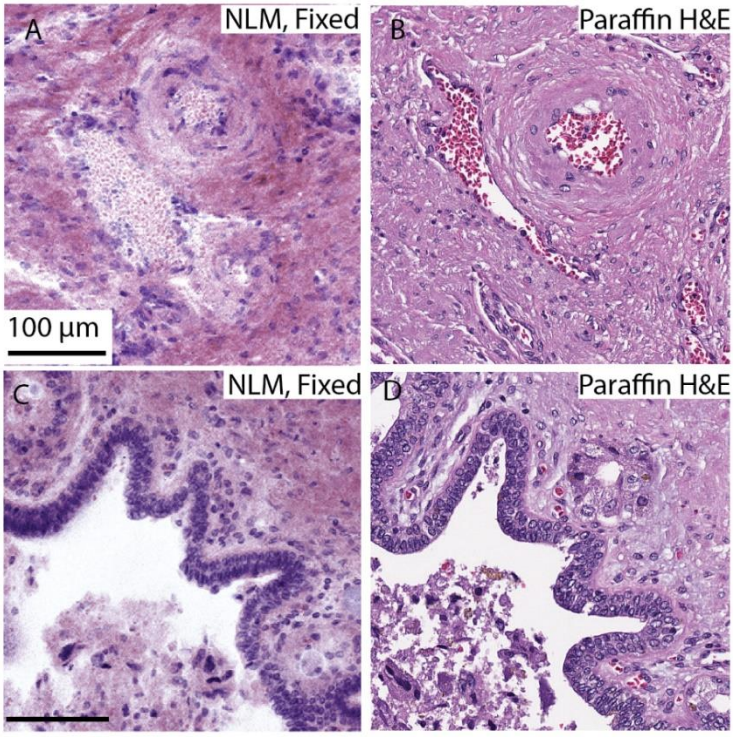

Figure 4.3. Examples of prostate tissue architecture visualized by nonlinear microscopy imaging of fixed tissue that was not processed or physically sectioned versus corresponding standard paraffin embedded H&E slides. An artery and vein (A and B) and ejaculatory ducts (C and D) are shown. Scale bars are 100 µm. (10x objective, 0.75 µm pixel).

Benign conditions

Nonlinear microscopy images of fixed prostate tissue that was not processed or microtomed for paraffin histology and the corresponding paraffin H&E slide from a patient who underwent Bacillus Calmette-Guerin therapy is shown in **Figure 4.4**. Necrotizing granulomatous inflammation is apparent in both the nonlinear microscopy and paraffin H&E with central regions of necrosis, giant cells (yellow arrow), and palisading histiocytes (red box). Benign, atrophic single-layer basophilic glands, as indicated by the flattened epithelium, decreased cytoplasmic volume and dilated lumen, are seen throughout the tissue (blue arrow).

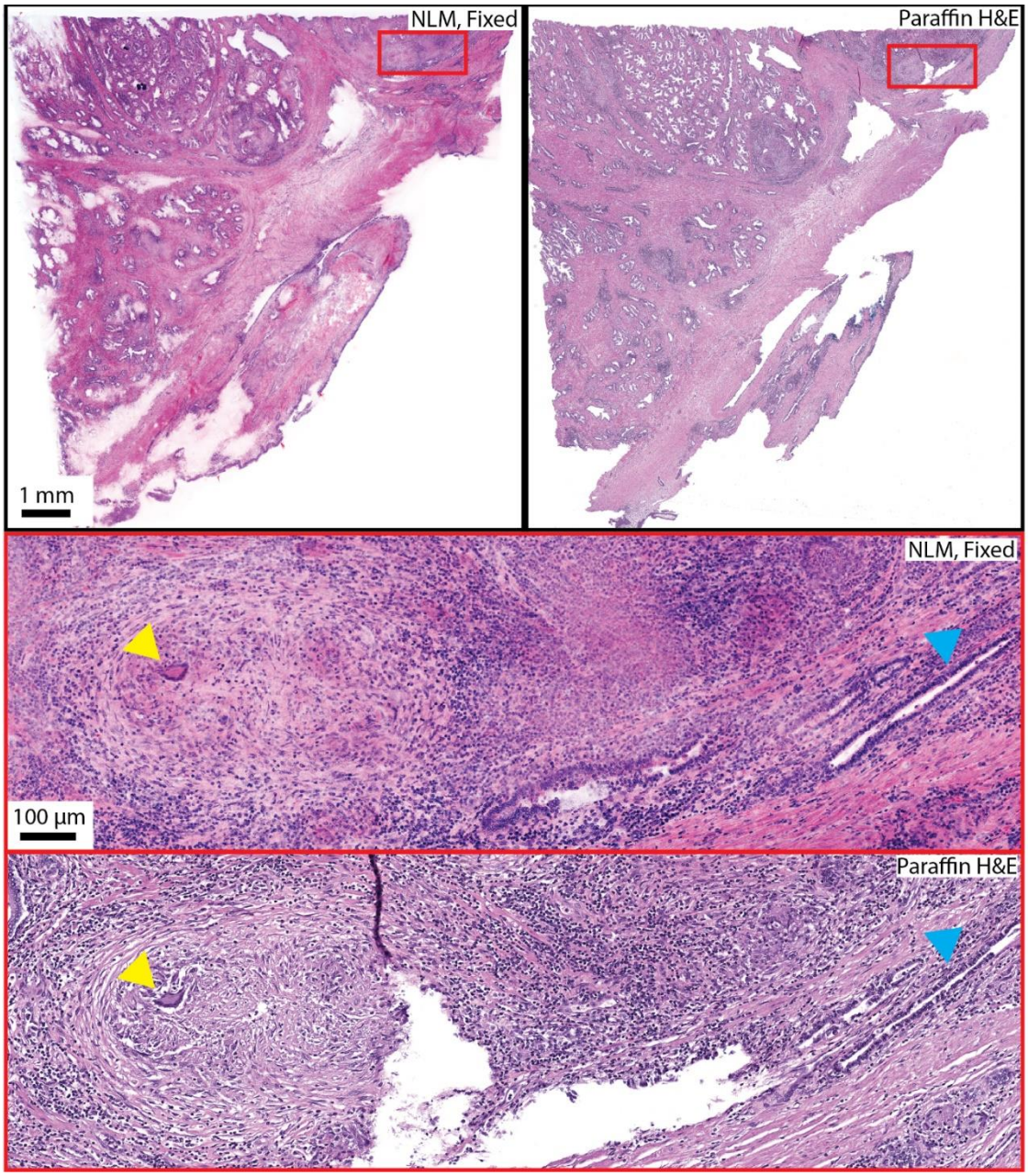

Figure 4.4. A prostate specimen from a patient who underwent Bacillus Calmette-Guerin therapy. The characteristic histological patterns of this therapy are evident in nonlinear microscopy images of the fixed, unsectioned specimen and corresponding paraffin embedded H&E slide, including granulomatous inflammation (red) with giant cells (yellow arrow) and atrophic glands (blue arrow). (10x objective, 0.75 µm pixel).

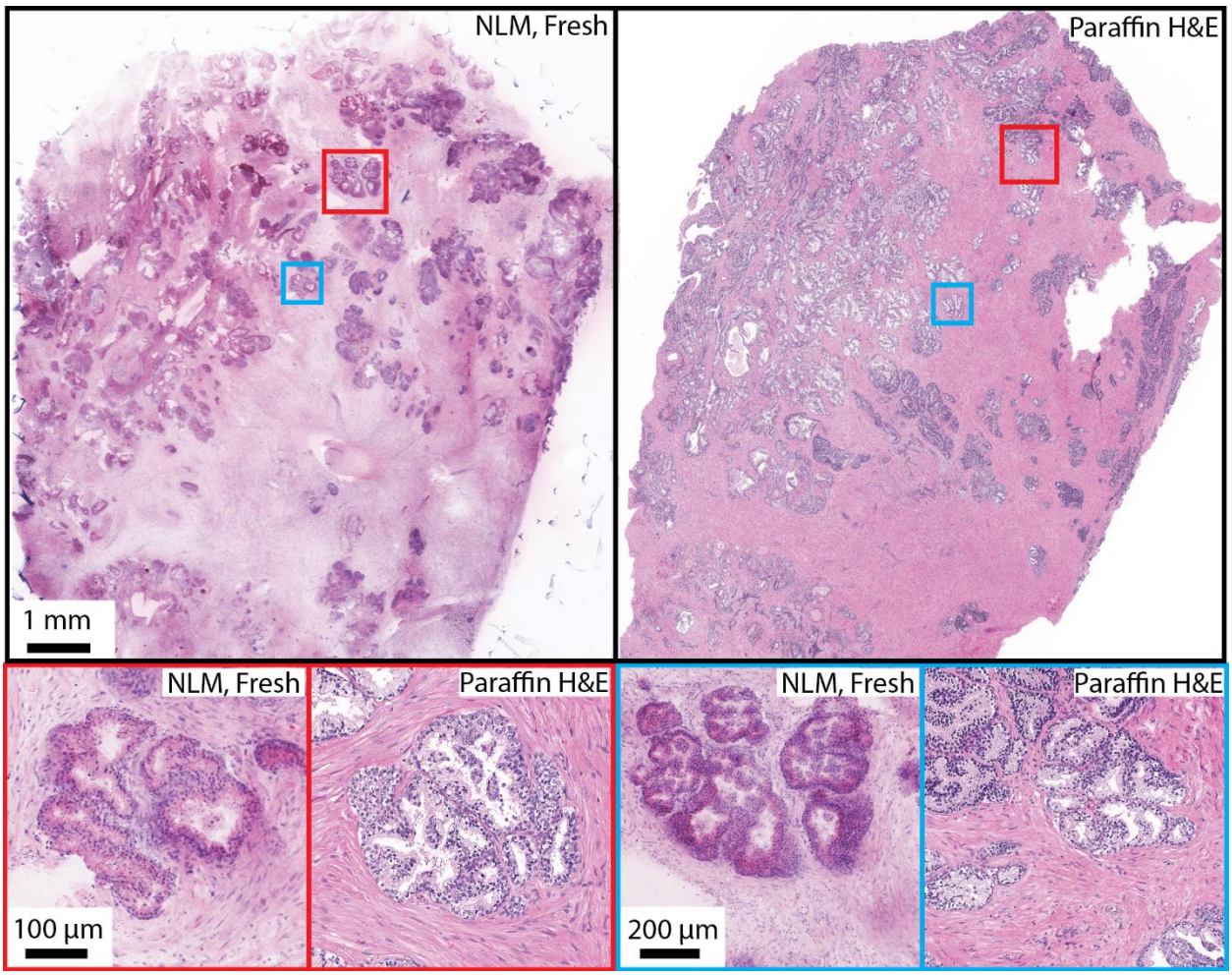

Figure 4.5. Nonlinear microscopy images of a freshly excised, unfixed specimen with benign prostatic hyperplasia and corresponding paraffin H&E slide. Complex hyperplastic glands are abundant throughout the tissue (red and blue box). (10x objective, 0.75 µm pixel).

Nonlinear microscopy images of freshly excised, unfixed prostate tissue with benign prostatic hyperplasia and the corresponding paraffin H&E slides are shown in **Figure 4.5**. Stromal and glandular hyperplasia is clearly visualized in nonlinear microscopy with nodules made up of complex benign glands with luminal papillary projections throughout the tissue (red, blue).

Carcinoma

Differentiating prostate carcinoma versus benign conditions is important for both histologic diagnosis and tumor margin evaluation. Nonlinear microscopy enables visualization of prostate carcinoma with some features closely resembling those of paraffin H&E and other features that differ, but are recognizable. Discriminating between cancerous and benign glands requires appreciation of cellular aspects such as nuclear size and nucleoli, while determining the histologic grade (Gleason score) is more reliant on visualization of glandular architectural features.

An example of a nonlinear microscopy image of fixed prostate tissue that was not processed or sectioned for paraffin histology and a corresponding paraffin H&E slide from a patient with typical adenocarcinoma (Gleason 7 (4+3)) is shown in **Figure 4.6**. Prominent nucleoli of enlarged nuclei are evident on the nonlinear microscopy images (orange box), however, the color of the cytoplasm in the nonlinear microscopy images is different than of the paraffin H&E slide. Despite these differences, it is clear in the nonlinear microscopy image that the dominant tumor component of this prostate section is composed of sheets and cribriform patterns of fused, infiltrative glands consistent with a Gleason pattern 4 which matches that of the paraffin H&E slide (blue, yellow). Well-formed, infiltrating glands of Gleason pattern 3 make up a minority of this carcinoma (red). Benign, atrophic glands can be seen at the periphery of the tumor.

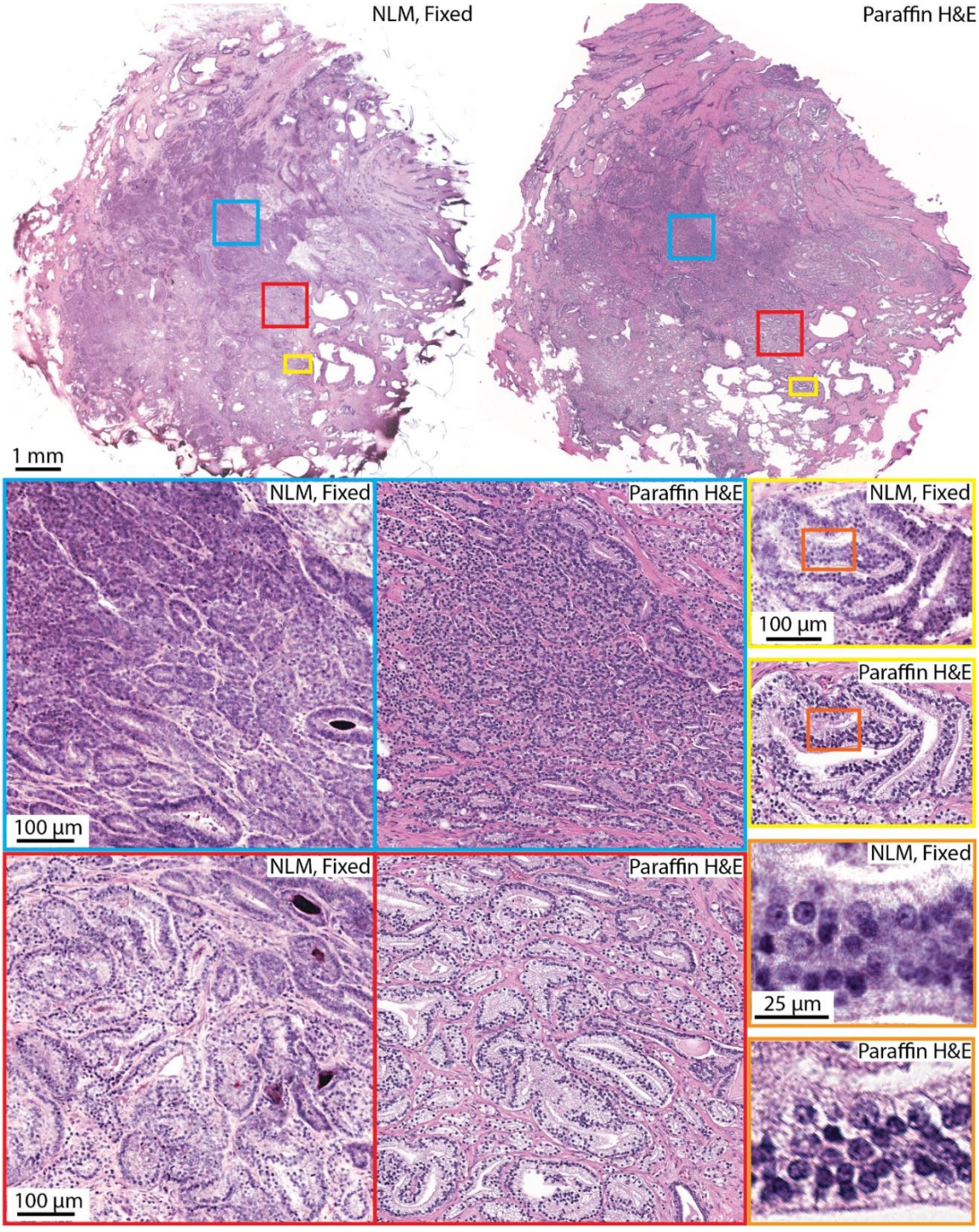

Figure 4.6. A nonlinear microscopy image of a fixed, unsectioned prostate specimen and corresponding paraffin H&E slide from a patient with typical adenocarcinoma displaying Gleason pattern 4, with ductal features (blue, yellow) and 3 (red). The nuclei are enlarged with prominent nucleoli (orange box). (20x objective).

The foamy gland variant of prostate cancer is characterized by abundant foamy cytoplasm due to numerous intracytoplasmic vacuoles. This characteristic foamy appearance is not as prominent in nonlinear microscopy images of freshly excised, unfixed tissue and instead the cytoplasm can appear eosinophilic and even amphophilic as shown in **Figure 4.7**. This is probably due to a combination of factors including insufficient rinsing of the fresh tissue, differences in nonlinear microscopy image color display versus transmission microscope visualization of paraffin H&S slides, differences in specificity of fluorophore uptake in fresh tissue versus fixed tissue, and differences in specificity of acridine orange versus hematoxylin. Other features of typical adenocarcinoma, such as prominent nucleoli and enlarged nuclei are less apparent in the foamy variant as seen in both the nonlinear microscopy image of fresh tissue and paraffin H&E slides. In both nonlinear microscopy and paraffin H&E, we can see glands made up of a single layer of cells with smaller, basally located nuclei with abundant cytoplasm (red, blue). Further, intraluminal crystalloids (yellow arrows), which are typically pink and rhomboid in shape in paraffin H&E slides, are present in the nonlinear microscopy images, however, they appear in multiple different colors. The architectural pattern in the nonlinear microscopy images and paraffin H&E slides are consistent and show a foamy cell variant adenocarcinoma invading the fibromuscular tissue with a Gleason score of 6 (3+3).

A nonlinear microscopy image of an entire cross-section (whole mount) of a freshly excised, unfixed prostate specimen from a patient who underwent a radical prostatectomy is shown in **Figure 4.8**. Typical adenocarcinoma is readily apparent in the peripheral zone of the prostate. At higher power, perineural invasion can be seen beside normal nerve fibers among the periprostatic fat indicating extra-prostatic extension. A centrally located ganglion cell can be seen in a nerve fiber bundle with prominent nucleoli.

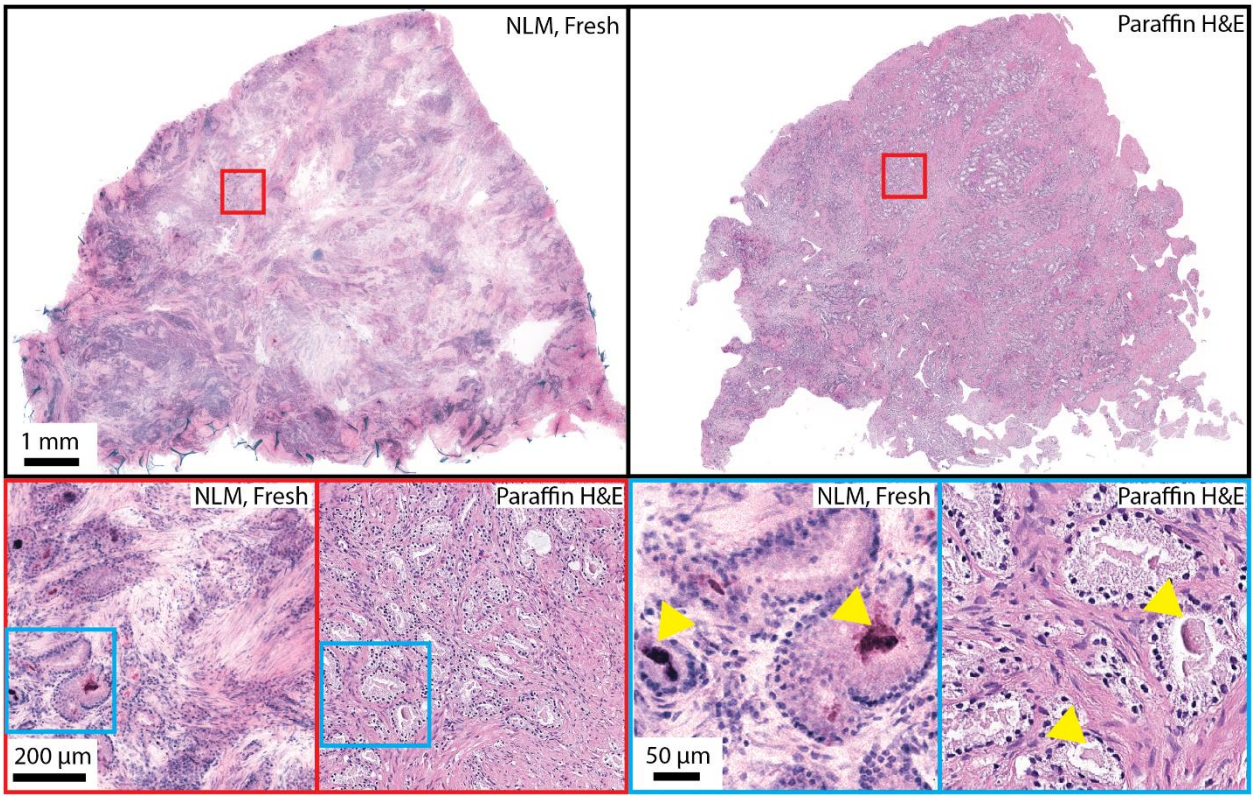

Figure 4.7. A nonlinear microscopy image of a freshly excised unfixed specimen and corresponding paraffin H&E slide exhibiting foamy gland variant of prostate cancer with Gleason score 6 (3+3). The cytoplasm of the cancer cells is less 'foamy' in the nonlinear microscopy images than the paraffin H&E (red, blue). Intraluminal crystalloids (yellow arrows) are present in the images. (10x objective, 0.75 µm pixel).

Figure 4.9 shows an example demonstrating nonlinear microscopy of freshly excised, unfixed prostate tissue that was subsequently processed for paraffin embedded H&E and used for post-operative diagnostic purposes. Nonlinear microscopy was performed in real-time as described in the methods section (**Figure 4.1**B) in order to rapidly identify regions of interest and demonstrate the speed required for intraoperative consultation. A cancer positive margin is apparent on

nonlinear microscopy (red and blue inset) and was identified with only 2.5 minutes of tissue preparation. The prostate photograph shows a grossly apparent tumor abutting the blue ink. Note that since nonlinear microscopy enables visualization of fluorescence and not true color, the ink does not appear as it does on paraffin sections and instead appears washed out with eosinophilic globules making it distinctly recognizable (green arrows). The paraffin section did not show tumor on ink, likely due to levelling of the paraffin block which introduces a discrepancy between the nonlinear microscopy imaging plane and the paraffin section plane.

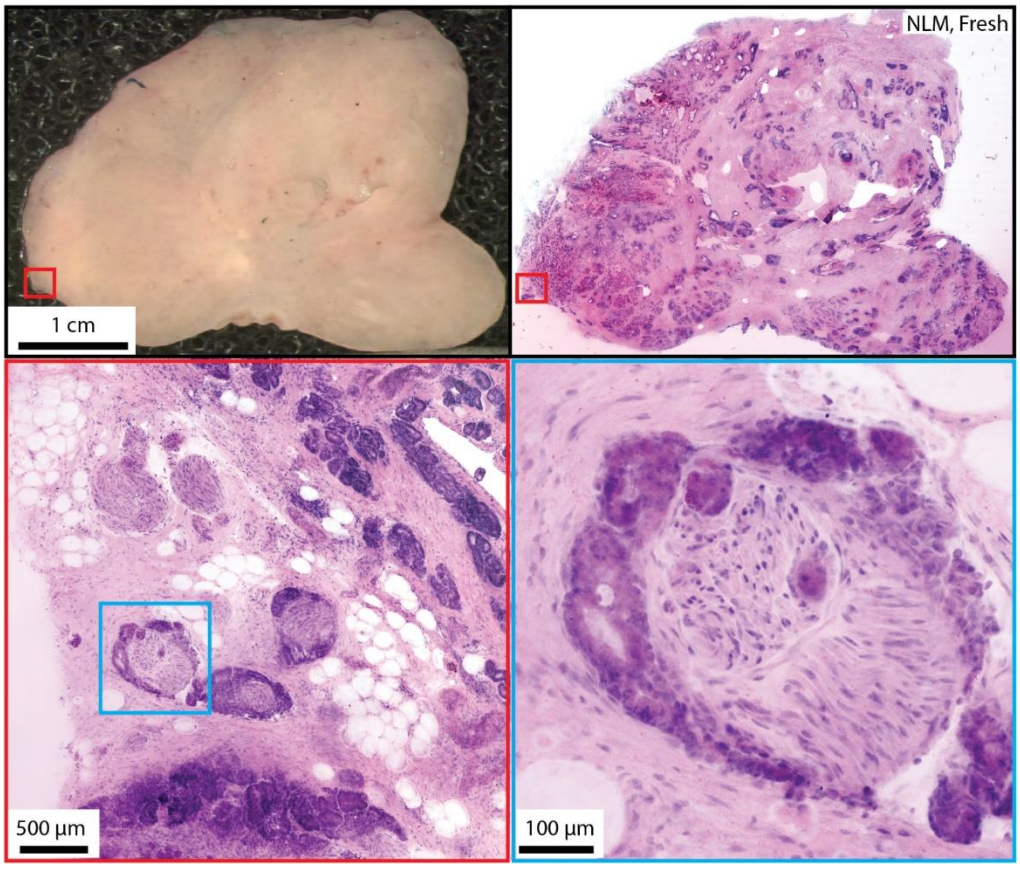

Figure 4.8. A white-light photograph and nonlinear microscopy image of multi-centimeter, freshly excised, unfixed prostate tissue. Extra-prostatic extension and perineural invasion is observed among the periprostatic fat (red and blue). (10x objective, 1 µm pixel).

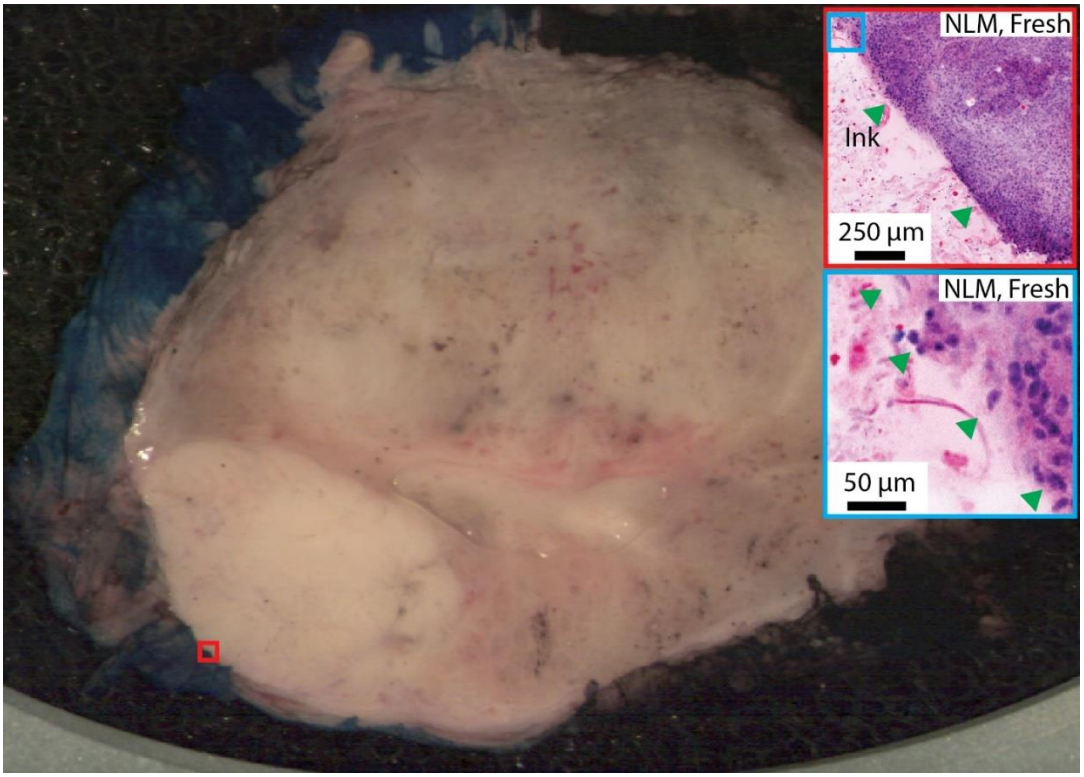

Figure 4.9. A white-light photograph and nonlinear microscopy image of multi-centimeter, freshly excised, unfixed prostate tissue with tumor touching the blue ink. The tumor can be seen touching the ink in the nonlinear microscopy image (red and blue box, green arrows). The paraffin H&E slide did not show tumor touching the ink because of discrepancy between the nonlinear microscopy imaging plane and paraffin embedded H&E section. (10x objective, 1 µm pixel).

4.2.4. DISCUSSION

Nonlinear microscopy using rapid fluorescent stains for nuclear and stromal/cytoplasmic contrast enables prostate tissue evaluation within minutes without physical sectioning. This avoids the freezing and cryotoming required for frozen section analysis. Displaying nuclear and stromal fluorescence signals in H&E colors generates nonlinear microscopy images that resemble standard paraffin H&E histology. This study shows that nonlinear microscopy enables visualization of

benign glands, vasculature, atrophic and hyperplastic glands and stroma, inflammation, and adenocarcinoma, including typical, ductal, and foamy variants. Perineural invasion and extraprostatic extension are also readily apparent. Prominent nucleoli, high nuclear to cytoplasmic ratio, and glandular and stromal architectural patterns enable prostate cancer to be recognized and Gleason patterns differentiated in nonlinear microscopy images.

Despite the similarities between nonlinear microscopy in fresh/fixed unsectioned tissue and paraffin H&E slides, several differences were recognized. Typical histologic features that rely on color (such as bland nuclei or pale pink cytoplasm) are less apparent and consistent in nonlinear microscopy. This is because: (1) Images are generated using two discrete fluorescent color channels rather than white light transmission. Therefore, features that are not due to H&E staining, such as the bright red appearance of red blood cells, are not apparent in nonlinear microscopy images which use nuclear and stromal fluorescence signals to synthesize H&E-like images. (2) Freshly excised, unfixed tissue stains less homogenously than permeabilized, dehydrated tissue in paraffin sections, causing variations in appearance within and between tissues. (3) Acridine orange and sulforhodamine 101 staining in nonlinear microscopy versus hematoxylin and eosin staining of paraffin sections have similar, but not identical, staining specificities. For example, the cytoplasm of foamy variant adenocarcinoma can be darker in nonlinear microscopy images than in paraffin H&E slides.

Other than color differences between nonlinear microscopy and paraffin H&E, freshly excised, unfixed prostate tissue and fixed tissue that was not processed or sectioned for paraffin embedded histology appears different than paraffin H&E sections due to alcohol dehydration, xylene and paraffin infiltration, and sectioning. Alcohol dehydration, used to prepare paraffin H&E slides, causes shrinkage and cytoplasmic retraction which can make features such as stromal fibers and

nuclei more prominent. Understanding these differences enables interpretation of nonlinear microscopy images and facilitates feature mapping between nonlinear microscopy and paraffin H&E.

To provide a direct comparison between nonlinear microscopy images and scanned H&E slides, nonlinear microscopy figures in this chapter were generated by acquiring a series of high magnification nonlinear microscopy images covering the entire tissue cross section surface (**Figure 4.1**C), analogous to a histology slide scanner. This was convenient for digital archiving and multiple reader assessment, but is too time consuming for intraoperative applications.

It is important to note that intraoperative consultation can be performed in minutes, since comprehensive imaging of entire tissue cross sectional faces is rarely required. The edges of the tissue where surgical margins are represented as well as focal regions of interest can be rapidly assessed by translating the tissue under operator control and changing objective magnifications (**Figure 4.1**B and **Figure 4.9**).[14] This operating mode would be comparable in speed to evaluating histology slides using a standard transmission light microscope, except that fresh, unsectioned tissue is imaged rather than paraffin embedded stained slides.

Since positive surgical margins occur after radical prostatectomy in an about 15% (6.5-32%)[89] of patients, frozen section analysis during a prostatectomy has been investigated extensively. The utility of frozen section analysis is controversial since it can be unreliable at predicting histologically positive surgical margins due to incomplete sampling[90], however, frozen section analysis protocols with more thorough sampling using multiple sections, such as those described by Schlomm, *et al.* and Bodman, *et al.*, reduce the rate of positive surgical margins and increase the number of nerve-sparing surgeries.[76,77,91] These sampling techniques are time intensive and require additional infrastructure with a highly optimized workflow, including multiple cryostats,

technologists, and pathologists per patient.[76,78] For example, even with 5 cryostats used in parallel and two pathologists and four technicians working on one patient, Schlomm, *et al.* report an average time of 35 minutes per patient.[76]

In contrast to frozen section analysis, nonlinear microscopy does not involve freezing and cryotoming, so entire cross sections of the prostate can be rapidly processed without dissection into smaller sizes. Furthermore, multiple tissue cross sections can be stained at one time and the pathologist can begin evaluation within 2.5 minutes, while frozen section analysis requires each tissue cross section to be frozen in a separate block and individually cryotomed. The simplicity and work flow advantages of nonlinear microscopy should enable more comprehensive assessment of margins than frozen section analysis in a shorter amount of time with reduced personnel requirements, facilitating wider spread adoption of intraoperative consultation in radical prostatectomy.

Furthermore, since nonlinear microscopy does not require freezing, it is non-destructive and does not have freezing artifacts. Tissue can be subsequently processed for standard paraffin embedded histology and confirmation of nonlinear microscopy findings, as demonstrated in this study. Immunohistochemistry assays (p63, Prostate Specific Antigen, NKX3.1, Cytokeratin 34 beta E12, AMACR) were tested and found to be unaffected by nonlinear microscopy processing and imaging (data not shown) as expected since the fluorescent stains are removed to undetectable levels after standard histology processing. Furthermore, nonlinear microscopy imaging can be performed up to 50 to 100 μm below the tissue surface. This capability is analogous serial sectioning in histology and provides visualization of depth resolved architectural morphology which may give additional insight into pathology or image below surface contaminants such as

surgical debris. Finally, nonlinear microscopy is inherently digital which enables digital archiving and may facilitate future telepathology or computer-assisted diagnostic applications.

Our study is limited because pathologists performed nonlinear microscopy evaluation unblinded to paraffin H&E and used a small number of specimens representing each pathology subtype. Therefore, statistical analysis was not performed. Future studies will be needed to analyze a more extensive set of prostate pathologies and assess the sensitivity and specificity of nonlinear microscopy compared to standard paraffin embedded H&E. Both fresh and fixed specimens were used to increase tissue availability and evaluate the possibility of imaging smaller fragments such as biopsies while they are being fixed. No apparent differences between nonlinear microscopy images of fresh and fixed specimens were seen.

Nonlinear microscopy can be used to assess normal prostate architecture, benign conditions, and carcinoma in both fixed and freshly excised tissue. Images are similar to paraffin H&E slides and imaging can be performed rapidly. Nonlinear microscopy is a promising method for future intraoperative assessment of prostate tissue, however, additional blinded studies are needed to determine its sensitivity and specificity when detecting pathology compared to the gold standard of paraffin embedded H&E histology.

4.3. ANALYSIS OF NLM ACCURACY FOR DETECTING PROSTATE CANCER IN RADICAL PROSTATECTOMIES

4.3.1. INTRODUCTION

In 4.2. we demonstrated a rapid tissue preparation and imaging protocol where freshly excised prostate tissue is stained in a nuclear and cytoplasmic/stromal fluorescent dye then evaluated using NLM.[7,14] This protocol generated images which closely resembled those of corresponding paraffin H&E.[7] Pathologists were able to visualize prostate tissue architecture, secretory and basal cells, inflammation, and stromal and glandular hyperplasia. We also showed that NLM enabled visualization of prostate carcinoma including Gleason patterns, perineural invasion, extraprostatic extension, and positive margins. This previous study provided a qualitative, descriptive analysis of fresh prostate tissue visualized using NLM compared to paraffin H&E, an important first step in interpreting NLM images, but did not quantitatively assess the diagnostic capability of NLM image interpretation. In this section, we report a multi-pathologist blinded reading study of nonlinear microscopy images from 122 freshly excised prostate tissue specimens from 40 patients to assess the accuracy of NLM for detecting carcinoma.

4.3.2. MATERIALS AND METHODS

Specimen Preparation and Imaging

Freshly excised prostate tissue was collected from patients who underwent a radical prostatectomy using protocols approved by Beth Israel Deaconess Medical Center Committee on Clinical Investigations and Institutional Review Board and Massachusetts Institute of Technology Committee on the Use of Humans as Experimental Subjects. Informed consent was waived by both committees.

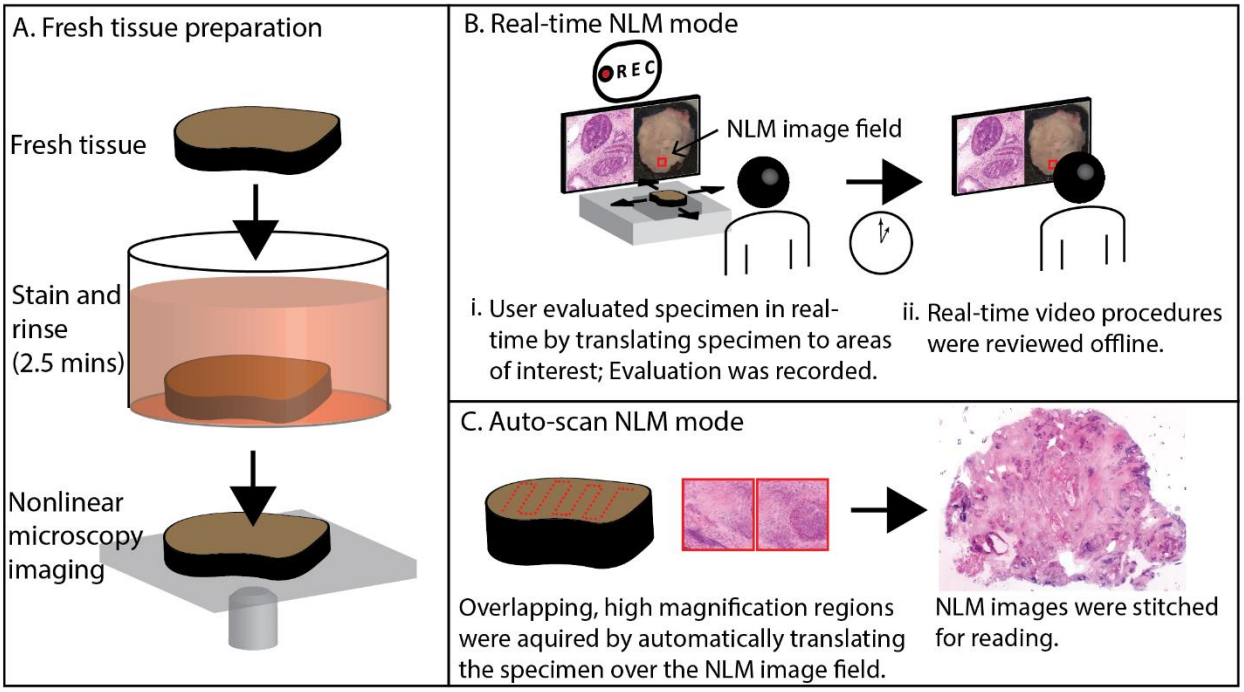

Figure 4.10. Method for evaluating fresh prostate tissue using nonlinear microscopy (NLM). **A.** Fresh tissue was stained in acridine orange and sulforhodamine 101 for 2 minutes, then rinsed in saline for 30 seconds. The specimen was placed on a glass specimen holder and transferred to the nonlinear microscope. The nonlinear microscope was operated in two modes: real-time nonlinear microscopy mode and auto-scan nonlinear microscopy mode. **B.** Real-time nonlinear microscopy mode: A white-light photograph of the specimen surface was displayed with a fiducial marker (in red) indicating the current nonlinear microscopy imaging field, providing a navigational guide. **B(i)** Pathologists examined the specimens on a computer monitor showing nonlinear microscopy images in an H&E color scale at 16 frames/second while translating the specimen to select the nonlinear microscopy field of view. The nonlinear microscopy evaluation procedure was recorded for offline, post-procedural review (**B(ii)**). **C.** Auto-scan nonlinear microscopy mode: a nonlinear microscopy image of the entire specimen cross section was generated by automatically acquiring a series of overlapping, high magnification regions and stitching them together.

The freshly excised prostate tissue was prepared using protocols previously described and shown in **Figure 4.10**A.[7,8] The fresh prostates were grossed following standard protocols then

dissected into specimens of ~10x10 mm with 1-4 mm thickness. The unprocessed specimens were stained in a 50% ethanol solution containing the fluorescent contrast agents acridine orange (40 µg/ml; #10050, Electron Microscopy Sciences) and sulforhodamine 101 (40 µg/ml; S7635, Sigma-Aldrich) for 2 minutes (**Figure 4.10**A). Acridine orange stains DNA similar to hematoxylin, while sulforhodamine 101 stains cytosol and stroma similar to eosin[51]. The specimens were then rinsed for 30 seconds in saline to remove excess dye and placed on a specimen holder with a glass window for imaging with a nonlinear microscope.

The nonlinear microscope[14] used a short-pulsed Ti:Sapphire laser (Chameleon Ultra, Coherent, Inc.) at 1030 nm wavelength to excite acridine orange and sulforhodamine 101 fluorescence in a narrow focus, providing visualization of a thin section without physical sectioning. The microscope had two interchangeable objectives: a 10x, 0.45 numerical aperture (CFI Plan Apo Lambda, Nikon) and a 5x, 0.25 numerical aperture objective (Fluar, Carl Zeiss). Fluorescent light from acridine orange and sulforhodamine 101 was detected using two photomultiplier tubes (H7422-40p, Hamamatsu). A white light camera was integrated into the nonlinear microscope to record a gross view of the specimen.

Specimens were evaluated on the nonlinear microscope in two modes: *real-time nonlinear microscopy mode* which emulates the procedure pathologists use with a standard microscope to evaluate histology and *auto-scan nonlinear microscopy mode* which emulates a digital slide scanner. In real-time nonlinear microscopy mode, shown in **Figure 4.10**B, pathologists examined the specimens on a computer monitor showing nonlinear microscopy images at 16 frames/second while translating the specimen to select the nonlinear microscopy field of view. Images resembling paraffin H&E were generated from nonlinear microscopy by displaying the fluorescence signals from the nuclear (acridine) and stromal (sulforhodamine) detector channels in an H&E color scale

using an algorithm called Virtual Transillumination Microscopy.[6] A fiducial marker (shown in red in **Figure 4.10**B) was displayed on the white-light gross image of the specimen indicating the current position of the nonlinear microscopy image to aid in navigation. The objectives could be rapidly changed for variable magnification and focus depth adjusted for visualizing tissue below the specimen surface. The real-time mode evaluation, including nonlinear microscopy images at known positions, was saved for post-procedural analysis and training. In this mode of operation, a pathologist can rapidly and efficiently evaluate large specimen areas, similar to slide evaluation on a standard histology microscope.

In auto-scan nonlinear microscopy mode (**Figure 4.10**C), a nonlinear microscopy image of the entire specimen was generated by automatically acquiring a series of overlapping, high magnification 1 x 1 mm, 2048 x 2048 pixel frames with 1.2 μm lateral optical resolution[14] and 0.49 μm pixel size. The nonlinear microscopy frames were stitched together (using Microsoft Image Composite Editor) and viewed analogously to a whole slide image from a digital slide scanner. The auto-scan mode is more time-consuming than real-time mode and only acquires a limited number of image depths, however it enables multiple readers to evaluate nonlinear microscopy image data offline.

After evaluation with nonlinear microscopy, the fresh specimens were fixed in formalin on the glass surface of the specimen holder to avoid distortion of the imaged region by specimen handling, then processed for conventional paraffin H&E. The paraffin H&E slides were scanned with a digital slide scanner (20x magnification; Aperio AT2, Leica Biosystems Inc.).

Blinded Reading

Three pathologists (a senior pathologist with over 20 years of experience, a junior pathologist with less than 5 years of experience, and a pathology resident) evaluated nonlinear microscopy images and corresponding paraffin H&E in a prospective blinded reading consisting of training, pretesting, and reading phases. This protocol, outlined in **Figure 4.11**, was used to assess the accuracy of detecting carcinoma on radical prostatectomy specimens using nonlinear microscopy. Intraoperative Gleason scoring of radical prostatectomies is typically not required and thus excluded in our analysis.

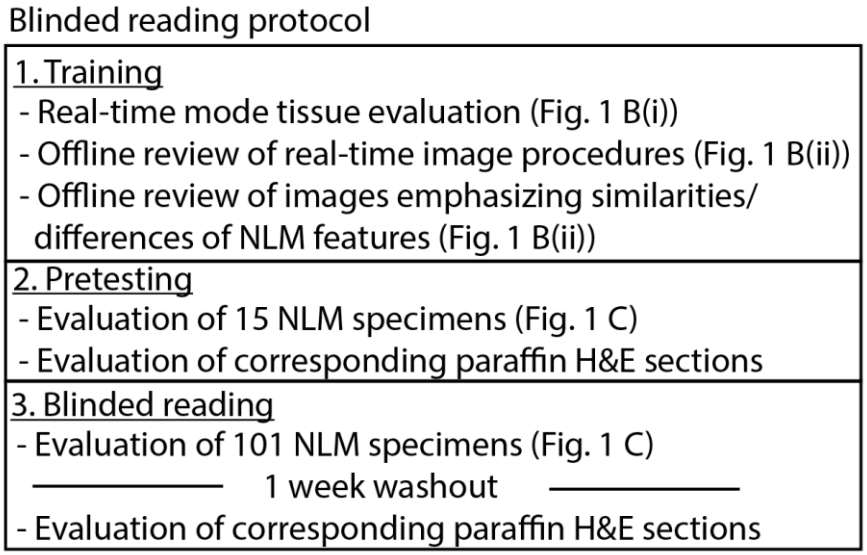

Figure 4.11. Blinded reading protocol of nonlinear microscopy (NLM) images. The three phase protocol consisted of training, pretesting, and blinded reading to assess the sensitivity and specificity of detecting cancer using nonlinear microscopy versus the gold-standard of paraffin H&E.

Training

The pathologists were trained in three steps. In the first step, pathologists evaluated fresh tissue in real-time nonlinear microscopy mode for at least 30 minutes to gain familiarity with nonlinear microscopy imaging and ergonomics. In the second step, pathologists reviewed 8 prerecorded real-time nonlinear microscopy evaluation procedure videos (**Figure 4.10**B(ii)) (each ~5-10 mins in length) from 8 different patients. This step provided experience with various prostate pathologies visualized in fresh tissue on nonlinear microscopy. In the final training step, the pathologists reviewed images from real-time imaging procedures that emphasized the differences and similarities between nonlinear microscopy and paraffin H&E. These differences and similarities were described previously.[7] The nonlinear microscopy training was performed using real-time nonlinear microscopy mode due to the ease and rapidity of capturing large areas of varying pathologies. The training step took approximately 3 hours for each pathologist.

Pretesting and reading

122 freshly excised prostate specimens with an average size of 10 x 10 mm were collected from 40 patients and imaged in auto-scan nonlinear microscopy mode. Corresponding paraffin H&E slides were made and scanned on a slide scanner. The nonlinear microscope was operated in auto-scan nonlinear microscopy mode to enable evaluation of the same specimen area by multiple pathologists and enable high correspondence between the nonlinear microscopy imaging plane and the paraffin H&E slide. The nonlinear microscopy images and scanned paraffin H&E slides were viewed in OpenSeaDragon, a web-based viewer that enables variable magnification review. Nonlinear microscopy data from 6 specimens was discarded due to poor correspondence between the nonlinear microscopy and paraffin H&E image planes or because of poor tissue preservation unrelated to the study. These mismatches between the plane of nonlinear microscopy imaging and

paraffin H&E slide occur because the nonlinear microscopy image is acquired on freshly excised tissue and the paraffin H&E slide requires tissue processing and microtome sectioning.

In pretesting, pathologists read 15 nonlinear microscopy images for the presence or absence of cancer. Corresponding paraffin H&E slides were then read to provide immediate feedback. After training and pretesting, the pathologists read nonlinear microscopy images of the remaining 101 specimens in a randomized order, blinded to paraffin H&E results, and recorded whether cancer was present or absent. After a washout period of one week, the pathologists read the paraffin H&E slides. A consensus diagnosis was obtained for paraffin H&E readings in the event of reader discrepancy in order to have a gold-standard diagnosis for comparison.

Statistical Analysis

The sensitivity, specificity, positive predictive value, negative predictive value, and accuracy of nonlinear microscopy assessment for the presence of cancer was calculated for each nonlinear microscopy reader using the consensus paraffin H&E diagnosis as the gold-standard. The 95% confidence intervals were calculated on the pooled results from the 3 readers. The interobserver variability was calculated using Fleiss kappa. A two-sample t test was used to compare the mean time required to evaluate the nonlinear microscopy images and paraffin H&E.

4.3.3. RESULTS

Nonlinear Microscopy Images of Fresh Prostate Specimens

Example nonlinear microscopy images of fresh prostate specimens are shown in **Figure 4.12** and **Figure 4.13**. In these figures, differences between nonlinear microscopy images of fresh specimens and paraffin H&E including cytoplasmic color difference, increased eosinophilic secretions in carcinoma, diminishment of cell border clarity, expanded cellular appearance, and

images that appear thicker than paraffin H&E, are apparent, but these differences do not impair interpretation.[7] Prostate carcinoma with poorly formed and fused glands (Gleason 4) is shown in

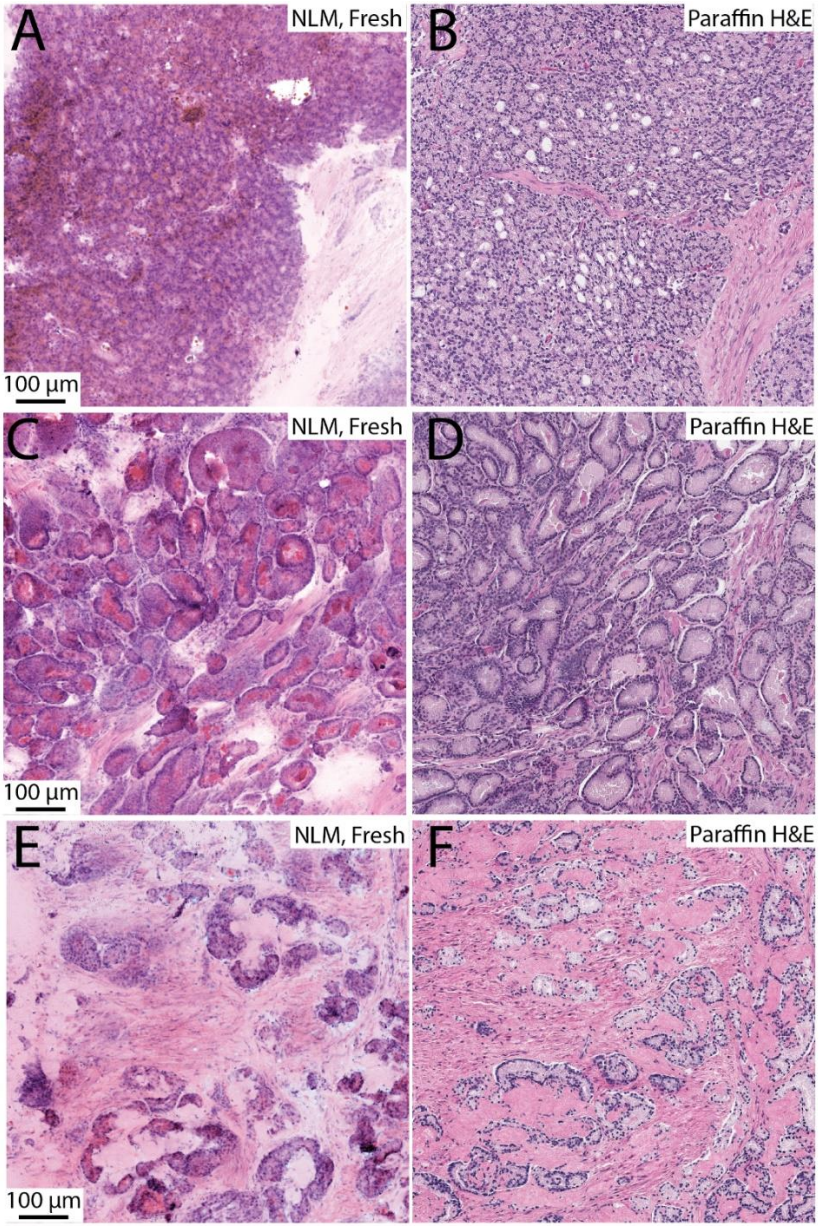

Figure 4.12. Example nonlinear microscopy (NLM) images of fresh tissue pathology and corresponding paraffin H&E slides. A, B. Poorly formed and fused glands (Gleason 4); **C, D**. Foamy gland adenocarcinoma; **E, F.** Mucinous fibroplasia.

Figure 4.12A (nonlinear microscopy) and B (paraffin H&E). **Figure 4.12**C and D show an example of foamy gland adenocarcinoma visualized with nonlinear microscopy and paraffin H&E, respectively. The foamy appearance is not as apparent in the nonlinear microscopy image and instead the cytoplasm appears more eosinophilic. The bright intraluminal eosinophilic secretions seen in the nonlinear microscopy image commonly appear in fresh tissue visualization of carcinoma and is particularly evident in foamy gland variant. An example of mucinous fibroplasia visualized with nonlinear microscopy and paraffin H&E is shown in **Figure 4.12**E and F. Collagenous micronodules are seen with associated eosinophilic stroma. **Figure 4.13**A and B show glomeruloid and cribriform patterns, respectively. **Figure 4.13**C is an example of perineural invasion. **Figure 4.13**D shows prominent nucleoli in a malignant gland, exemplifying the cytological detail present in nonlinear microscopy images of fresh tissue. In these example images, typical histological features of carcinoma (prominent nucleoli, glandular and stromal architectural patterns) are readily apparent in nonlinear microscopy and enable specimen reading and interpretation.

Sensitivity and Specificity

Table 4.3 summarizes the blinded reading results of the 101 specimens (61 with cancer present on paraffin H&E, 40 without cancer present). All three pathologists had a 95% or greater sensitivity and a 100% specificity. The pooled sensitivity was 97.3% (93.7%-99.1%; 95% confidence interval) and specificity was 100.0% (97%-100%). Interobserver agreement between the three pathologists was almost perfect for the nonlinear microscopy readings with a Fleiss κ=0.95. The three individual pathologists required an average of 39.2, 53.5, and 73.7 seconds to evaluate each nonlinear microscopy image and 38.6, 57.0, and 59.4 seconds to evaluate each paraffin H&E slide giving a combined average time of 55.4 seconds per nonlinear microscopy

image and 51.7 seconds per paraffin H&E slide. These mean times were not statistically different in a two-sample t test (p=0.76).

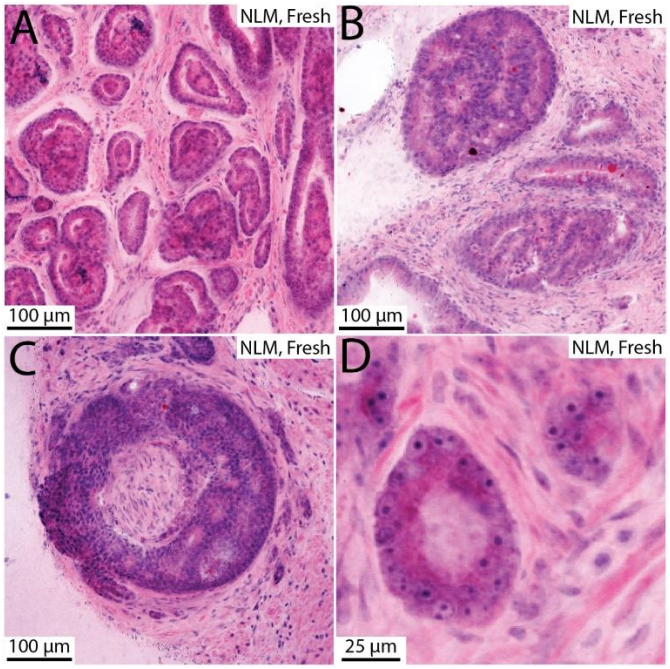

Figure 4.13. Example nonlinear microscopy (NLM) images of carcinoma in fresh prostate tissue. A. Glomeruloid pattern. **B.** Cribriforming. **C.** Perineural invasion. **D.** Large nucleoli visualized in malignant glands.

Reader	Sensitivity [95% CI]	Specificity [95% CI]	PPV	NPV	Accuracy
Reader 1	0.951	1.000	1.000	0.930	0.970
Reader 2	1.000	1.000	1.000	1.000	1.000
Reader 3	0.967	1.000	1.000	0.952	0.980
Pooled 1-3	0.973 [0.937, 0.991]	1.000 [0.970, 1.000]	1.000	0.960	0.983

Table 4.3. Sensitivity and specificity of nonlinear microscopy for detecting carcinoma in fresh prostate tissue vs paraffin H&E.

4.3.4. DISCUSSION

In this study, we show that nonlinear microscopy with rapid fluorescent staining enables cancer detection with nearly equivalent accuracy (98%) to that of paraffin H&E with only a short training period. Specimen preparation requires <3 minutes after grossing, is non-destructive (no freezing or microtome sectioning), and enables gold-standard histological post-operative analysis of the same specimen. In this blinded reading, small fragments of tissue (10 x 10 mm) were used to represent localized detection of prostate cancer, however, multi-centimeter, fresh whole-mount specimens can also be evaluated on the nonlinear microscope without increasing specimen preparation times. Furthermore, several specimens can be prepared in parallel without additional specialized equipment because staining only requires a container for the fluorescent solution.

Because the nonlinear microscope can operate in real-time and auto-scan modes, it combines the analogous capabilities of traditional light microscopy and whole slide scanning in a single instrument. In both of these modes, the time to scan an area increases as the image resolution increases. In this study, we acquired data using auto-scan mode, which restricts imaging to a single objective for the entire specimen. Using this mode, we found that acquiring data using a 10x, 0.45 numerical aperture objective was sufficient for cancer detection in large specimens, while maintaining rapid data acquisition times. Real-time mode enables rapid surveying of large areas of tissue at user-specified magnifications and is thus the proposed mode for intraoperative evaluation of fresh tissue. Real-time mode was also used for pathologist training since the trainees could directly operate the microscope and observe a multitude of different specimens efficiently. This mode of operation, however, does not provide unbiased images of specimens because the operator controls the specimen translation, speed, and magnification, and therefore it is not appropriate for a blinded reading. Although the auto-scan mode is slower to acquire data, it enables

evaluation of the same specimen by multiple different pathologists unbiased to the other's evaluation. Because it also enables specimen image archiving for offline viewing, the auto-scan mode was naturally conducive to this reading study.

There are several differences observed when evaluating fresh, unprocessed tissue with nonlinear microscopy. These differences include: variations in cytoplasmic color which is typically more basophilic in carcinoma on nonlinear microscopy than paraffin H&E; an increased frequency and volume of eosinophilic intraluminal secretions in carcinoma when visualized in fresh tissue with nonlinear microscopy than on processed tissue with paraffin H&E; loss of cell border sharpness and a thicker appearance of nonlinear microscopy images on fresh tissue due to the tissue not being dehydrated or processed with paraffin. These differences, however, are consistent and, combined with the ability to rapidly image multiple depths (analogous to serial sections), can augment interpretation of fresh tissue. Therefore, with training and experience, pathologists became accurate and comfortable interpreting these differences as evidenced by the high sensitivity and specificity (97.3% and 100%, respectively) and inter-observer agreement reported in this study.

Blinded reading of surgical margins with nonlinear microscopy was not practical in this study because positive margin rates are low and large numbers of specimens representing surgical margins were not available. However, we have previously demonstrated nonlinear microscopy imaging of extra-prostatic extension and positive surgical margins[7] and typical histological features of carcinoma (prominent nucleoli, glandular and stromal architectural patterns) are independent of its location and were readily apparent in nonlinear microscopy images. Furthermore, this study used small fragments of tissue (average 10 x 10 mm) to assess localized cancer detection. Finally, diagnostic performance is expected to further improve when nonlinear

microscopy is operated in real-time mode because the pathologist can adjust the instrument and view different depths continuously, while data from auto-scan nonlinear microscopy mode is limited to a few depth planes. This study provides evidence that nonlinear microscopy has a high diagnostic performance for assessing prostate cancer and may be a promising method for intraoperative specimen evaluation.

Gleason scoring would typically not be performed intraoperatively and therefore is not included in this study. Instead, we plan to analyze Gleason scoring accuracy in a separate study on needle core biopsies where it might be used clinically. Our initial studies, which include use of higher magnification objectives with smaller fields of view, suggest that Gleason scoring is feasible but requires increased reading time. There are challenges when interpreting Gleason patterns due to the differences in nonlinear microscopy image for fresh tissue versus paraffin H&E as described above, including thicker appearing sections, increased luminal secretions, and variation in simulated staining colors. However, nonlinear microscopy can generate images at adjustable depths up to 100 μm below the tissue surface, analogous to serial sectioning, which may enhance interpretation of Gleason patterns.

Many studies have investigated the utility of frozen sections in intraoperative evaluation of prostate margins.[90,92,93] In order to avoid excessively prolonging surgical time, these studies have often restricted frozen sections to a small number of specimens representing a limited fraction of the margin or grossly suspicious areas and have reported wide variations in sensitivity for detecting positive margins.[90,92–94] Recent studies using more comprehensive frozen section sampling of prostatectomy specimens demonstrated high sensitivities for detecting positive surgical margins, enabling an increase in the rate of nerve-sparing radical prostatectomies and a reduction in positive surgical margins.[76,77,91,95] For example, in a study of over 11,000 patients, NeuroSAFE[76]

demonstrated a significant increase in nerve-sparing radical prostatectomy rates in (81% to 97% in all tumor stages) with a decrease in positive margins rates when using frozen sections. However, NeuroSAFE required processing up to 25 frozen sections per patient, with 5 cryostats, 2 pathologists, and 4 technicians to maintain a 35-minute average evaluation time. This and other studies demonstrated that intraoperative margin evaluation can improve nerve-sparing radical prostatectomy and positive surgical margin rates, but comprehensive sampling required extensive personnel, which is impractical and expensive for most hospitals and surgical workflows.[76–78]

The present study suggests that nonlinear microscopy has sufficient accuracy for rapid evaluation of prostate tissue, achieving a pooled 97.3% sensitivity and 100% specificity for detecting carcinoma compared to paraffin H&E in a blinded reading by three pathologists. In contrast to frozen section analysis, nonlinear microscopy imaging does not require freezing and microtome sectioning. Multiple specimens can be prepared for imaging in parallel and large specimens can be imaged without requiring dissection into smaller sizes. Pathologists can begin nonlinear microscopy assessment within 3 minutes after inking and grossing. These advances can support future studies investigating comprehensive nonlinear microscopy evaluation of radical prostatectomy margins, comparable to the NeuroSAFE, with many fewer personnel and shorter evaluation times. Accurate, safe, and efficient intraoperative margin assessment could improve decisions regarding nerve-sparing without increasing positive margin rates.

4.3.5. SUPPLEMENTARY RESULTS

Integrity of RNA and DNA after NLM preparation

This work was done in collaboration with Jared T. Ahrendsen, Olga Voznesensky, and Steven Balk at Beth Israel Deaconess Medical Center.

Freshly excised prostate tissue was collected and divided into three samples. Sample 1 and Sample 2 were stained in a solution of acridine orange and sulforhodamine 101 according to the standard NLM imaging protocol described previously. Sample 3 was a control and was not stained. All three samples were snap frozen to preserve tissue integrity and stored at -80°C overnight.

RNA and DNA were extracted from the three samples. The samples were analyzed on a TapeStation (Agilent). Sample 1 had an RNA integrity number (RIN) of 3.9, Sample 2 had a RIN of 4.6, and Sample 3 had a RIN of 5.8. All RIN values in these samples are within an acceptable range for additional analysis. Variation in RIN values are expected in human samples. The DNA was not found to be degraded in any of the samples.

Sample #	Sample treatment	GAPDH C_T Mean	18S C_T Mean
RNA			
1	Stained	21.57	8.91
2	Stained	21.76	7.80
3	Control	20.49	8.45
DNA			
1	Stained	30.50	17.55
2	Stained	31.25	18.23
3	Control	29.29	16.27

Table 4.4. Results from reverse transcription polymerase chain reaction (RT-PCR) on prostate tissue samples that were stained with acridine orange and sulforhodamine 101. GAPDH and 18S had similar cycle thresholds (C_T) in all samples indicating that amplification was similar between samples prepared for NLM imaging and control samples.

Portions of the three samples were amplified with reverse transcription polymerase chain reaction (RT-PCR) to investigate the effects of NLM evaluation. Amplification of GAPDH and 18S were analyzed in each sample. The results are shown in **Table 4.4**.

GAPDH and 18S were amplified in the stained and unstained samples in both RNA and DNA. C_T values (cycle threshold that amplification occurred) were similar between the stained and unstained samples. In conclusion, NLM tissue preparation did not alter RNA or DNA analysis indicating that RNA and DNA are likely viable for other downstream analyses. Additional studies on specific applications are needed to confirm these conclusions.

Chapter 5
NLM evaluation of prostate biopsies

5.1. INTRODUCTION

Over 1 million prostate biopsy procedures are performed annually in the US.[96] Prostate biopsies are evaluated using formalin-fixed paraffin embedded (FFPE) histology, which requires specimen processing that can take hours. Patients and urologists would benefit from a faster diagnosis which would reduce anxiety and expedite care.[97–99] Pathologists must also triage biopsy tissue for FFPE histology, molecular/genomic analyses, and research prior to knowing histologic tissue features. This lack of information can lead to suboptimal tissue allocation.[100] For example, inadequate biological specimens due to, among other things, inadequate size and cellular composition, has been identified as one of the most significant challenges in developing and validating biomarkers from tumor banks.[101] Furthermore, the number of biopsies that a clinician performs may be reduced with immediate information on biopsy content.[102,103]

Frozen sections are not used for rapid diagnosis of prostate biopsies because they are time- and labor-intensive, consume the small amount of tissue available, and the freezing and microtome sectioning introduce artifacts, distorting the histology and complicating interpretation.[104] Imprint cytology can be used on fresh tissue and is much faster than frozen sections, however, only a small fraction of cells are analyzed in limited contexts and the preparation process can distort the tissue and alter cellularity.[105–107] Techniques that image fresh biopsy specimens without requiring fixation, freezing, microtome sectioning, or distorting tissue could reduce the time required for diagnosis while preserving biopsy integrity.

Nonlinear microscopy (NLM) is a fluorescence microscopy technique that can produce high-resolution images of freshly excised tissue that resemble H&E histology. NLM scans a short-pulsed laser over a specimen to excite fluorescence only at the laser focus, generating images without microtome sectioning.[4] NLM enables imaging continuously up to ~100 μm below the tissue surface, providing three-dimensional visualization of the tissue analogous to serial sectioning without microtome sectioning.[8,37] In a previous three-pathologist blinded reading study of 122 prostatectomy specimens from 40 patients, NLM achieved a 97.3% sensitivity and 100.0% specificity for detecting prostate cancer compared to FFPE histology.[88]

In Section 5.2. , we describe a method for evaluating prostate core needle biopsies in minutes using NLM and evaluate this method on 170 biopsies from 63 patients who underwent targeted in-bore MRI or MRI/ultrasound fusion directed core needle biopsy procedures. The aim of this study was to assess the accuracy and timing of using NLM for diagnosing prostate carcinoma, Gleason scoring, and estimating the amount of core involved by carcinoma on needle biopsies. In Section 5.3. , we investigate the similarities and differences of NLM versus FFPE H&E of prostate needle core biopsies from the pathologist's perspective on the 170 biopsies. NLM images of benign tissue and carcinoma (including Gleason patterns) are described along with the challenges associated with this new technique.

This work was done in collaboration with Tadayuki Yoshitake and James G. Fujimoto at Massachusetts Institute of Technology and Yue Sun, Yubo Wu, Linda York, Boris Gershman, Leo L. Tsai, and Seymour Rosen at Beth Israel Deaconess Medical Center and Harvard Medical School. This study was supported in part by the National Institutes of Health R01-CA178636-06, R01 CA249151-01, and the MIT Termeer Medical Engineering Graduate Fellowship.

5.2. NLM ACCURACY FOR EVALUATING PROSTATE BIOPSIES

5.2.1. INTRODUCTION

In this section, we describe a method for evaluating prostate core needle biopsies in minutes. Our goal was to assess the accuracy of NLM in diagnosing prostate carcinoma, Gleason scoring, and determining the core fraction involved by carcinoma.

5.2.2. MATERIAL AND METHODS

A detailed description of the Material and Methods can be found in Section 5.2.4. One hundred and seventy biopsies from 63 patients who underwent MRI-guided targeted prostate biopsies were collected for NLM imaging. MRI-guided biopsies were performed using MRI-ultrasound (US) fusion biopsy in the office, where previously-acquired MRI images were mapped onto real-time US images, or in-gantry biopsy, where all targeting and sampling were performed at the MRI scanner. The biopsies were stained with acridine orange and sulforhodamine 101 for 45 seconds to provide nuclear and stromal/cytoplasmic contrast analogous to H&E. After staining, the biopsies were evaluated by a genitourinary pathologist in real time using an NLM instrument. The pathologist translated the specimen both laterally and vertically enabling imaging in three dimensions while NLM images were displayed on a computer monitor in an H&E color scale. After NLM evaluation, the biopsies were processed for FFPE histology according to standard practice.

The biopsies from the first 10 patients (15 biopsies) were used to optimize protocols. The biopsies from the remaining 53 patients (155 biopsies) were read by one of two pathologists who assigned a diagnosis of cancer or benign, a Gleason score, and a percent of core involved by carcinoma in real time. The same or different pathologist evaluated the FFPE histology blinded to

the NLM. The results from the NLM real-time evaluation and the FFPE histology evaluation were compared.

5.2.3. RESULTS AND DISCUSSION

Figure 5.1 shows example NLM and corresponding FFPE H&E images of benign hyperplasia and carcinoma. Individual malignant glands, fused glands, and sheet-like architecture of Gleason 3, 4, and 5 respectively are clearly visualized with NLM. Differences between NLM and FFPE H&E include reduced cell-border sharpness, variations in cytoplasmic color, and larger, more prominent nucleoli.

	Biopsies (Total = 155)	Lesions (Total = 62)	Patients (Total = 53)
Sensitivity [95% CI]	0.924 [0.850,0.969]	0.923 [0.791, 0.984]	0.917 [0.775, 0.983]
Specificity [95% CI]	1.000 [0.943, 1.000]	1.000 [0.852, 1.000]	1.000 [0.805, 1.000]
PPV	1.000	1.000	1.000
NPV	0.900	0.885	0.850
Accuracy	0.955	0.952	0.943

Table 5.1. Summary of sensitivity and specificity of prostate biopsies evaluated using nonlinear microscopy (NLM). Positive predictive value (PPV), negative predictive value (NPV), confidence interval (CI).

Eighty-five (from 39 lesions, 36 patients) out of the 155 biopsies had carcinoma on FFPE histology. The sensitivities on a per biopsy, per lesion, and per patient basis were 92.4%, 92.3%, and 91.7% respectively and specificities were 100% (**Table 5.1**). Seven biopsies with carcinoma on FFPE H&E were falsely diagnosed as benign on NLM. Two of these biopsies had less than 5% of the core involved by carcinoma on FFPE H&E and likely resulted from a mismatch in NLM imaging plane and FFPE H&E sectioning plane. The other five biopsies had a low grade carcinoma

(Gleason pattern 6) on FFPE H&E and an appearance that had not previously been seen on NLM (small atrophic and malignant glands). Upon review of the NLM data after FFPE H&E analysis, the carcinoma was apparent. Future studies will need to incorporate focused training with more variations of low grade carcinoma to reduce interpretation errors.

The agreement between the Grade Group determined by NLM and FFPE H&E on a per biopsy basis had an unweighted Cohen's Kappa of 0.588 (**Table 5.2**). Gleason scoring typically has high interobserver variability with average Kappa values ranging from 0.41 to 0.59.[108] Gleason patterns also change throughout the depth of individual biopsies.[109] Therefore, variations in NLM imaging and FFPE H&E sectioning plane can alter Gleason scores. Furthermore, NLM can image continuous variations in depth in real time, which enables volumetric assessment and can make Gleason score comparisons to a two-dimensional section challenging. The Gleason score could not be determined in three biopsies on NLM and two on FFPE H&E because only a small focus of carcinoma was present in the biopsy.

The mean time to prepare biopsies was 2.45 minutes, the mean NLM evaluation time per biopsy was 2.10 minutes, and the mean total time (preparation + evaluation time) per patient was 8.15 minutes. The mean evaluation time per biopsy in Patients 11-30 (first 20 patients after the 10-patient optimization period) was double the evaluation time in the remaining patients. The number of biopsies evaluated for a single patient varied from 1 to 9 with a median of 3 biopsies. These times include diagnosing, Gleason scoring, and determining the percent of biopsy involved with carcinoma. Evaluating biopsies for the presence or absence of carcinoma alone using NLM could be prioritized in many applications without incurring additional delays associated with Gleason scoring.

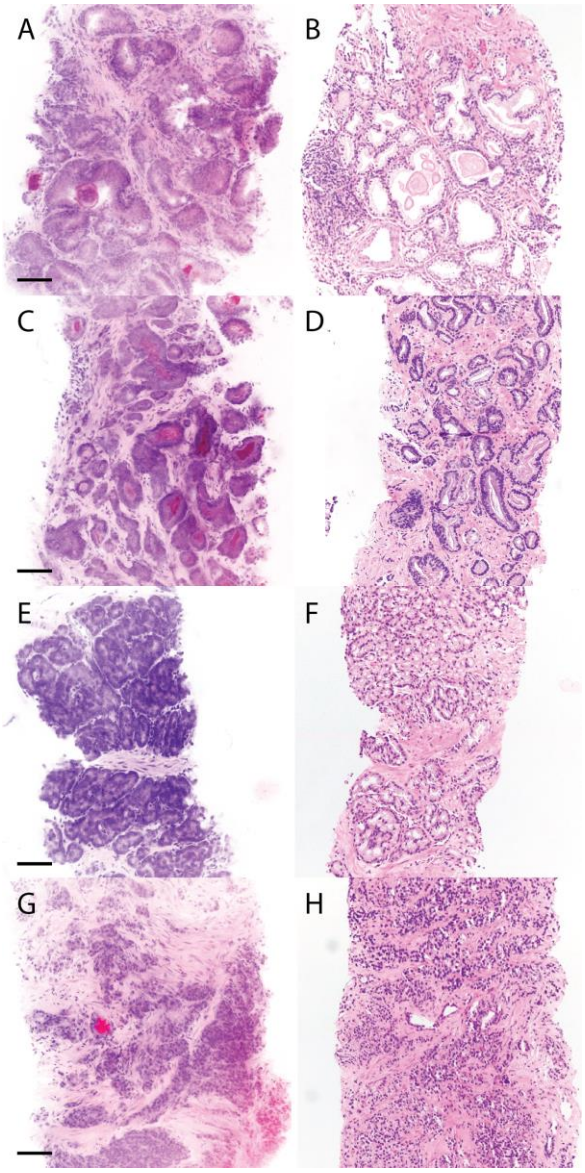

Figure 5.1. Examples of nonlinear microscopy (NLM) images of prostate core needle biopsies. **A.** NLM and **B.** corresponding FFPE H&E images of benign prostatic hyperplasia. Large glands with abundant cytoplasm and papillary infolding. Corpora amylacea are seen in lumens. **C.** NLM and **D.** corresponding FFPE H&E images of a biopsy with Gleason pattern 3. Individual glands with amphophilic cytoplasm and bright, eosinophilic secretions in lumens are seen throughout the biopsy. **E.** NLM and **F.** corresponding FFPE H&E images of a biopsy with Gleason pattern 4. Poorly formed and fused glands are seen in both NLM and FFPE images. **G.** NLM and **H.** corresponding FFPE H&E of a biopsy with Gleason pattern 5. Solid, sheet-like architecture of malignant cells are infiltrating prostatic stroma. (Scale bar = 100 μm).

		NLM				
	Grade Group	**1**	**2**	**3**	**4**	**5**
FFPE H&E	**1**	24	6	0	0	0
	2	1	22	9	0	0
	3	0	2	7	0	0
	4	0	0	1	3	0
	5	0	1	2	1	1

Table 5.2. Comparison of Grade Groups determined using nonlinear microscopy (NLM) and formalin-fixed, paraffin-embedded (FFPE) H&E slides.

The present study has several limitations. All biopsies were MRI guided and are therefore from a distinct group of radiologically suspicious lesions (PI-RADS scores of at least 3). There was also a limited number of patients with biopsies scored in Grade Group 5. Future studies are needed to measure accuracy of this Grade Group. Additionally, this study was performed using an NLM instrument that is currently being developed for wide clinical use.

This section presents the first analysis of NLM for the real-time evaluation of diagnostic prostate core needle biopsies. Multiple biopsies could be prepared in parallel and NLM evaluation began within an average of 2.45 minutes. Pathologists achieved a 92.4% sensitivity and 100.0% specificity for detecting carcinoma, on a per biopsy basis, compared to FFPE histology. NLM is a promising method for rapid prostate biopsy evaluation; however, future studies that analyze biopsies in an intraprocedural setting are needed.

5.2.4. SUPPLEMENTARY INFORMATION

5.2.4.1. SUPPLEMENTARY MATERIAL AND METHODS

All prostate lesions were initially assessed with diagnostic MRI using the PI-RADS 2.1 scoring system.[110] The need for biopsy was determined by the managing urologist, based on MRI

findings and other clinical measures such as PSA levels. All samples were obtained from targeted lesions using 18-gauge core biopsy devices. For MRI-US fusion biopsies, only targeted cores were included in this study. All research was performed according to protocols approved by Beth Israel Deaconess Medical Center Committee on Clinical Investigations and Institutional Review Board and Massachusetts Institute of Technology Committee on the Use of Humans as Experimental Subjects. Written informed consent was obtained from all subjects.

Biopsy preparation

Biopsies were placed in separate jars of formalin immediately after removal from the biopsy needle according to standard clinical practice (**Figure 5.2**). In the first 22 patients, biopsies were collected and evaluated with NLM almost immediately after the biopsy procedure. Due to COVID-19 physical distancing restrictions, subsequent patient biopsies were collected 1-3 hours after the biopsy procedure. The additional time in formalin did not noticeably alter NLM images. The biopsies were removed from the formalin jars and stained with acridine orange (40 µg/ml; #10050, Electron Microscopy Sciences, Hatfield, PA) and sulforhodamine 101 (40 µg/ml; S7635, Sigma-Aldrich, St. Louis, MO) in a 1:1 ethanol:water solution for 45 seconds and rinsed for 1-2 seconds in saline. This staining procedure is similar to that previously described for prostatectomy specimens.[7,88] Due to the much smaller volume of tissue in biopsies, optimal staining was achieved in 45 seconds rather than the 2 minutes required for prostatectomy specimens. Multiple biopsies from the same patient were stained in parallel to minimize preparation time.

After staining, the biopsies were placed on a specimen holder with glass windows, enabling evaluation of several biopsies on a single surface. Biopsy foam was used to apply gentle compression against the glass to ensure a flat imaging surface without distorting architecture. The

biopsy foam was soaked in formalin to hydrate the biopsy and continue fixation during NLM evaluation. The specimen holder was placed in the NLM instrument.

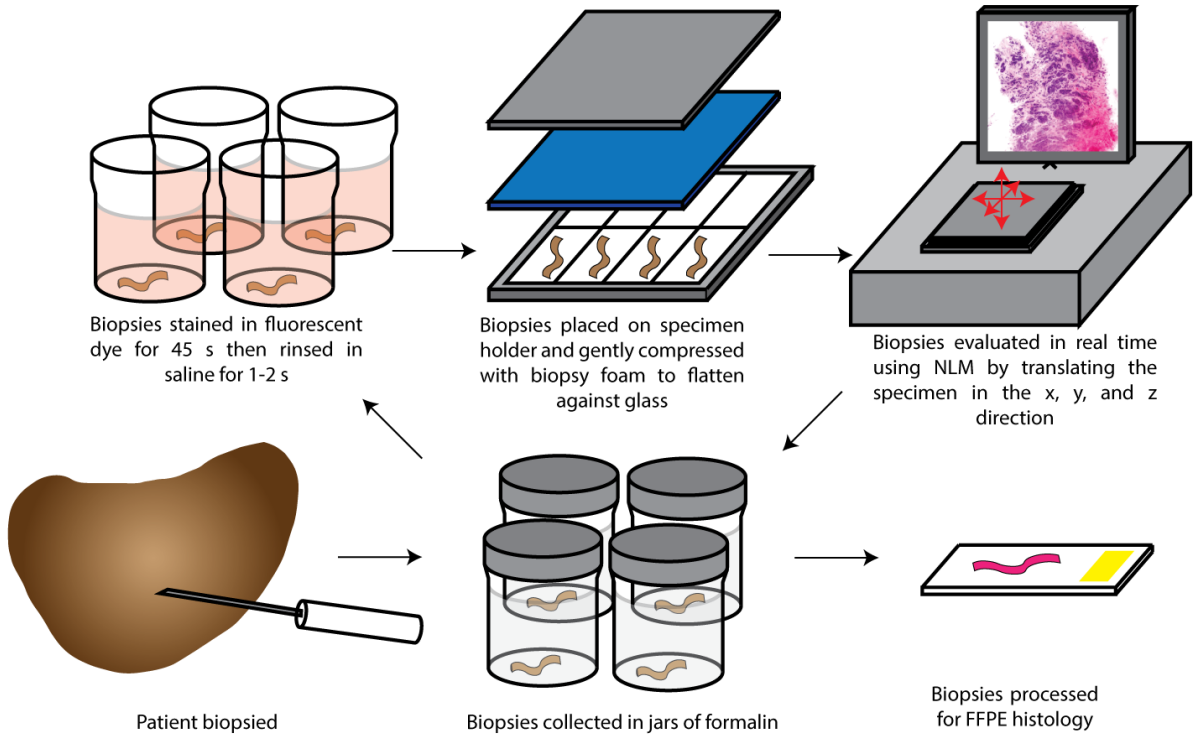

Figure 5.2. Method for preparing and evaluating prostate biopsies using nonlinear microscopy (NLM). During the biopsy procedure, the biopsies were transferred from the biopsy needle (18 gauge) to labelled jars of formalin (the standard of care). Multiple biopsies were then stained in parallel in acridine orange and sulforhodamine 101 for 45s and rinsed to remove excess dye. The biopsies were placed on a specimen holder with a glass window, gently compressed with biopsy foam to ensure a flat imaging surface, covered with a lid, and placed in the NLM instrument. A pathologist evaluated the biopsies in real time by laterally (x-y plane) translating the specimens to areas of interest and changing the imaging depth (z axis). A computer monitor displayed the NLM images at 16 frames/second in an H&E color scale. After NLM evaluation, the biopsies were returned to their formalin jars and submitted for standard FFPE histology.

NLM evaluation

The custom designed NLM instrument (previously described[14]) used a Ti:Sapphire laser (Chameleon Ultra, Coherent, Inc.) operated at 1030 nm to excite the fluorescent dye in a narrow focal depth without microtome sectioning. A 20x, 0.75 NA air objective (CFI Plan Apo Lambda 20x, Nikon, Melville, NY) was used. The fluorescent signals from the acridine orange and sulforhodamine 101 were separated using a 590 nm high-pass dichroic beam splitter, filtered using two emission filters (ET540/40 m, Chroma Technology, Bellows Falls, VT and FF01–650/60, Semrock, Rochester, NY), and detected using two photomultiplier tubes (H7422-40p, Hamamatsu, Hamamatsu City, Japan).

The biopsies were evaluated by a genitourinary pathologist in real time by translating the specimen holder while NLM images of 1024x1024 pixels were displayed on a computer monitor at 16 frames/second in an H&E color scale.[6] This evaluation mode is analogous to viewing biopsies using a standard histology microscope and is advantageous as it enables rapid surveying of tissue at low magnification with more careful inspection at high magnification if needed. The pathologist translated the specimen both in the x-y plane and z axis (up to 100 μm below the specimen surface), enabling imaging in three dimensions. This capability is analogous to serial sectioning, but does not require physical microtome sectioning. The H&E color scale could be adjusted to suit the user's staining and visualization preference. The NLM images were recorded along with their x, y, and z positions for post-procedural reconstruction and analysis. After NLM evaluation, the biopsies were returned to their original formalin jars and processed for FFPE histology according to standard practice.

The first 15 biopsies (10 patients) were used to optimize tissue preparation and imaging and to gain experience interpreting small core needle biopsies. Previous studies interpreting cancer on

multicentimeter prostatectomy specimens served as a foundation for this optimization and initial evaluation.[7,88] A genitourinary pathologist (SR or YS) reviewed these biopsies with NLM in real time. The same pathologist later evaluated the FFPE histology when it was available (1 to 2 days after the NLM evaluation). Following standard of care, three FFPE H&E slides at three different levels were evaluated per biopsy. Additional levels and special stains were evaluated as needed. After preparing and submitting the biopsy report for clinical care, areas of interest in the NLM and FFPE histology were compared side-by-side. This initial optimization phase improved understanding of NLM capabilities in biopsies, diagnoses, and Gleason scoring.

The remaining 155 biopsies (53 patients) were read by one of two pathologists who assigned a diagnosis of cancer or benign, a Gleason score, and a percent of core involved by carcinoma in real time.

Analysis of accuracy of detecting carcinoma and Gleason scoring

Sensitivities, specificities, positive predictive values (PPV), and negative predictive values (NPV) and 95% confidence intervals were calculated using FFPE histology as the gold standard on a per biopsy, per lesion, and per patient basis. Biopsies were classified into a Grade Group 1-5 based on the Gleason score. Unweighted Cohen's Kappa was calculated between the Grade Groups assigned by NLM and FFPE histology. The correlation and absolute difference between the percent of core involved by carcinoma determined by NLM and by FFPE histology was calculated.

5.2.4.2. SUPPLEMENTARY RESULTS

Biopsy evaluation

Although the accuracy of prostate biopsy evaluation is high, there are several differences between NLM and FFPE H&E. Many of these differences can be attributed to the fact that NLM

images freshly biopsied tissue. NLM images can have reduced cell-border sharpness due to the tissue not being dehydrated or processed for FFPE histology. Gleason pattern 3 glands, although individual and distinct, are often filled with eosinophilic contents visualized on NLM that are removed by tissue processing for FFPE histology. Variations in cytoplasmic color appears throughout cells and distinct pink fibers (that appear to be elastic fibers) can be seen throughout the stroma and in the elastic lamina of vessels. Larger and more frequent prominent nucleoli are seen throughout carcinoma in NLM compared to FFPE H&E, which is a reliable diagnostic feature. Systematically characterizing these differences should enable more accurate interpretation of NLM images.

NLM enabled subsurface visualization of biopsies in real time. This was especially important for examining core needle biopsies since the surfaces of the biopsies usually have obscuring artifacts due to damage from the biopsy needle or handling the fragile tissue. It is important to note that these artifacts are not present on FFPE histology since slides are obtained from subsurface tissue after facing the paraffin block.

Percent of core involved with carcinoma

The estimated percent of the core involved with carcinoma determined using NLM versus FFPE histology had a Pearson's correlation coefficient of 0.617. The mean absolute difference between the percent of core involved with carcinoma determined with NLM versus FFPE histology was 17.5%. The Gleason score and percent of the core involved with carcinoma are known to have intra- and inter-observer variability which could contribute to the variations observed here. In addition, variations in NLM evaluation and FFPE H&E sectioning plane could contribute to the differences. Furthermore, NLM enables imaging in three dimensions, which can alter interpretation of the Gleason score and percent of core with carcinoma.

Gleason scoring discrepancies

A major discrepancy in Grade Groups occurred in one biopsy where a Grade Group 2 was scored on NLM versus Grade group 5 on FFPE H&E. This patient had three biopsies of the same lesion. On NLM, the highest Grade Group in these three biopsies was Grade Group 5. Upon review of the NLM data of the discrepant biopsy, Gleason pattern 5 (single cells with large nucleoli infiltrating the prostatic stroma) was apparent among cribriform glands (Gleason 4) and missed during initial real time NLM review. In future biopsy readings, careful analyses of stroma between high grade glands will be important to ensure that cases like this are not scored artificially low.

Duration of prostate biopsy evaluation

Biopsies could be prepared and evaluated rapidly using NLM (**Table 5.3**). The biopsy evaluation time became faster with increased NLM experience. The mean evaluation time per biopsy in the Patients 11-30 (the first 20 patients after the optimization phase) was 3.08 minutes but decreased to only 1.54 minutes in subsequent patients (patients 31-63).

Other techniques

Other groups have also demonstrated rapid evaluation of prostate biopsies using fluorescent microscopy techniques such as confocal fluorescence microscopy[111,112], structured illumination[9], and light sheet microscopy[12]. These studies primarily restrict their analyses to the accuracy of detecting carcinoma and not accuracies of Gleason scoring. NLM uses long wavelength light and nonlinear fluorescence excitation, which enables high contrast, deep imaging in biopsy tissue. It is important to note that none of these techniques, including NLM, are used in current clinical practice, and additional studies are needed for validation.

	Mean	Median	Standard deviation
Preparation time/patient (mins)	**2.45**	**2.19**	**0.78**
Patient #1 to 20	*2.49*	*2.50*	*0.72*
Patient #21 to 53	*2.43*	*2.08*	*0.82*
Evaluation time/biopsy (mins)	**2.10**	**1.68**	**1.42**
Patient #1 to 20	*3.08*	*2.58*	*1.81*
Patient #21 to 53	*1.54*	*1.36*	*0.70*
Total time/patient (mins)	**8.15**	**6.89**	**4.16**
Patient #1 to 20	*8.85*	*8.00*	*4.75*
Patient #21 to 53	*7.75*	*6.83*	*3.81*

Table 5.3. Evaluation time of prostate biopsies using nonlinear microscopy (NLM). The number of biopsies evaluated for a single patient varied from 1 to 9 with a median of 3 biopsies.

5.3. HISTOLOGICAL INTERPRETATION OF PROSTATE BIOPSIES USING NLM

5.3.1. INTRODUCTION

In Section 5.2. , we reported a study investigating the accuracy of NLM for prostate biopsy evaluation. A total of 170 biopsies from 63 patients who underwent targeted in-bore MRI or MRI-ultrasound fusion biopsy were prospectively collected and evaluated in real time by genitourinary pathologists using NLM. Pathologists achieved a 92.4% sensitivity and 100.0% specificity for detecting carcinoma compared to FFPE histology. The agreement between the Grade Group determined by NLM versus FFPE histology had an unweighted Cohen's Kappa of 0.588. The average NLM evaluation time was 2.10 minutes per biopsy. In this section, we investigate the similarities and differences of NLM versus FFPE H&E of prostate needle core biopsies from the pathologist's perspective on 170 biopsies. NLM images of benign tissue and carcinoma (including Gleason patterns) are described along with the challenges associated with this new technique.

5.3.2. MATERIALS AND METHODS

A total of 170 biopsies were collected from 63 patients who underwent in-bore MRI or MRI/ultrasound (US) fusion biopsy procedures. Only targeted cores, using 18-guage core biopsy devices, were included in this study. The biopsies used in this study were also used in Section 5.2. Written informed consent was obtained from all subjects. All research was performed according to protocols approved by Beth Israel Deaconess Medical Center Committee on Clinical Investigations and Institutional Review Board and Massachusetts Institute of Technology Committee on the Use of Humans as Experimental Subjects.

Biopsy preparation

Biopsies were placed in formalin after the biopsy procedure following standard practice. The first 22 biopsies were collected for NLM imaging immediately after the biopsy procedure.

Subsequent biopsies were collected for NLM imaging up to 1-3 hours after the biopsy procedure to comply with COVID-19 physical distancing restrictions. The additional delay did not alter NLM images.

All biopsies from a single patient were stained in parallel with acridine orange (40 µg/ml; #10050, Electron Microscopy Sciences, Hatfield, PA) and sulforhodamine 101 (40 µg/ml; S7635, Sigma-Aldrich, St. Louis, MO) in a 1:1 ethanol:water solution for 45 seconds and rinsed for 1-2 seconds in saline. Acridine orange provided nuclear contrast and sulforhodamine 101 provided cytoplasmic/stromal contrast. The biopsies were then placed on a single specimen holder with a glass window enabling rapid evaluation of all biopsies without changing specimen holders. Biopsy foam was used to apply gentle compression to ensure a flat imaging surface against the glass. The specimen holder was transferred to the NLM instrument.

Biopsy evaluation

The NLM instrument used to evaluate biopsies was previously described.[14] A line-scan camera integrated into the NLM instrument acquired a white-light photograph of the biopsy surfaces. The white-light photograph was displayed on the computer monitor along with the NLM images and a marker indicating the position of NLM imaging that was updated in real time to aid in NLM navigation. A genitourinary pathologist evaluated the biopsies in real time by translating the specimens to areas of interest. The NLM instrument used a short-pulsed Ti:Sapphire laser (Chameleon Ultra, Coherent, Inc.) at 1030 nm wavelength to excite acridine orange and sulforhodamine 101 fluorescence. A 20x, 0.75 NA air objective (CFI Plan Apo Lambda 20x, Nikon, Melville, NY) was used as in Section 5.2. The NLM images were updated at video rate and displayed in an H&E color scale. Vertical translation of the specimen enabled evaluation of

biopsies up to ~100 µm below the biopsy surface analogous to serial sectioning without the microtome. NLM images were recorded for post-procedural analysis.

After NLM imaging, the biopsies were placed in formalin and submitted for standard formalin fixed paraffin embedded (FFPE) histology. After diagnosis and finalizing the pathology report for clinical care, the FFPE H&E sections were compared to the NLM images. Similarities and differences between NLM and FFPE H&E were analyzed.

5.3.3. RESULTS

Benign prostate biopsies

NLM images of benign prostate biopsies and corresponding FFPE H&E are shown in **Figure 5.3**. Glandular hyperplasia is shown in **Figure 5.3**A. The biopsy surface (left) appears hypercellular and is difficult to interpret. By translating the NLM imaging plane on the z axis in real time, tissue below the biopsy surface was evaluated. At 10 µm below the biopsy surface (center), the benign glands were more easily interpretable. Glands lined with secretory cells with abundant cytoplasm and uniform, basally positioned nuclei are clearly visualized. The corresponding FFPE H&E histology (right) shows similar benign hyperplasia. **Figure 5.3**B shows benign glands with basal and secretory cell layers visible in the NLM and FFPE H&E section. **Figure 5.3**C shows benign stroma and glands with a large corpora amylacea. The laminated structure of the corpora amylacea is seen in both the NLM image and FFPE H&E section. Glands with basal cell hyperplasia are seen in **Figure 5.3**D and E on NLM images and corresponding FFPE H&E. A glandular secretory component is visualized on NLM and FFPE H&E in the upper portion of **Figure 5.3**E.

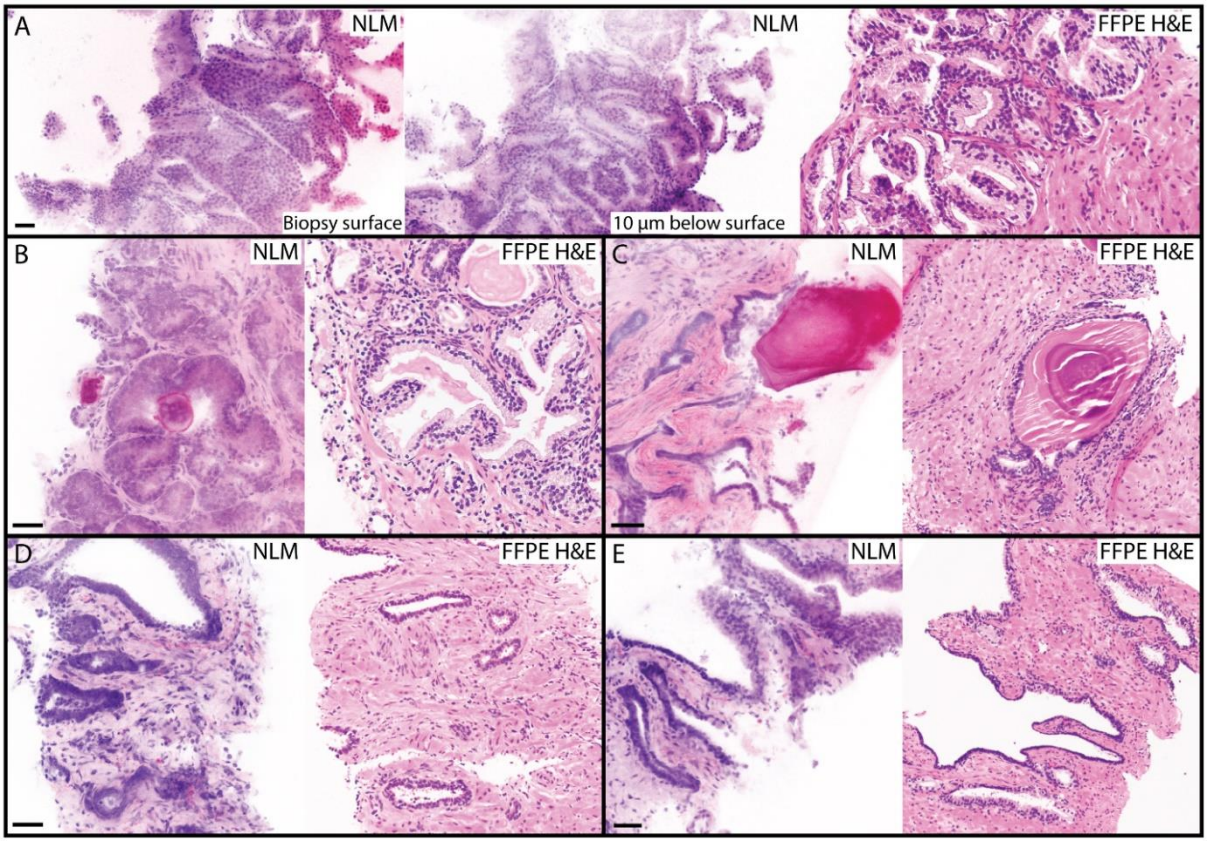

Figure 5.3. Nonlinear microscopy (NLM) images of benign prostate needle core biopsies. A. An NLM image of glandular hyperplasia acquired at the biopsy surface (left), at 10 µm below the biopsy surface (center), and a corresponding formalin fixed paraffin embedded (FFPE) H&E section (right). The surface can often appear hypercellular and can be difficult to interpret. **B.** Benign glands with a basal and secretory cell layers visualized in an NLM image (left) and a corresponding FFPE H&E section (right). **C.** Benign glands with a large corpora amylacea (NLM: left, FFPE H&E: right). **D.** Basal cell hyperplasia (NLM: left, FFPE H&E: right). **E.** Basal cell hyperplasia (bottom) with a glandular secretory cell component (top) (NLM: left, FFPE H&E: right). Scale bars = 50 µm.

An NLM image and corresponding FFPE H&E section of a biopsy with seminal vesicle mucosa is shown in **Figure 5.4**A. Closely packed glands characteristic of seminal vesicle mucosa are seen in the NLM image. The cytoplasmic yellow-brown pigment seen in seminal vesicle

epithelium on FFPE H&E is not present in NLM images. Instead, unstained areas occur (arrow). In **Figure 5.4**B, an NLM image of a nerve with adjacent ganglion cells (arrows) is seen. Nissl substance has a characteristic basophilic appearance.

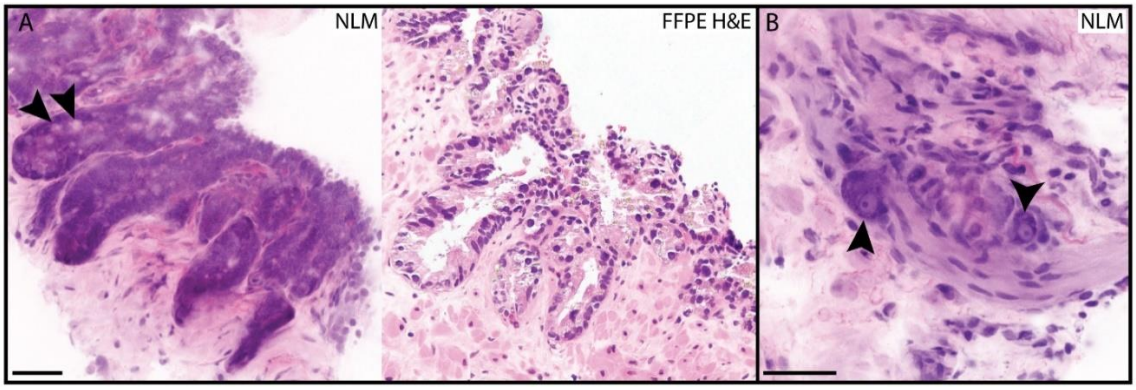

Figure 5.4. Nonlinear microscopy (NLM) images of seminal vesicles and nerves from prostate needle core biopsies. A. An NLM image (left) and a corresponding formalin fixed paraffin embedded (FFPE) H&E section (right) of seminal vesicle mucosa. Yellow-brown pigment in the cytoplasm does not stain in NLM (arrow). **B.** An NLM image of a nerve with adjacent ganglion cells. The prominent nucleoli of ganglion cells (arrow) are apparent. Nissl substance stains basophilic on NLM. Scale bars = 50 µm.

Carcinoma

Nonlinear microscopy enabled visualization of carcinoma and recognition of Gleason patterns in prostate needle core biopsies.

Gleason pattern 3

NLM images and corresponding FFPE H&E sections of prostate needle core biopsies with Gleason pattern 3 adenocarcinoma are shown in **Figure 5.5**. Discrete, well-formed glands are

clearly visualized with NLM. Bright eosinophilic secretions, as seen in **Figure 5.5**A, C, D, and E, are more prevalent in lumens of Gleason pattern 3 adenocarcinoma glands in tissues visualized with NLM than on FFPE H&E sections. These secretions can appear solid, as in **Figure 5.5**A, D, and E or have a crystalline appearance as in **Figure 5.5**C. Pattern 3 glands can also appear without eosinophilic secretions as shown in **Figure 5.5**B.

Foamy gland carcinoma does not have the characteristic foamy appearance usually seen on FFPE H&E in NLM images (**Figure 5.5**C). Foamy gland carcinoma visualized using NLM has the same architectural features as FFPE H&E section, namely discrete, well-formed glands that are often closely packed. Many cytological features are also similar to FFPE H&E sections, such as smaller, basally located nuclei without prominent nucleoli, with abundant cytoplasm, but the cytoplasm appears eosinophilic and denser on NLM than on FFPE H&E sections. These similar architectural and cytologic features enable identification of foamy gland carcinoma.

Gleason pattern 3 glands can appear solid as shown in **Figure 5.5**D. In this case, gland lumens are difficult to visualize on NLM. However, the densely-packed glandular architecture and eosinophilic intraluminal secretions make the diagnosis of cancer apparent. Perineural invasion is also readily identifiable on NLM as shown in **Figure 5.5**E.

NLM images and corresponding FFPE H&E of Gleason pattern 3 with small discrete glands are shown in **Figure 5.6**. Carcinoma infiltrating the prostatic stroma between benign glands is shown in **Figure 5.6**B. The benign glands are easily identifiable on the NLM image and the basal and secretory cell layers are seen.

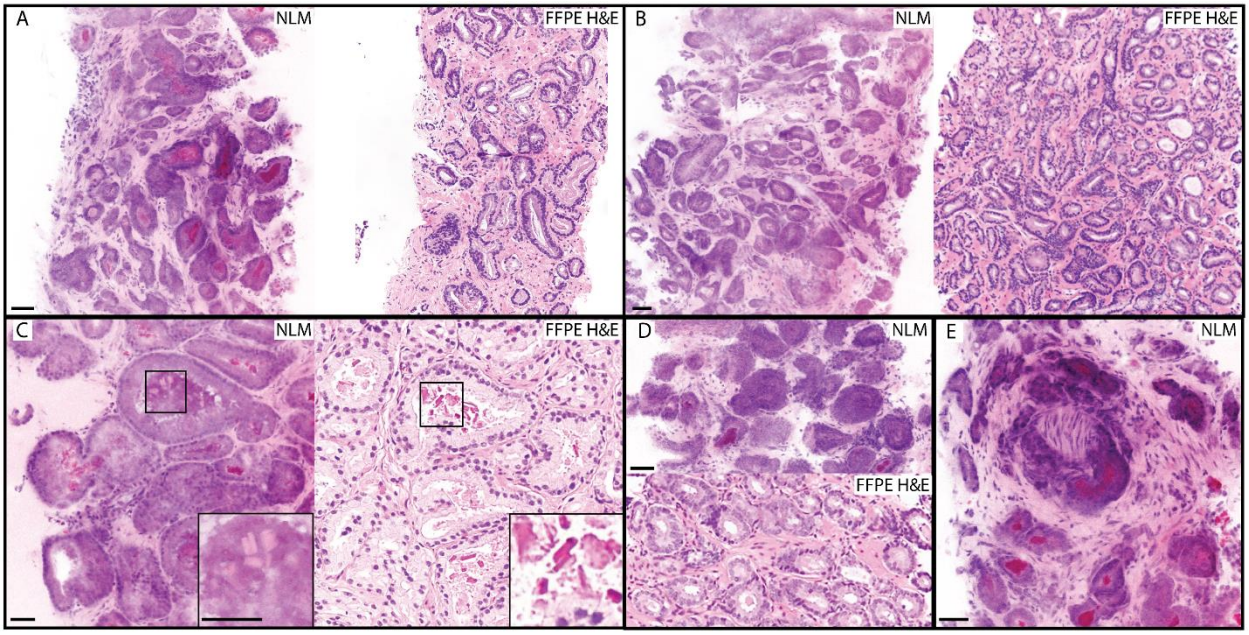

Figure 5.5. Nonlinear microscopy (NLM) images of Gleason pattern 3 prostatic adenocarcinoma from prostate needle core biopsies. A. Discrete, well-formed glands are clearly visualized with NLM (left) and formalin fixed paraffin embedded (FFPE) H&E (right). Bright, solid eosinophilic secretions are more commonly seen in these NLM images of Gleason pattern 3. **B.** Gleason pattern 3 without eosinophilic secretions (NLM: left, FFPE H&E: right). **C.** An example of foamy gland adenocarcinoma (NLM: left, FFPE H&E: right). The cytoplasm of secretory cells visualized using NLM does not have the characteristic foamy appearance present in FFPE H&E. The intraluminal secretions may have a crystalline appearance (inset). **D.** Malignant glands that appear solid (NLM: top, FFPE H&E: bottom). **E.** An example of an NLM image showing perineural invasion (center). Scale bars = 50 μm.

Gleason pattern 4

NLM images and corresponding FFPE H&E sections of prostate needle core biopsies with Gleason pattern 4 adenocarcinoma are shown in **Figure 5.7** and **Figure 5.12**. Fused glands in a cribriform pattern, characteristic of Gleason pattern 4, are readily visualized in NLM images. Gleason pattern 4 admixed with pattern 3 is shown in **Figure 5.7**B, C, and F and **Figure 5.12**. In

C and E, the pattern 3 glands are small whereas in F, the pattern 3 glands are large and have eosinophilic intraluminal secretions. Like in FFPE H&E sections, NLM images of Gleason pattern 4 rarely contain intraluminal secretions. Gleason pattern 4 with glandular lumens occluded by proliferating cells is shown in **Figure 5.7**D. Clear cytoplasmic vacuoles are visualized on NLM images and FFPE H&E sections (inset). A glomeruloid pattern is shown in **Figure 5.7**E. The cribriform proliferation attached to one edge of the gland giving the characteristic glomeruloid appearance is apparent in both the NLM image and FFPE H&E.

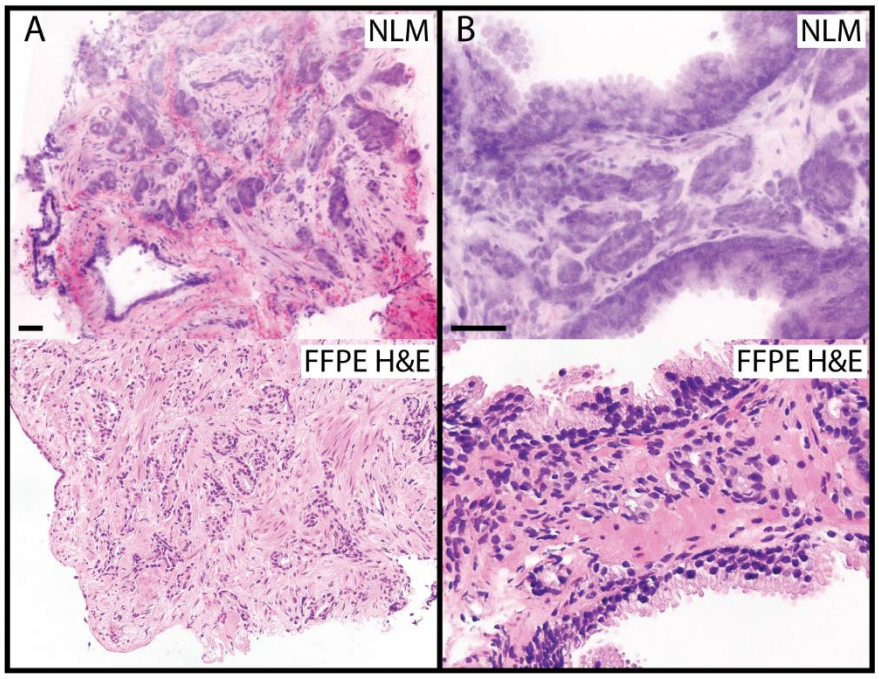

Figure 5.6. Nonlinear microscopy (NLM) images of Gleason pattern 3 prostatic adenocarcinoma with small glands in prostate needle core biopsies. A. Small discrete glands. **B.** Malignant glands infiltrating the prostatic stroma between benign glands. Basal and secretory cell layers are seen in the benign glands in the NLM image and FFPE H&E section. A-B NLM: top, formalin fixed paraffin embedded (FFPE) H&E: bottom. Scale bars = 50 µm.

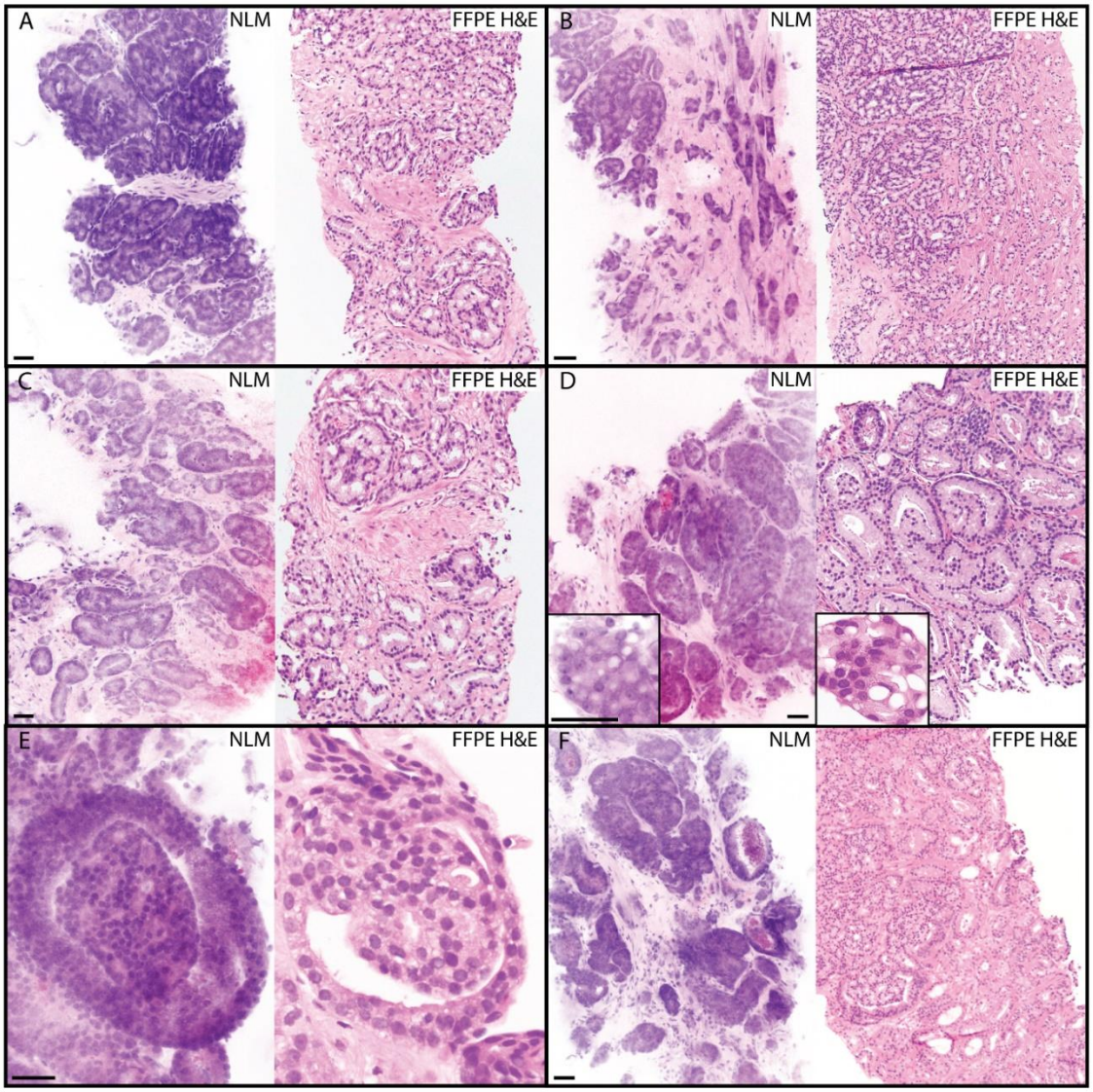

Figure 5.7. Nonlinear microscopy (NLM) images of Gleason pattern 4 prostate adenocarcinoma from prostate needle core biopsies. A. Typical Gleason pattern 4 with fused glands in a cribriform pattern. **B.** Distinct areas of Gleason pattern 4 on the left side of the biopsy and pattern 3 on the right side of the biopsy. **C.** Gleason pattern 4 with a component of pattern 3 throughout the image. **D.** Gleason pattern 4 with glandular lumina occluded by proliferating cells. Cytoplasmic vacuoles are seen (inset). **E.** A glomeruloid pattern. **F.** Gleason pattern 4 with a cribriform structure admixed with pattern 3. The Gleason pattern 3 is composed of large distinct glands with intraluminal secretions (right). In contrast, the Gleason pattern 4 does not contain intraluminal secretions. A-F NLM: left, formalin fixed paraffin embedded (FFPE) H&E: right. Scale bars = 50 µm.

Mucin-producing prostatic adenocarcinoma from prostate needle core biopsies is visualized in NLM images and corresponding FFPE H&E in **Figure 5.8** and **Figure 5.13**. Rapid evaluation of tissue below the biopsy surface with NLM enabled analyses the cribriform pattern in this biopsy at multiple depths (**Figure 5.8**B). The blue tinge seen in mucin on FFPE H&E sections is not present on NLM images of fresh prostate biopsies. This could be partly due to the different staining characteristics of hematoxylin versus acridine orange. It is also likely due to the mucin not being fixed to the glands and therefore the mucin is free floating in fresh tissue. The free-floating mucin partially covers the surface of the biopsy occluding NLM imaging in some biopsy areas (light appearance in dashed oval in **Figure 5.8**A).

Gleason pattern 5

NLM images and corresponding FFPE H&E sections of prostate needle core biopsies with Gleason pattern 5 adenocarcinoma are shown in **Figure 5.9**. Sheets of tumor cells with prominent nucleoli lacking gland formation are seen in the NLM image and corresponding FFPE H&E section in **Figure 5.9**A. NLM images of cords and strands of malignant cells are shown at two different depths below the biopsy surface in **Figure 5.9**B. Multiple depths confirmed that gland lumen formation was minimal consistent with Gleason pattern 5, which is confirmed on the corresponding FFPE H&E section (bottom). Extraprostatic extension, with carcinoma in adipose tissue, in another area of the same biopsy is also clearly visualized with NLM as shown in the inset of **Figure 5.9**B. Friable, high-grade tumor can appear loosely connected to the prostate stroma in NLM images of fresh biopsy tissue (**Figure 5.9**C). Since the tissue is not fixed or embedded in paraffin, the layer of stained tumor cells can become detached from the biopsy (orange arrow, bottom) leaving an area of weakly stained cells, which have minimal NLM signal (black arrow).

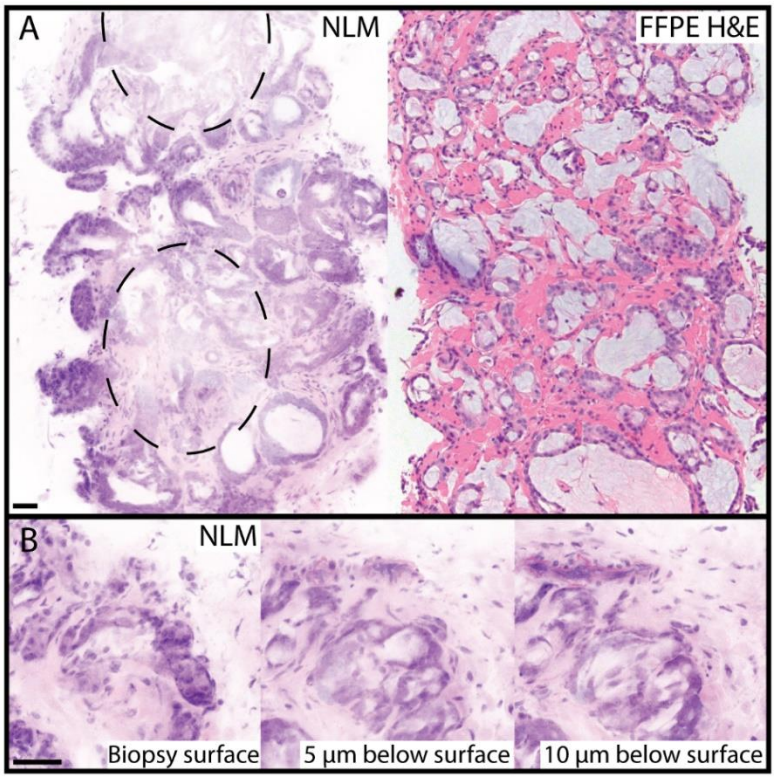

Figure 5.8. Nonlinear microscopy (NLM) images of mucin-producing prostatic adenocarcinoma from prostate needle core biopsies. A. An NLM image (left) and a corresponding formalin fixed paraffin embedded (FFPE) H&E section (right). Mucin does not stain in NLM images and therefore the blue tinge seen in the FFPE H&E is not present in NLM. In NLM evaluation of fresh tissue, the mucin covers the surface of the biopsy (dashed oval) and thus occludes NLM imaging. This occlusion appears as lighter regions (dashed circle) throughout the biopsy. **B.** NLM images acquired at the surface and 5 µm and 10 µm below the surface of the biopsy shown in A. The cribriform pattern varies in depth. Scale bars = 50 µm.

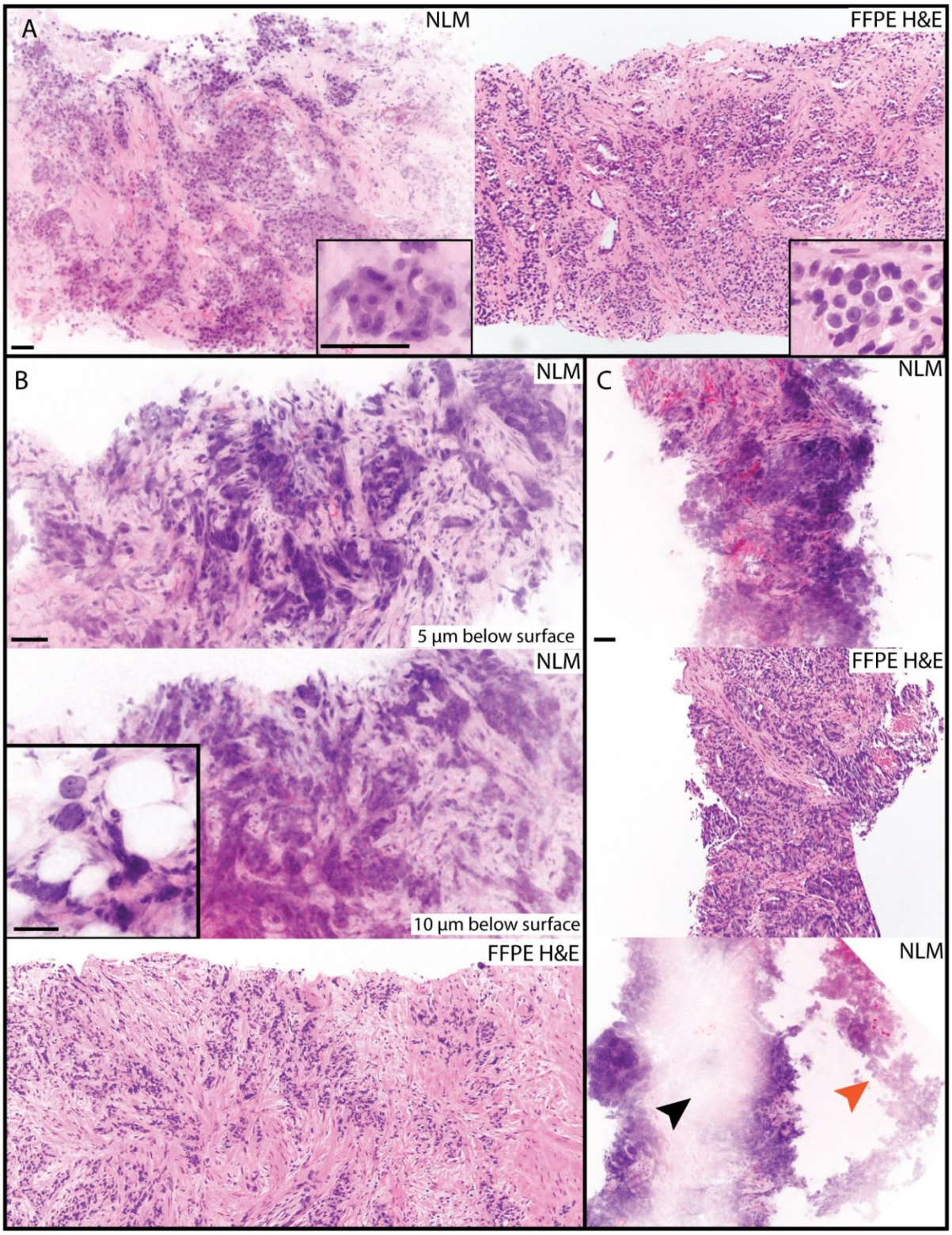

Figure 5.9. Nonlinear microscopy (NLM) images of Gleason pattern 5 prostatic adenocarcinoma from prostate needle core biopsies. A. Gleason pattern 5 consisting of sheets

of tumor cells without gland formation (NLM: left, corresponding formalin fixed paraffin embedded (FFPE) H&E: right). A high magnification image showing prominent nucleoli is shown inset. **B.** An NLM image of Gleason pattern 5 consisting of cords and strands of cells with minimal lumen formation acquired 5 µm below the biopsy surface (top), an NLM image acquired 10 µm below the biopsy surface (center), and a corresponding FFPE H&E (bottom). Evaluating NLM images at multiple depths confirmed that gland lumina were limited. The inset shows carcinoma in adipose tissue from another area of the biopsy. **C.** An NLM image of a high-grade tumor that appears loosely connected to the stroma (top) and a corresponding FFPE H&E section (center). In another area of this biopsy, tumor cells stained with acridine orange and sulforhodamine 101 became detached from the biopsy (orange arrow) in the NLM image (bottom) leaving an area of weakly stained tissue, which was absent of NLM signal (black arrow). Scale bars = 50 µm.

Variation of pathology at different depths

Visualizing biopsies at multiple different depths with NLM enables evaluation that is more comprehensive than FFPE H&E without requiring laborious and time-consuming serial sections in areas of uncertainty. **Figure 5.10**A demonstrates NLM analysis of variation in pathology in depth. A nerve free of carcinoma is present 12 µm below the surface (dashed circle) while perineural invasion is identified 10 µm deeper (B, dashed circle). This capability can augment the assessment of Gleason patterns. **Figure 5.10**C-E shows a biopsy with large, malignant glands with intraluminal secretions adjacent to chronic inflammation and benign glands. D. and E. are NLM images acquired 4 µm and 8 µm below C, respectively. In C, there appears to be a potential focus of glands in a cribriform pattern (black box) that evolves into a single discrete gland in E.

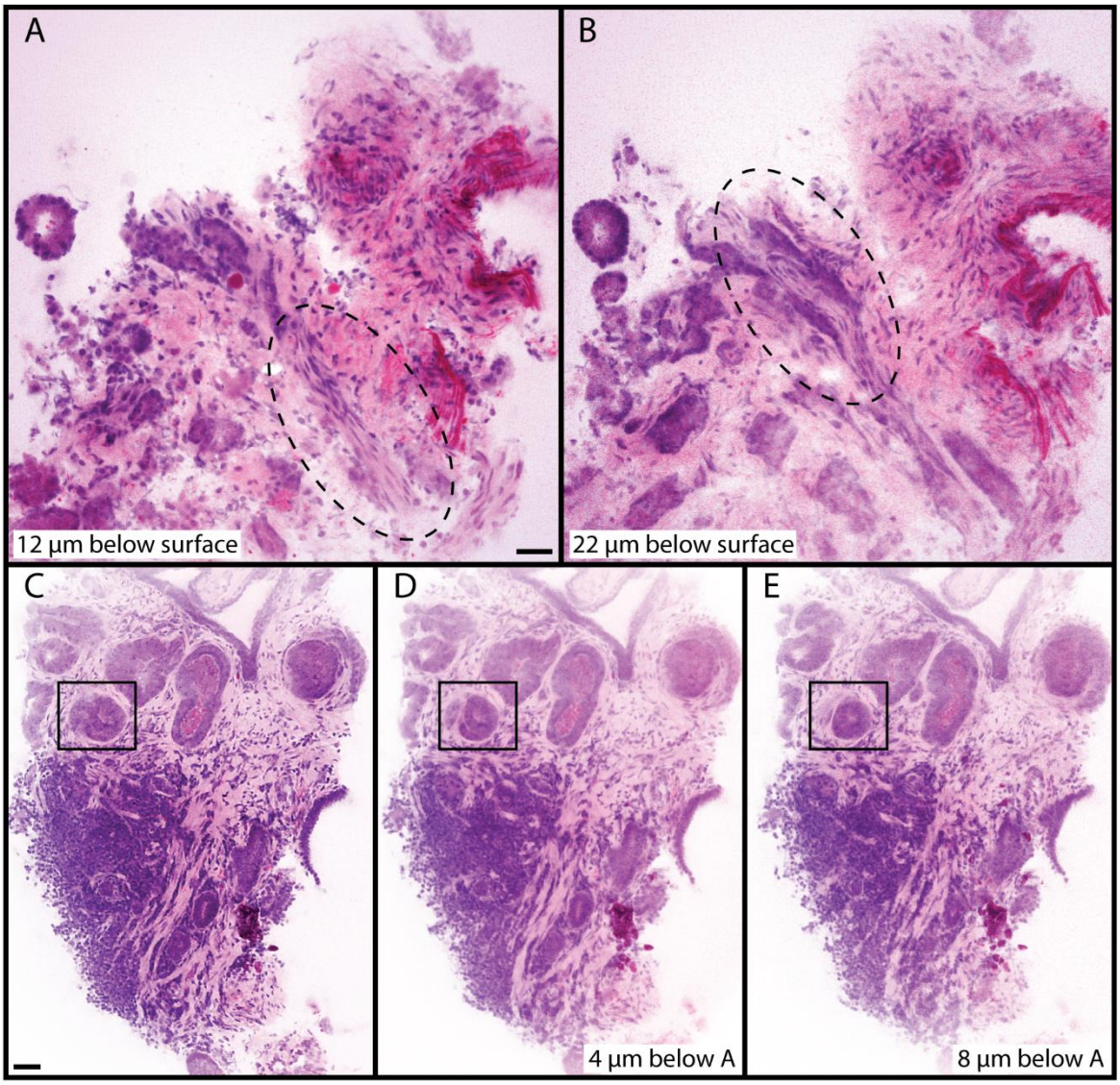

Figure 5.10. Pathology variations when changing the depth (z axis) of nonlinear microscopy (NLM) imaging. A. A nerve (dashed circle) uninvolved by carcinoma at 12 µm below the biopsy surface becomes B. involved by carcinoma 22 µm below the tissue surface. C. Large, malignant glands with intraluminal secretions adjacent to chronic inflammation and benign glands. D. and E. are NLM images acquired 4 µm and 8 µm below C, respectively. In C, there appears to be a potential focus of cribriform pattern (black box), which evolves into a single discrete gland in E. Scale bars = 50 µm.

5.3.4. DISCUSSION

NLM enables interpretation of prostate biopsies in minutes. Features of benign tissue, such as benign glands with basal and secretory cell layers, benign stroma with fibroadipose tissue, nerves, and vessels, and glandular and basal cell hyperplasia were readily visualized with NLM. Features of carcinoma, such as small, infiltrating glands that lack basal cells, nuclear enlargement, and prominent nucleoli, were visualized well with NLM. Furthermore, Gleason patterns could be differentiated, including the discrete, well-formed glands of Gleason pattern 3, cribriforming, fused glands, and glomeruloid patterns of Gleason pattern 4, and the sheets of cells with minimal gland formation of Gleason pattern 5.

NLM evaluation of prostate needle core biopsies enables visualization of many of the features present in FFPE H&E (as described above). The similarities reduce training requirements for interpretation and makes NLM a promising technique for rapid prostate biopsy diagnosis. However, it is important to recognize that NLM images are not FFPE H&E sections. Misunderstandings can result from relying too heavily on previous FFPE H&E experience. It is critical that the pathologist understands the differences in fresh tissue NLM imaging in order to confidently and accurately interpret images. We characterize these differences below to enable more accurate interpretation of NLM images.

Dehydrated, paraffinized tissue versus fresh tissue

Paraffin processing, which includes formalin fixation, alcohol dehydration, and paraffin embedding, results in reduced tissue volume, cell shrinkage, and cytoplasmic retraction. As a result, when compared to paraffin processed tissue, structures such as glands and cells visualized on fresh tissue with NLM appear thicker and more crowded (example: **Figure 5.3**A). Furthermore, the cell boarders in fresh tissue are less sharp due to this crowding and they have rounder, fuller

appearing cytoplasm. The lack of dehydration in NLM images also results in larger and more frequent prominent nucleoli throughout carcinoma compared to FFPE H&E, which can be a useful diagnostic feature.

Visualization of tissue prior to paraffin processing also results in additional cytoplasmic and luminal contents being present. For example, in the foamy gland variant of carcinoma, the characteristic foamy cytoplasm is not present on NLM and instead eosinophilic contents are seen (**Figure 5.5**C). Luminal contents, such as intraluminal secretions in low grade carcinoma (Gleason 3), are more frequent in NLM than FFPE H&E likely due to the reduction in processing. The frequent and clearly identifiable secretions are a useful diagnostic marker in NLM and may help differentiate benign hyperplasia.

Physical sectioning with a microtome versus optical sectioning

Unlike in FFPE histology where the axial resolution is determined by the thickness of microtome sections and lateral resolution determined by the objective lens, both the axial and lateral resolution in NLM imaging of thick tissue specimens is determined by the objective. A higher NA/power objective provides higher axial resolution (equivalent to a thinner section) enabling greater differentiation of architectural (Gleason patterns) and cytological details. For example, when going from a 5x to 10x objective the field of view is halved in both NLM and FFPE histology. However, the thickness of tissue visualized with NLM ranges from ~20 μm (depending on the microscope) to ~8 μm whereas the FFPE H&E always has a 5 μm physical thickness. This fact is important to recognize when interpreting images since when the axial section thickness increases, glands appear more crowded potentially resulting in false positive diagnoses.

There is a tradeoff between image resolution and speed in NLM evaluation. With larger prostatectomy specimens, a 10x, 0.45 NA objective enabled accurate and rapid cancer diagnoses, as described previously[88], however the limited axial (z) resolution made differentiation of Gleason patterns in biopsies difficult. In this study we used a 20x, 0.75 NA objective which improved visualization of architectural and cytological details. It is important to note, however, that NLM can use multiple objectives interchangeably like a traditional histology microscope[14] and therefore is not limited to a single resolution.

White-light transillumination versus fluorescence

Generation of NLM and FFPE H&E images result from different physical processes. FFPE H&E evaluation is done using transillumination by a white light. In this method, areas of higher dye concentration absorb more light and appear darker. NLM images are generated using epi-illumination and fluorescence detection. Areas of higher dye concentration have more fluorescence emission and generate more signal. To visualize the NLM images in an H&E color scale, they are remapped using Virtual Transillumination Microscopy (VTM).[6] VTM enables colors and intensities of the nuclear and cytoplasmic/stromal channels to be individually adjusted to suit the user's preference in real time.

White-light transillumination of an FFPE H&E slide also enables the whole visible spectrum to be visualized whereas NLM uses two discrete color channels, which collect the fluorescence from the acridine orange and sulforhodamine 101. Therefore, only combinations of the two hues that correspond to the two channels are represented in NLM and features that rely on color such as bland nuclei are less apparent, less consistent, or impossible to generate. For example, the bright red appearance of red blood cells and the yellow-brown pigment in seminal vesicles are not apparent on NLM.

Staining with Hematoxylin and Eosin versus Acridine Orange and Sulforhodamine 101

Acridine orange and sulforhodamine 101 have slightly different staining specificities than hematoxylin and eosin. For example, distinct pink elastic fibers can be seen throughout the stroma and in the elastic lamina of vessels on NLM and are not present on FFPE H&E. Mucin is not stained with acridine orange or sulforhodamine 101, leaving areas of mucin absent of NLM signal. Furthermore, staining can also be less homogenous in freshly excised tissue than in permeabilized, dehydrated sections resulting in variations in cytoplasmic colors between or within biopsies.

Two dimensional analysis versus three dimensional analysis

Rapidly evaluating multiple depths with NLM can be advantageous. For example, multiple depths in **Figure 5.3**A are used to more clearly define benign tissue, in **Figure 5.8**A to define the cribriform structure in mucin-producing carcinoma, and in **Figure 5.9**A to verify that there is minimal or no glandular formation in a biopsy with Gleason pattern 5. Evaluating multiple depths can also complicate biopsy evaluation. Classification of prostate carcinoma with Gleason scores is important for predicting clinical course and disease behavior.[113] Gland formation that is distinct and individual is associated with less aggressive tumors. Conversely, architectural complexity and loss of gland formation portends an increased malignant potential. Several groups, however, have shown that Gleason patterns change throughout the depth of individual biopsies.[109,114,115] This complicates the comparison of FFPE H&E and NLM, especially in cases of clearly glandular Gleason 3 pattern vs gland fusion/luminal narrowing Gleason 4 pattern (**Figure 5.10**). Sections at multiple depths are typically evaluated in FFPE histology, but NLM can image continuous variations in depth in real time, enabling volumetric assessment. This is a unique capability for assessing tumor characteristics that may improve upon two-dimensional visualization in FFPE.

Necrotic/high grade areas

Biopsies that are necrotic or friable such as in cases of high-grade carcinoma have cells that slough off during manipulation. Since the biopsies are not stabilized through fixation and paraffinization, these cells can float off the biopsy and appear in different regions of the biopsy leaving areas devoid of cells (**Figure 5.9**C).

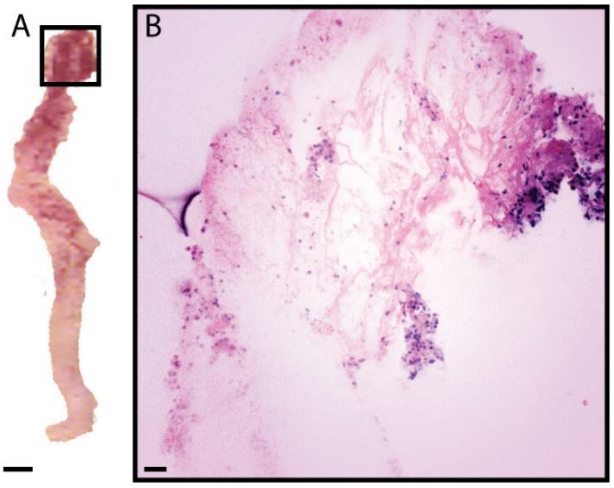

Figure 5.11. Nonlinear microscopy (NLM) image of a biopsy with substantial blood covering the surface. A. A photograph of a needle core biopsy covered in blood in the upper portion. (Scale bar = 500 µm). **B.** An NLM image of the biopsy shown in A acquired from the region in the black box. The blood prevents adequate staining of the biopsy causing this region to have limited NLM signal and appear white. Thus, hemorrhage may cause difficulties in interpretation, as seen in this example. (Scale bar = 50 µm).

Blood

Large amounts of blood in the biopsy can confound interpretation. The blood prevents adequate staining of the biopsy causing regions to have limited NLM signal and appear white

(**Figure 5.11**). Since blood itself also is stained minimally with acridine orange or sulforhodamine 101, little signal is generated. This could cover pathology (although we have not observed this in any cases we evaluated) or make determination of Gleason scores and extent of tumor difficult.

Surface artifacts

Core needle biopsies usually have obscuring artifacts, are hypercellular (**Figure 5.3**A), and have loose cells on their surfaces due to damage from the biopsy needle or handling the fragile tissue (**Figure 5.9**C). These artifacts are not present on FFPE histology since slides are obtained from subsurface tissue after facing the paraffin block. The capability of visualizing subsurface tissue with NLM is critically important for interpretation of freshly biopsied tissue.

Limitations and conclusions

There are several limitations to this study. It is primarily a qualitative analysis performed by few pathologists. A quantitative analysis measuring accuracy of NLM diagnosis of prostate needle core biopsies was described in Section 5.2. Future studies will need to include a larger population of pathologists and multiple institutions. Biopsies were placed in formalin for a short period (10 minutes to 3 hours) prior to NLM imaging, which would not likely be the case if performing NLM evaluation during a biopsy procedure. However, we saw no apparent differences between freshly excised tissue and biopsies that were put in formalin for a short period. The NLM instrument used in this study is a prototype currently being developed for wider clinical use. Future larger scale studies are still needed.

This study presents a comprehensive comparison of rapid NLM evaluation of prostate needle core biopsies to FFPE H&E. Benign prostate tissue and carcinoma can be differentiated and Gleason patterns determined. Differences in the appearance of prostate pathologies visualized with

NLM and FFPE H&E are defined and training and practice enables accurate and consistent NLM evaluation. NLM is a promising method for future rapid evaluation of prostate needle core biopsies.

5.3.5. SUPPLEMENTARY FIGURES

Figure 5.12 and **Figure 5.13** are additional figures showing biopsies of Gleason pattern 3 admixed with pattern 4 and mucin-producing prostatic adenocarcinoma.

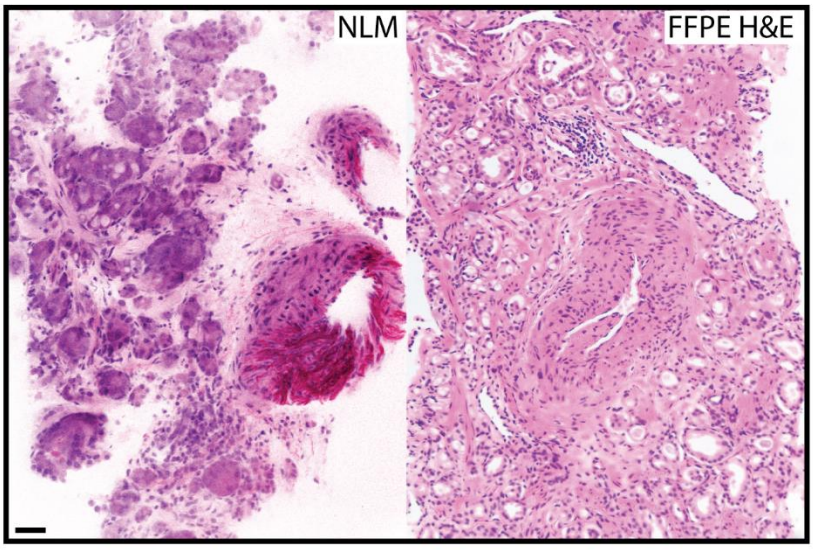

Figure 5.12. Nonlinear microscopy (NLM) image of Gleason pattern 3 admixed with pattern 4. A large vessel is seen in the center of the image. The elastic lamina has a prominent pink appearance in the NLM image which is not seen in the formalin fixed paraffin embedded (FFPE) H&E section. Scale bar = 50 µm.

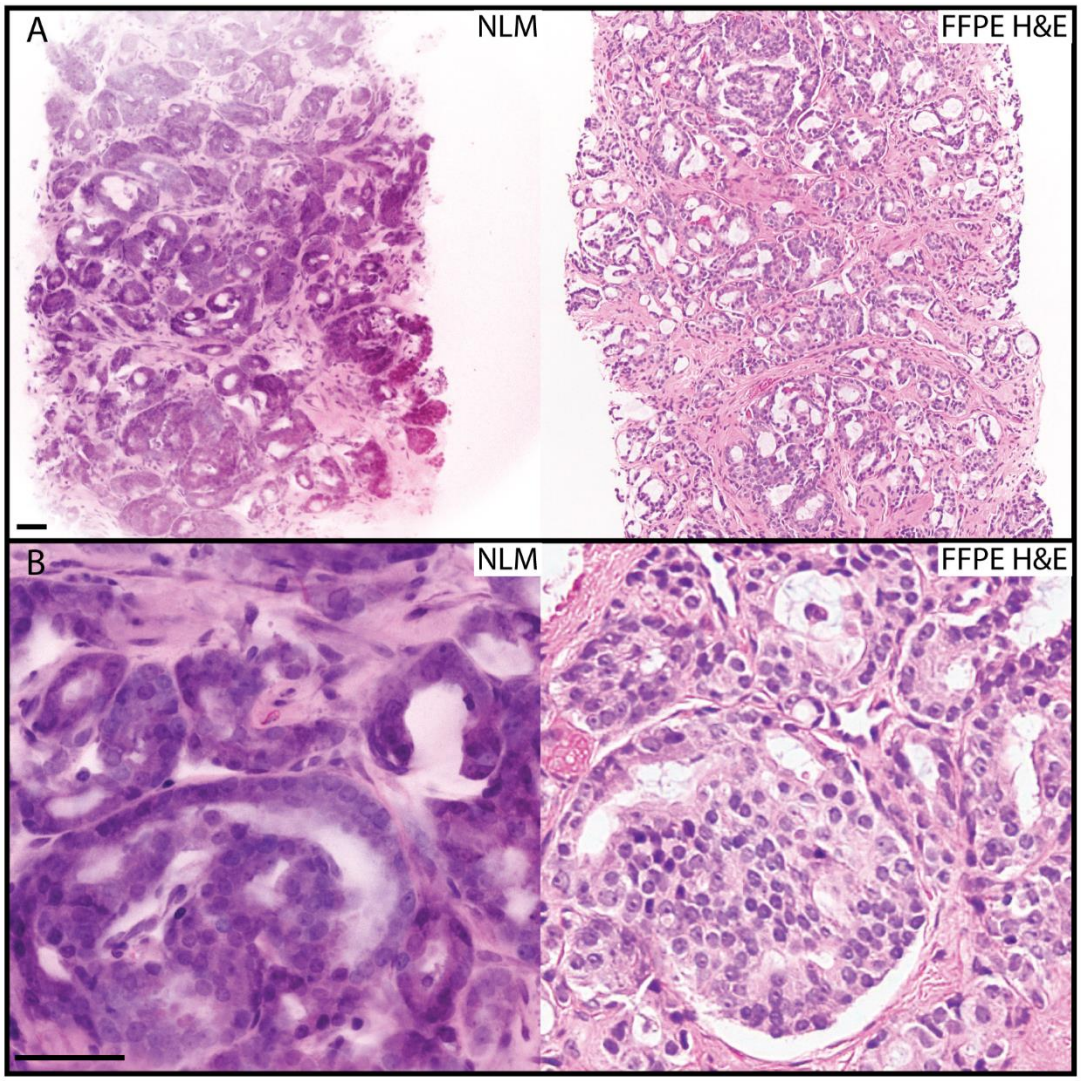

Figure 5.13. Nonlinear microscopy (NLM) images of a mucin-producing prostatic adenocarcinoma with Gleason patterns 3 and 4. A. An NLM image (left) and a corresponding formalin fixed paraffin embedded (FFPE) H&E section (right). **B.** A high magnification NLM image (left) and corresponding FFPE H&E section of the biopsy shown in A. Cribriform glands are seen. Round, dilated and empty spaces in the NLM image correspond to the mucin in the FFPE H&E image. The gray-blue tinge of mucin seen in the FFPE H&E is not present in NLM. Scale bars = 50 µm

Chapter 6

Three dimensional evaluation of archival renal biopsies using NLM

6.1. INTRODUCTION

Thorough examination of the renal biopsy enabling classification and mapping of disease will be a major part of the effort to improve clinical therapies and understand renal disease.[116] This could be especially important in diseases that have a focal injury pattern. Current standard histologic sampling techniques analyze only a small fraction of the renal biopsy. This means that a substantial amount of biopsy information is missed and large stores of archival paraffin blocks are available for analysis.

In diseases with focal injury patterns, only a limited portion of glomeruli have abnormalities that are apparent in paraffin histology and the abnormalities can also be restricted to small portions of glomeruli. Because only a small fraction of tissue is evaluated in paraffin histology, characterization of focal diseases can be challenging. A primary example of this is differentiating between minimal change disease (MCD) and focal segmental glomerulosclerosis (FSGS) which is important for predicting therapeutic response and disease prognosis.[117] Both diseases present with proteinuria, diffuse podocyte effacement, and minimal immune deposits under immunofluorescence and electron microscopy studies.[117] MCD has unremarkable changes in paraffin histology, while FSGS is characterized by sclerotic lesions in a small population of glomeruli, at least in initial phases.[118] The more glomeruli that are evaluated in paraffin histology, the higher possibility that a glomeruli affected by FSGS will be found.[119] A 17% increase in the number of glomeruli found to be involved with FSGS was found when evaluating biopsies via serial sections compared to the standard-of-care sectioning.[120] Further, accurately determining the

extent of involved glomeruli has important implications for pathogenesis and potential therapeutic response.[120]

Other focal diseases including anti-neutrophil cytoplasmic antibody (ANCA) glomerulonephritis (GN) often presents as focal and segmental necrotizing and crescentic glomerulonephritis.[121] It has been reported that 73% of glomeruli in focal ANCA associated GN are normal while only 14% of glomeruli have segmental crescentic lesions, and 6.5% have globally sclerotic lesions.[122] Having high proportions of normal tissue in renal biopsies makes it difficult to consistently quantify disease severity or prognosis based on two dimensional paraffin slides (interobserver and intraobserver variability is high).[123]

Systemic lupus erythematosus (SLE) nephritis can be focal and the interpretation and classification of the disease has poor reproducibility between pathologists.[124] In particular, differentiating SLE class II, a purely mesangial process, from SLE class III, which affects glomerular capillaries, can be difficult when limited tissue is evaluated.[125] Furthermore, classifications are based off of the extent of glomerular involvement which can be misrepresented when subsampling the tissue.[126] These difficulties and inconsistencies have led to a call for revisiting and reclassifying SLE nephritis.[126]

Diabetic nephropathy is another disease where focal lesions are an important part of disease classification. In diabetic nephropathy, the presence of Kimmelstiel-Wilson nodules defines Class III disease while lower classes are absent of these lesions.

Complete, three-dimensional (3D) analysis of tissue specimens has been shown to enhance information on disease and tissue pathology[127,128], however, this often requires laborious serial sectioning.[129,130] Combining tissue clearing with microscopy techniques such as nonlinear

microscopy (NLM) enables 3D analysis of tissue volumes without physical sectioning. These techniques have been demonstrated to improve examination of renal tissue from animals and human cadavers.[48,131–134]

This chapter demonstrates a technique for 3D analysis of archival renal biopsy specimens using NLM. Renal paraffin blocks are deparaffinized and stained with Hoechst and Eosin, then optically cleared using benzyl alcohol benzyl benzoate (BABB). 3D NLM imaging is performed and displayed using an H&E color scale. Quantitative analyses of glomeruli and tissue pathology are presented.

This work was done in collaboration with Tadayuki Yoshitake, James G. Fujimoto at Massachusetts Institute of Technology and Seymour Rosen and Milan Rosen at Beth Israel Deaconess Medical Center and Harvard Medical School. The work was supported in part by the National Institutes of Health R01-CA178636-06, R01-CA075289-20, the MIT Broshy Graduate Fellowship in Medical Engineering and Science, and the MIT Termeer Medical Engineering Graduate Fellowship.

6.2. MATERIALS AND METHODS

Tissue preparation

Archival renal biopsy paraffin blocks from 12 patients were collected. All research was performed according to Institutional Review Board protocols.

The paraffin blocks were melted and processed in a reverse cycle on a vacuum infiltrating processor (10 minutes at 65°C, 9 xylene washes, 5 ethanol washes, 1 water wash) to remove paraffin from the tissue. The tissue clearing method was based on a method described by Dent, *et*

al[135]. and Olsen, *et al.*[136] Solutions of increasing concentration of methanol (70% for 1 hour, 95% and 100% for 30 minutes each) with 40 µg/mL Hoechst 33342 (Life Technologies, Eugene, OR) and 1 µL/mL eosin Y (5% by weight in water, Sigma-Aldrich, St. Louis, MO) in each solution were used to dehydrate biopsies and label nuclear and cytoplasmic/stromal components. Nuclei were stained with Hoechst 33342 instead of acridine orange, which was used in previous chapters for evaluating freshly excised tissue, because acridine orange had a lot of nonspecific staining when specimens were stained for the long period of time required for dye penetration into thick tissue. Combining tissue staining with dehydration reduces tissue preparation time. The biopsies were rinsed in 100% methanol for 15 minutes to remove excess dye. Then the biopsies were optically cleared in a 2:1 solution of benzyl alcohol (ACS reagent, >99%, Sigma-Aldrich, St. Louis, MO, USA): benzyl benzoate (ReagentPlus®, >99%, Sigma-Aldrich, St. Louis, MO, USA) (BABB) for 4 to 6 hours. Staining and clearing was performed at 40°C on a shaker table to improve penetration.

NLM imaging and image processing

After staining and tissue clearing, the biopsies were placed on a glass coverslip and biopsy foam was used to maintain the biopsy's position against the glass surface. The biopsy foam does not cause architectural distortion since it only applies gentle compression to the fixed and processed biopsy.

A previously described nonlinear microscope[8] was used to evaluate the renal biopsies. A Ti:Sapphire femtosecond laser (Mira, Coherent, Santa Clara, CA) operated at 780 nm was scanned with resonant and galvanometer scanners through a 20X, 1.0 NA water immersion objective (XLUMPFL20XW, Olympus, Tokyo). A 525 nm high-pass dichroic beam splitter (T525lpxr, Chroma Technology Corporation, Bellows Falls, VT) split the Hoechst and Eosin fluorescent

emission light through two separate emission filters (FF02-460/80-25 and FF01-590/104-25, Semrock, Rochester, NY) onto two photomultiplier tubes (H7422P-40, Hamamatsu, Hamamatsu City, Japan). 1024 x 1024 pixel frames were acquired over a 0.49 x 0.49 mm area. Entire biopsy cross sections were acquired by automatically translating the biopsy with a precision linear motor stage and imaging overlapping frames at a single depth from the biopsy surface. Biopsy cross sections were then acquired every 4 μm in depth generating a 3D NLM dataset.

The tissue preparation (alcohol dehydration, staining, and clearing) required 6-8 hours. The NLM acquisition time varied depending on the size of the biopsy. The duration of imaging ranged from 10 minutes (450-frame dataset) to 5.5 hours (18,000-frame dataset). The microscope used was not optimized for speed and we expect that future version will provide large reductions in acquisition times.

After NLM imaging, the NLM images were mapped into an H&E color scale using an algorithm called Virtual Transillumination Microscopy.[6] The frames in each biopsy cross section were stitched together using Image Composite Editor (Microsoft, Redmond, WA) so that they could be viewed analogously to a whole slide image from a digital slide scanner.

After NLM imaging, biopsies were placed in 100% methanol for 1 hour to remove the BABB. The specimens were then re-processed in a vacuum infiltrating processor and re-embedded in paraffin. H&E, Periodic acid–Schiff (PAS), Jones methenamine silver, and Masson's trichrome paraffin embedded sections were made (**Figure 6.11**).

Analysis, segmentation, and counting

A renal pathologist with over 20 years of experience (SR) read the NLM images using OpenSeadragon, a web-based viewer that enables variable magnification review. Similarities and

differences between the NLM images, paraffin histology, and original archival biopsy pathology report were investigated.

3D volumes were reconstructed using Amira (ThermoFisher, Waltham, MA). Cysts, glomeruli, exudative lesions, and Kimmelstiel-Wilson nodules were manually segmented in Amira. Glomeruli were counted on the 3D NLM volumes. No automated segmentation or analysis algorithms were used in this initial study.

Tissue evaluated in the original pathology report vs NLM imaging

To make the original diagnoses (**Table 6.1**, column 3), pathologists typically evaluated 10-15 slides with 2-4 sections (2-3 μm thickness) per slide. To make the histology slides, serial sections (directly adjacent tissue) were not always used on adjacent slides. Instead sections were sampled through the block and much of the tissue was wasted. All tissue that was left in the block after microtome sectioning for paraffin histology was evaluated by NLM. Before microtome sectioning, the biopsies have a diameter of ~1 mm. Comparing the tissue thickness evaluated by NLM (**Table 6.1**, column 2) to the 1 mm initial diameter, provides an estimate on the remaining biopsy volume in the paraffin block.

6.3. RESULTS

Nonlinear microscopy images of renal biopsies: specific conditions

Results from 12 biopsies obtained from archival paraffin blocks are presented. **Table 6.1** shows a summary of the biopsies and patient diagnoses. NLM enables 3D evaluation of biopsy specimens, generating images that closely resemble paraffin H&E sections.

Biopsy #	Tissue thickness evaluated by NLM (μm)	Diagnosis
1	660 and 232	Acute tubular necrosis
2	448 and 268	Global sclerosis, interstitial fibrosis, tubular atrophy, and vascular disease
3	264 and 332	Diabetic nephropathy
4	292	IgA nephropathy
5	368	Diabetic nephropathy
6	200	FSGS with features of collapsing glomerulopathy
7	368	Thrombotic microangiopathy
8	388 and 88	IgA nephropathy with focal crescents
9	380 and 216	Diabetic nephropathy + IgA nephropathy
10	392 and 472	Tubular necrosis and calcification
11	312	Diabetic nephropathy
12	320	Advanced CKD with microcystic changes, consistent with lithium nephropathy

Table 6.1. Archival paraffin blocks analyzed with NLM. Twelve archival paraffin blocks were analyzed. In Biopsy 1, 2, 3, 8, 9, and 10 two fragments of tissue were in the block and analyzed with NLM. In the other biopsies, only one fragment was in the block. NLM analysis was performed on the entire biopsy tissue that was left in the archival block. The diagnosis was obtained from the original pathology report.

Diabetic nephropathy

Biopsy 3, 5, 9, and 11 were from patients diagnosed with diabetic nephropathy. NLM images corresponded closely to the paraffin H&E slides and enabled 3D visualization and analysis of many of the characteristic features of diabetic nephropathy. **Figure 6.1** and **Figure 6.2** show examples of diabetic nephropathy visualized with NLM.

Figure 6.1 shows a region of interest from a biopsy of a patient with advanced diabetic nephropathy (Biopsy 5) in NLM images selected at different levels. Three glomeruli are present

showing varying degrees of disease involvement. Glomerulus 1 is characterized by prominent endocapillary exudative lesions that are also present in Bowman's capsular area. The urinary space is largely occluded and associated with some degree of proliferation. Endocapillary cellularity is irregularly reduced. At deeper levels, Bowman's space is almost entirely lost and the glomerular tuft exudative lesions continue to be prominent and have a vacuolated (lipid) component (green arrow). In Glomerulus 2, the glomerular tuft in the first level (0 µm) has prominent exudative lesions with some degree of maintained endocapillary cellularity. At deeper levels, the urinary space becomes totally obliterated. Hyalinized arterioles are seen at the 40 µm and 60 µm level of Glomerulus 1 and 2, respectively (blue arrow). Glomerulus 3 shows even more advanced changes. The exudative lesions are now encircling the tuft, which is basically acellular matrix plus basement membranes. A corresponding paraffin H&E slide of the same region is shown (bottom right).

Figure 6.2A shows an example of a 3D NLM volume of a biopsy from a patient with diabetic and IgA nephropathy (Biopsy 9). **Figure 6.2**B shows a glomerular tuft displayed in 24 µm intervals. Glomerular mesangial expansion is seen by hypercellularity and matrix expansion, which occludes capillary lumens. Kimmelstiel-Wilson nodules are seen only at levels 120 µm and 144 µm. Thus, in a situation of mesangial expansion and hypercellularity (IgA), morphologically characteristic lesions are more clearly defined by 3D imaging. An NLM image and corresponding paraffin H&E slide of Biopsy 9 is shown in **Figure 6.2**C. Mesangial expansion and hypercellularity are seen in both images.

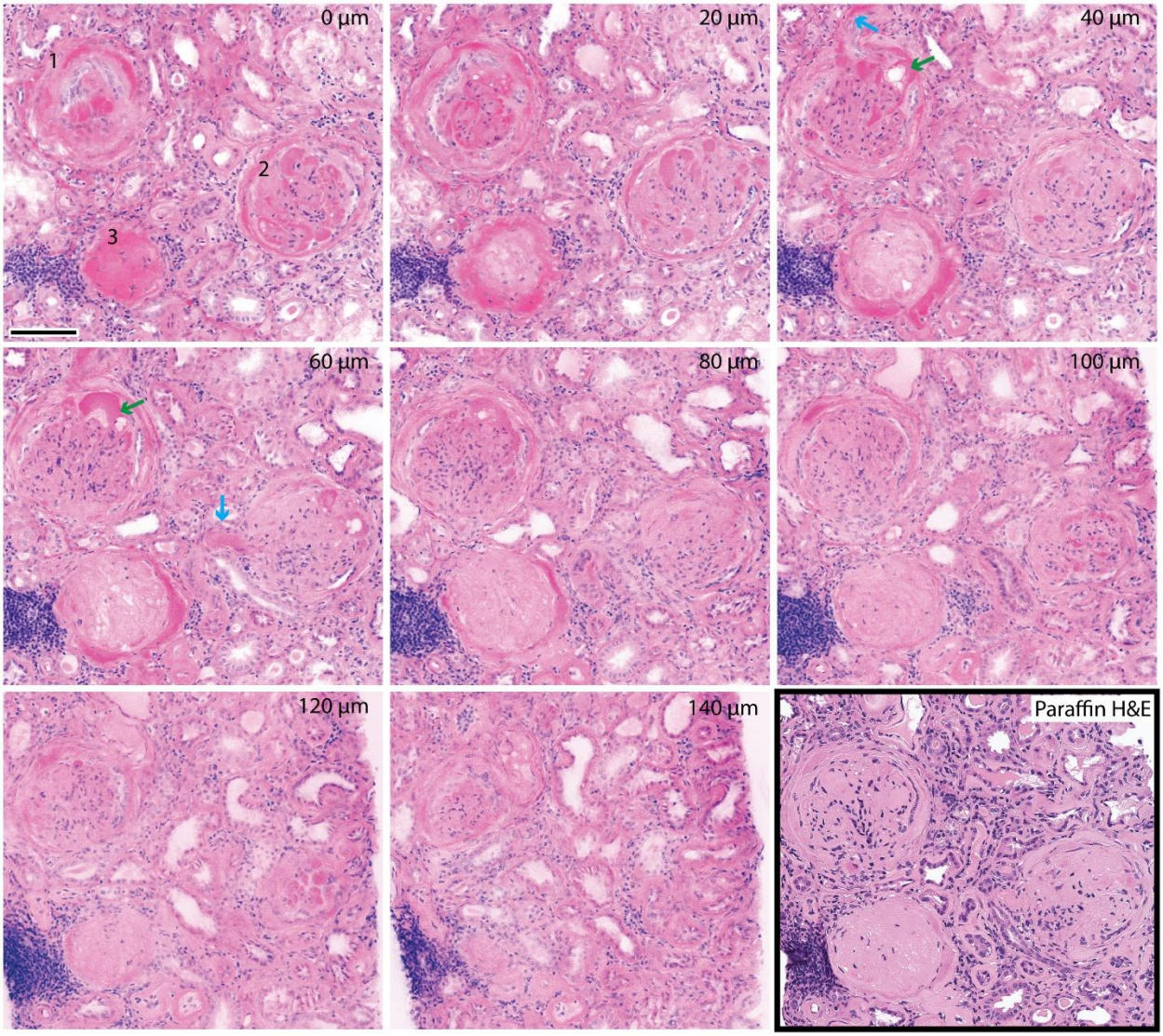

Figure 6.1. Three-dimensional NLM analysis of Biopsy 5: Diabetic nephropathy. NLM images of Biopsy 5 were acquired every 4 µm in depth. Images spaced 20 µm apart in depth show advanced glomerular changes in 3 different glomeruli (labelled 1, 2, and 3). Capillary lumens and Bowman spaces are occluded with reduction of the glomerular tuft to a collapsed acellular mass of basement membranes and matrix. Exudative lesions are abundant, have a vacuolated (lipid) component (green arrow), and can be seen as both part of the glomerular tuft and Bowman's capsule, the latter forming an encompassing ring. The hyalinized arterioles are evident in images at the 40 µm and 60 µm level (blue arrow). The depth below the biopsy surface is labelled in top right of each image. Scale bar = 100 µm.

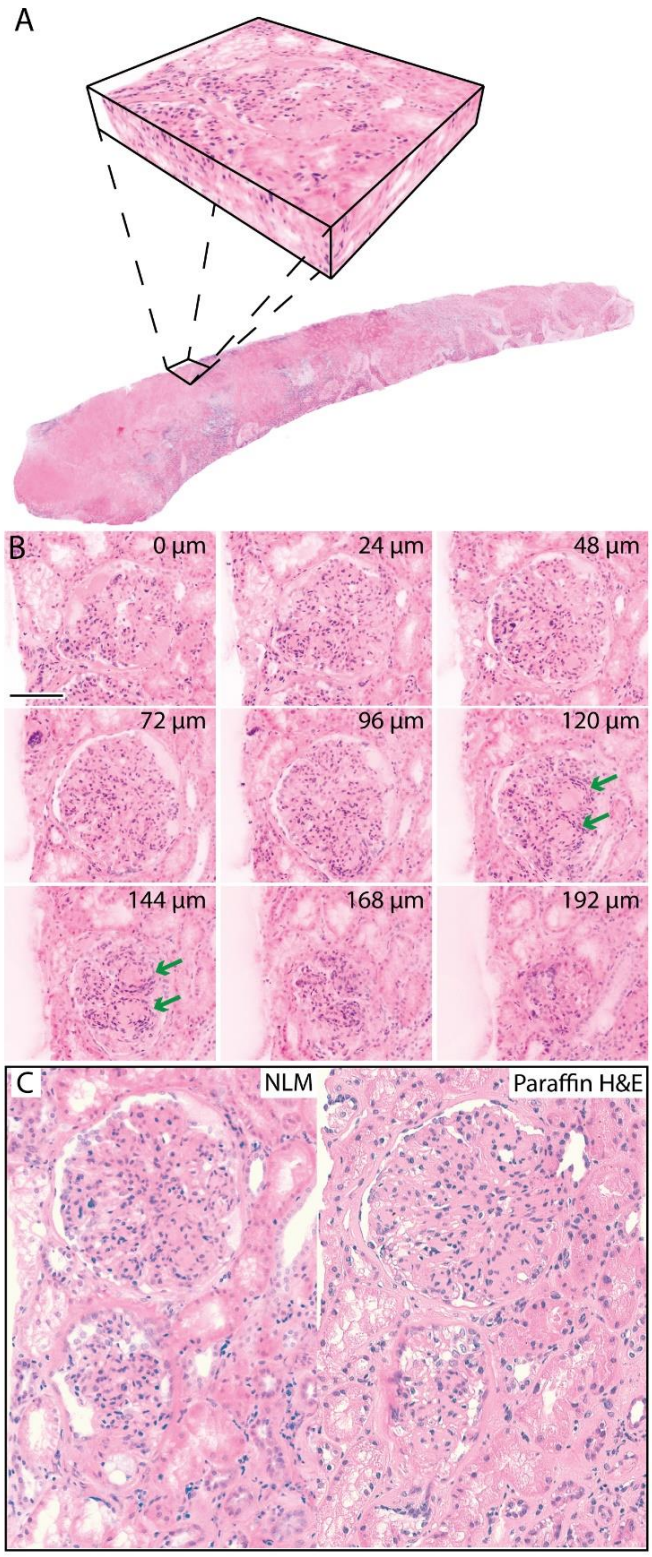

Figure 6.2. Three-dimensional NLM analysis of Biopsy 9 (diabetic nephropathy + IgA nephropathy). (**A**) NLM images of Biopsy 9 taken every 4 µm in depth through the biopsy and

reconstructed into a 3D volume. (**B**) NLM images selected at different levels of a glomerulus from Biopsy 9. The depth below the tissue surface is indicated in microns (top right). **(C)** An NLM image and corresponding paraffin H&E slide of Biopsy 9. Hypercellularity and mesangial expansion are evident in the NLM images and paraffin H&E slide, but the Kimmelstiel-Wilson nodules are only clearly defined at the NLM levels 120 µm and 144 µm (B, green arrow). Scale bar = 100 µm.

Focal and segmental glomerulosclerosis

NLM with optical clearing enabled 3D evaluation of focal lesions such as in biopsies with focal and segmental glomerulosclerosis (FSGS). NLM images selected at 12 µm intervals throughout a 3D volume of a glomerulus are shown in **Figure 6.3** and **Figure 6.4** (Biopsy 6). At the first level (0 µm) in **Figure 6.3**, the glomerular tuft is largely maintained but the left upper aspect is sclerotic (blue arrow). At deeper levels, it becomes more obvious that the tuft is adherent to Bowman's capsule which is accompanied by proliferation of Bowman's capsular cells and synechiae. At deeper levels, the vascular pole and macula densa become well delineated. The mesangial proliferation and matrix increase appear more evident in the area of the tuft with the segmental changes. The accompanying chronic inflammatory infiltrate is seen at all levels.

IgA Nephropathy

A biopsy from a patient with IgA nephropathy with crescentic lesions is shown in **Figure 6.5**. The crescent is seen in the NLM image extending into the proximal tubule. The crescent is global and associated with scattered neutrophils.

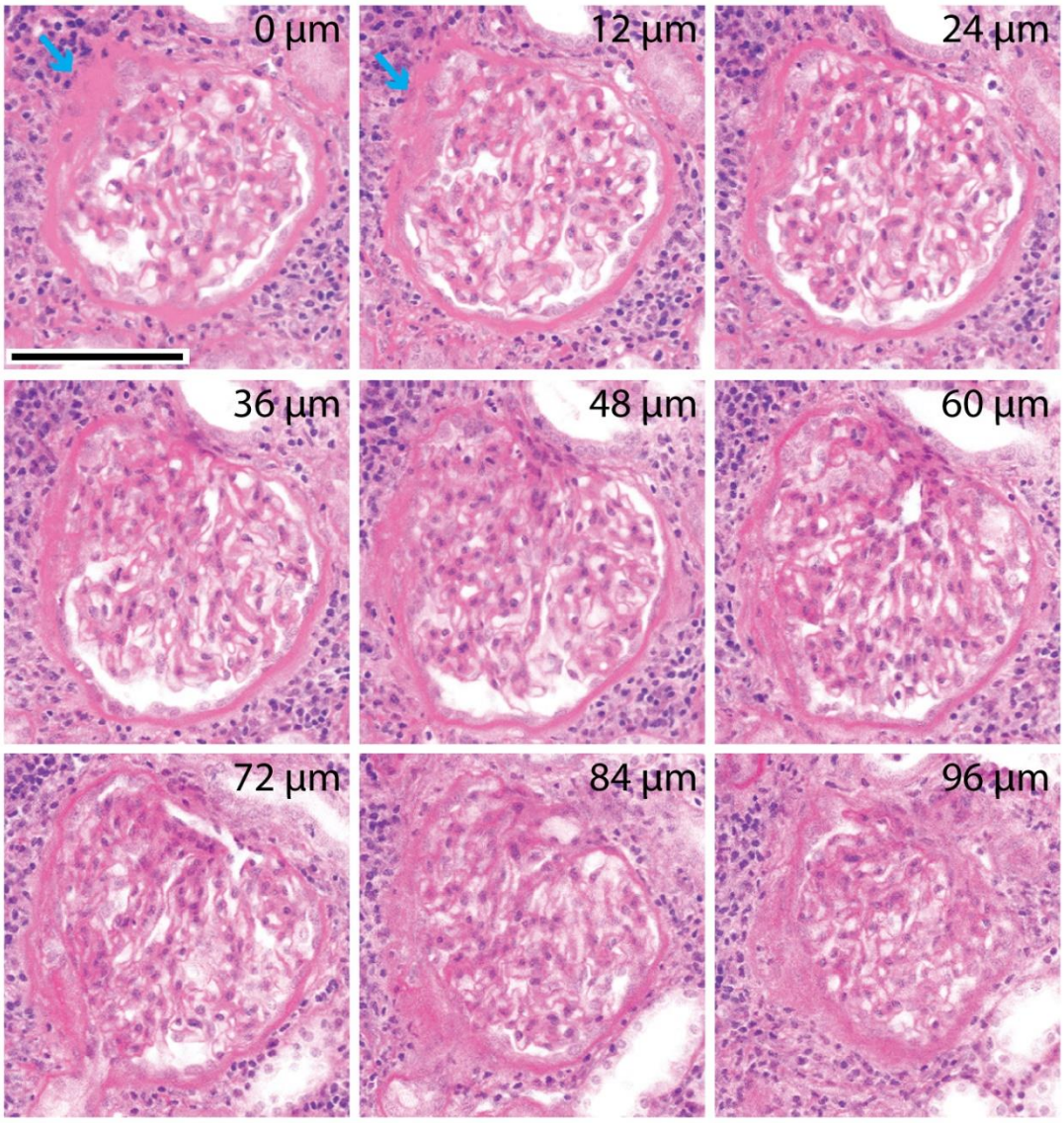

Figure 6.3. Focal and segmental glomerulosclerosis: Biopsy 6. NLM images of a patient with focal and segmental glomerulosclerosis (Biopsy 6) were acquired every 4 µm in depth. Images spaced 12 µm apart in depth show a segmental obliteration of the glomerular tuft with sclerosis (blue arrow), adhesions and obliteration of the urinary space. The relationship to the vascular pole is seen only in certain levels and an adhesion to the urinary pole is seen only in one image (at 72 µm depth). The depth below the tissue surface is indicated in microns (top right). Scale bar = 100 µm.

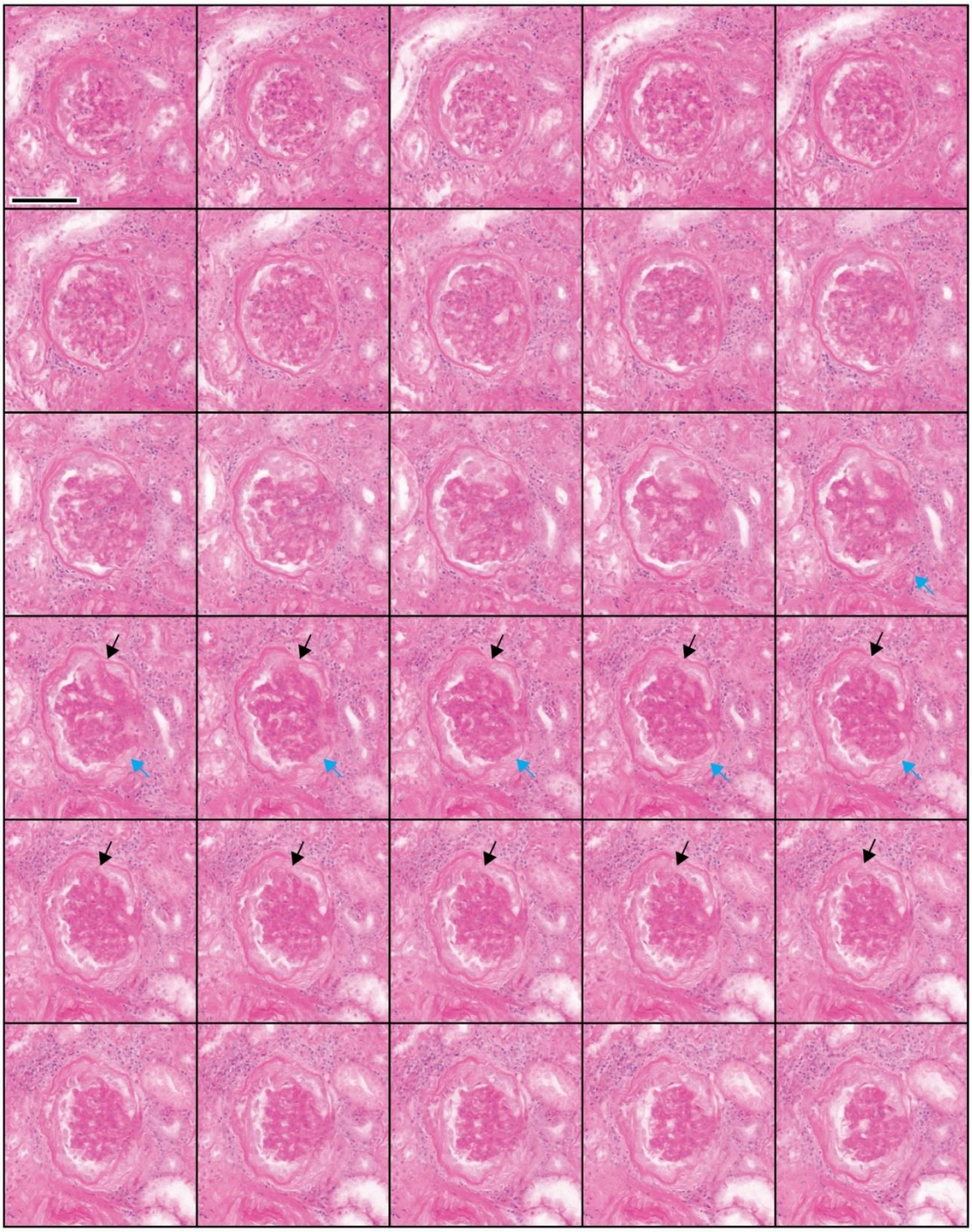

Figure 6.4. Three-dimensional NLM analysis of FSGS (Biopsy 6). NLM images spaced 4 µm in depth are shown (from left to right). Sections of glomerular collapse with associated epithelial proliferation and formation of synechia (black arrows) are seen. Fragmentation of Bowman's capsule at the vascular pole is seen (blue arrows) associated with epithelial proliferation. Scale bar = 100 µm.

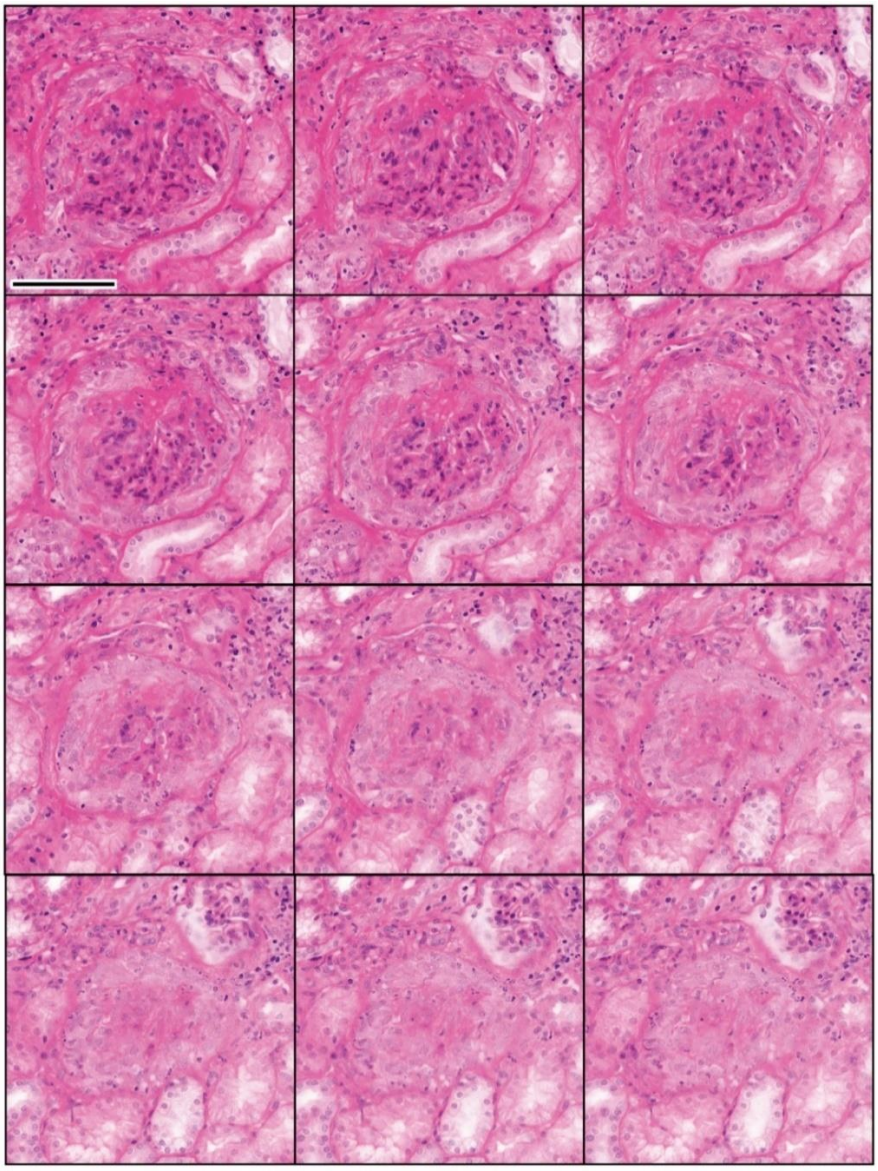

Figure 6.5. Three-dimensional NLM analysis of crescentic IgA nephropathy (Biopsy 8). NLM images spaced 4 µm in depth are shown (from left to right). In the first few images (upper left) the crescent extends into the proximal tubule. The crescent is global and associated with scattered neutrophils. Scale bar = 100 µm.

Acute tubular necrosis (acute kidney injury)

Acute tubular necrosis (ATN) can be visualized with NLM. **Figure 6.6** and **Figure 6.7** show granular debris in distal tubules and collecting ducts visualized with NLM. Neutrophils, necrosis, and oxalate are also apparent in 3D NLM images. Mitotic figures can be identified.

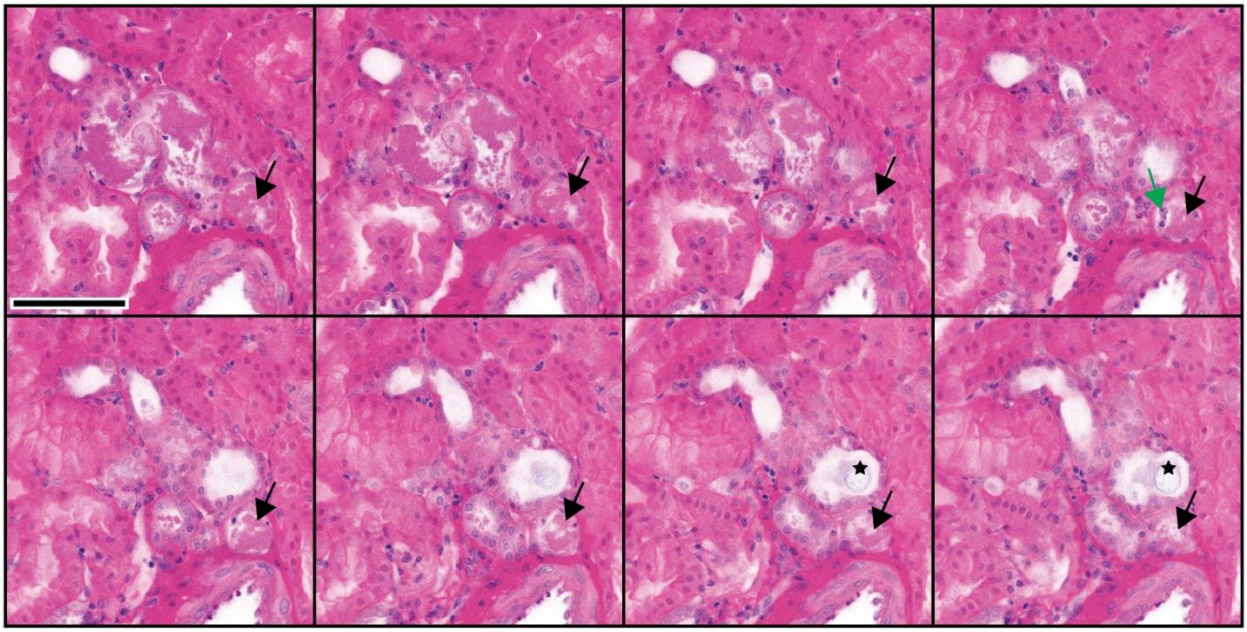

Figure 6.6. Three-dimensional NLM analysis of tubular necrosis (Biopsy 10) – part 1. NLM images spaced 4 µm in depth are shown (from left to right). Proximal tubules appear intact. Distal tubules with granular debris, oxalate (star), necrosis (black arrow), and neutrophils (green arrow) are seen. Scale bar = 100 µm.

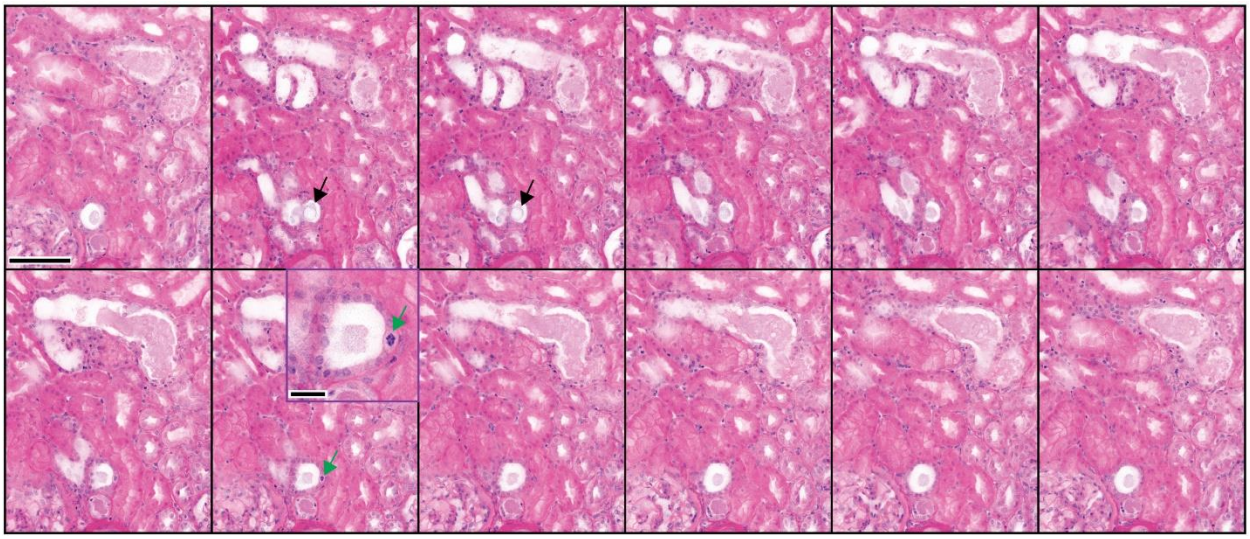

Figure 6.7. Three-dimensional NLM analysis of tubular necrosis (Biopsy 10) – part 2. NLM images spaced 4 µm in depth are shown (from left to right). Proximal tubules appear intact. Deeper cortex with collecting ducts filled with granular debris, in which cellular elements can be identified. Oxalate is seen in a distal tubule (black arrow). A mitotic figure can be identified (green arrow). Scale bar = 100 µm. Inset scale bar = 25 µm.

Quantitation

Glomeruli

Figure 6.8 compares the glomerular count from the 3D NLM volumes to the original paraffin histology. Note that the histology count was performed on the original histology slides while the NLM count was performed on tissue from the archival block. Furthermore, paraffin sections typically underestimate the glomerular count in renal biopsies.[137] The high glomerular count in the residual tissue indicates that archival blocks could be an important resource for retrospective studies.

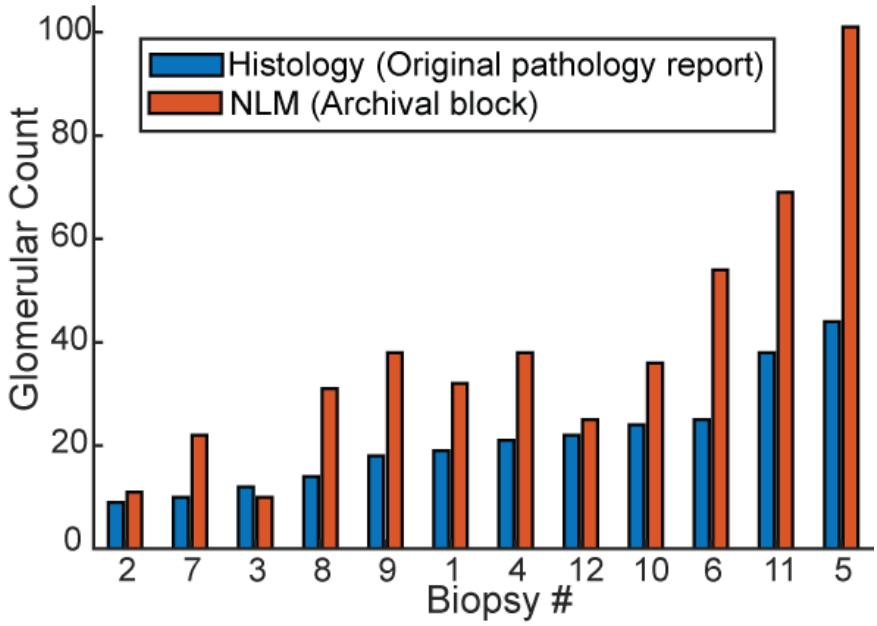

Figure 6.8. A plot of the glomerular count in the tissue analyzed using 3D NLM imaging versus the count on the original paraffin slides. Note that these counts were performed on different tissue from the same biopsy. The count on histology was performed on the original histology slides while the count on NLM was performed on the tissue from the archival block that was remaining after cutting the histology slides.

NLM analysis also enabled quantification that is difficult to perform with paraffin slides. For example, Biopsy 5 and 9 had mean glomerular diameters of 178.0 µm and 215.4 µm, respectively. The mean fraction of lesion volume (exudative lesions and Kimmelstiel-Wilson nodules) to glomerular volume was 0.229 in Biopsy 5 and 0.016 in Biopsy 9 (see **Figure 6.9**).

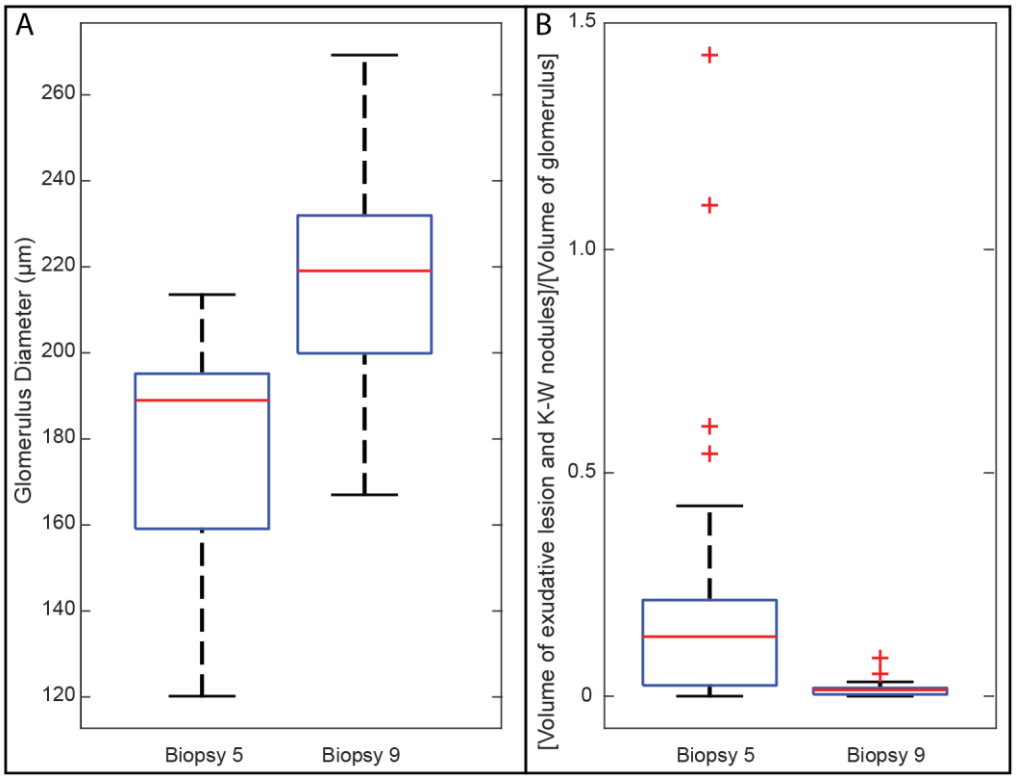

Figure 6.9. Box plot of glomerular diameters and lesional volumes in biopsies of patients with diabetic nephropathy. (**A**) The diameters of all glomeruli in biopsy 5 and 9 are shown. The mean glomerular diameters are 178.0 µm and 215.4 µm for biopsy 5 and 9 respectively. (**B**) The volume of exudative lesions and Kimmelstiel-Wilson nodules in each glomerulus as a fraction of the volume the glomerulus is shown. The mean fraction of lesion volume:glomerular volume was 0.229 and 0.016 in biopsy 5 and 9 respectively.

Tubulointerstitium

Figure 6.10 shows a 3D NLM volume of a renal biopsy from a patient with lithium nephropathy (Biopsy 12). The extent of parenchymal compromise is seen best in 3D. The cysts were segmented and the hypertrophic proximal tubules are seen as convoluted structures (blue and red box). Cysts could also be quantified and were measured to be 9.7% of total biopsy volume in

Biopsy 12. These measurements as well as spatial relationships within the glomeruli and biopsies could be readily obtained from 3D NLM volumes.

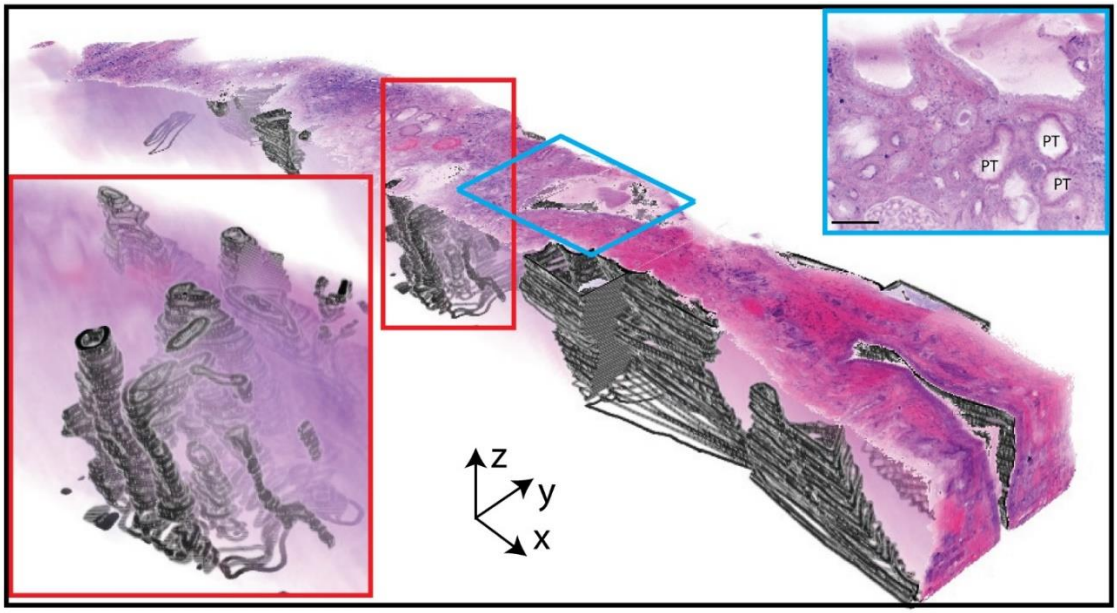

Figure 6.10. Three-dimensional NLM analysis of Biopsy 12 (lithium nephropathy). NLM images of Biopsy 12 taken every 4 µm in depth through the biopsy and reconstructed into a 3D volume. Individual cysts and tubules have been segmented in black and constitute 9.7% of the total biopsy volume. The 3D volume has been made partially transparent to visualize the segmented structures. A higher power view of the segmented tubules is shown in the red box. Hypertrophic proximal tubules (PT) are seen in the center and at higher power (blue box, 80 µm below biopsy surface, scale bar = 100 µm). Scale bar x, y, z = 100 µm.

Reversible processing

After tissue optical clearing and NLM imaging, biopsies could be declarified, re-embedded in paraffin, and processed for standard evaluation. NLM imaging with optical clearing did not alter standard tissue processing (**Figure 6.11**).

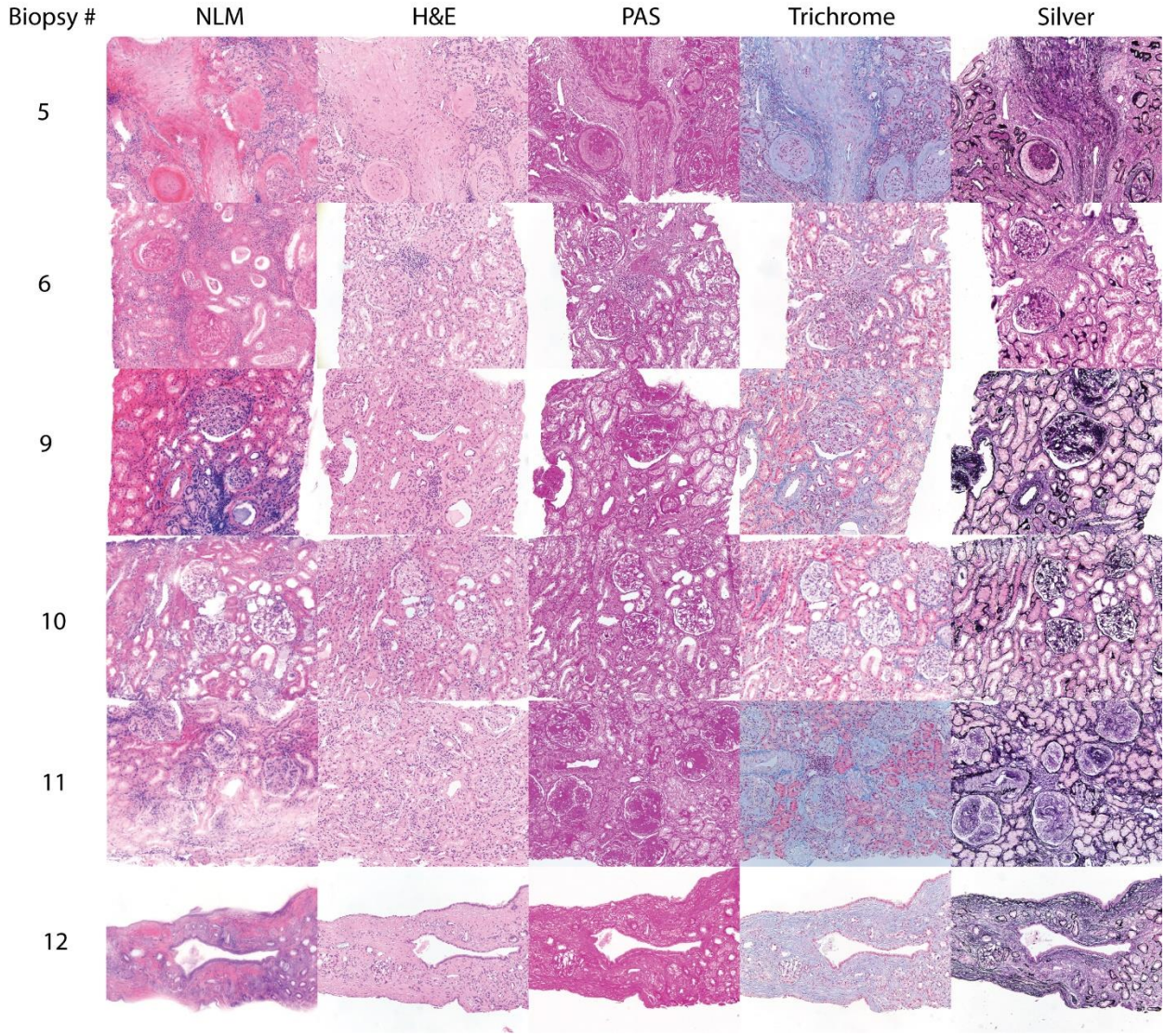

Figure 6.11. Histology of biopsies that were first optically cleared and evaluated with NLM. The first column shows NLM images from a biopsy that was optically cleared. After tissue optical clearing and NLM imaging, biopsies were declarified, re-embedded in paraffin, and processed for standard evaluation. H&E, PAS, Masson's trichrome, and Jones methenamine silver staining is not affected by prior NLM analysis.

6.4. DISCUSSION

In this study, we demonstrate an optical clearing, staining and 3D NLM imaging protocol for analysis of archival renal biopsies without microtome sectioning. The NLM images closely resemble paraffin H&E slides. Hypercellarity, mesangial expansion, hyalinized arterioles, and Kimmelsteil-Wilson nodules were clearly visualized in diabetic nephropathy. NLM enabled examination of segmental sclerosis, glomerular tuft adhesions, and mesangial proliferation in FSGS. Crescentic IgA nephropathy, oxalate, necrosis, and tubular granular debris in ATN, and large cysts in lithium nephrotoxicity are also apparent in NLM images.

There are differences between NLM images and paraffin H&E slides including decreased cell border sharpness, thicker appearing images, and variations in cytoplasmic color. In this initial study, the NLM images were acquired on thick tissue using a 20X, 1.0NA objective with a ~4 μm axial (z) resolution. Paraffin histology is typically cut at 2 μm and therefore NLM images appear thicker. Higher NA/power objectives can be used to provide higher resolution images at the cost of decreased imaging speed. Variations in cytoplasmic color likely result from differences in staining characteristics of Hoechst and Eosin versus Hematoxylin and Eosin. These differences are consistent across biopsies and patients and pathologists with experience and training may become comfortable interpreting these differences. Furthermore, standard paraffin evaluation can be performed in addition to NLM analysis.

In this chapter, we show that 3D NLM evaluation enables visualization and quantification of disease markers including sclerotic lesions, Kimmelstiel-Wilson nodules, mitotic figures, necrosis, glomerular collapse, and cystic changes. It is important to note that NLM evaluation is not meant to replace current standard-of-care tissue studies (PAS, Jones methenamine silver, Masson's Trichrome, immunofluorescence) but rather supplement them. NLM evaluation enables more

precise analysis of known diagnostic, therapeutic, and prognostic indicators. Larger studies will be required to investigate if NLM could provide additional insight into disease diagnosis, progression or treatment response.

Evaluating biopsies in 3D could be advantageous in many focal diseases. Differentiating between minimal change disease and FSGS is important for predicting therapeutic response and disease prognosis.[117] The more glomeruli that are evaluated in paraffin histology, the higher possibility that a glomerulus affected by FSGS will be found.[119,120] ANCA glomerulonephritis (GN), lupus nephritis, and diabetic nephropathy also often present with focal components of injury.[121,125]

There are several limitations to this study. This study has a small sample size and the biopsies analyzed represent a limited number of diseases. Larger studies will be required for further characterization of this technique. Furthermore, a limited number of known diagnostic and prognostic indicators were analyzed. The staining and imaging technique demonstrated in this chapter is limited to a nuclear and cytoplasmic/stromal fluorescent stain analogous to hematoxylin and eosin. Techniques that simulate stains such as PAS, Jones methenamine silver, and Masson's trichrome may improve the technique. However, as presented, this technique in not meant to replace standard tissue studies but augment them.

Previous studies have demonstrated analysis of needle biopsies from autopsy kidneys using NLM with similar clearing techniques.[48] The studies presented in this chapter extend these findings to demonstrate that archival tissue can be analyzed and that archival biopsies present a rich source of previously unanalyzed tissue. The techniques presented in this chapter may be more generally applicable to other organs and pathologies. Large stores of archival paraffin blocks are available

with comprehensive clinical data on outcomes in many diseases. Retrospective analysis of these specimens will be required to further assess the utility of NLM in biopsy analysis.

Chapter 7
Summary of thesis

In this thesis, we developed and validated new approaches for intraoperative and intraprocedural consultation with NLM.

In **Chapter 2**, we developed a rapid, robust fluorescent staining protocol using acridine orange and sulforhodamine 101 for NLM imaging. This protocol is compatible with 1030 nm excitation and therefore can be used with Ti:Sapphire lasers and compact, low cost ytterbium lasers. We validated this method by expert review of NLM images compared to formalin- fixed, paraffin-embedded (FFPE) H&E histology. Diagnostically important features such as normal terminal ductal lobular units, fibrous and adipose stromal parenchyma, inflammation, invasive carcinoma, and in situ lobular and ductal carcinoma were present in NLM images associated with pathologies identified on standard FFPE H&E histology. We demonstrated that acridine orange and sulforhodamine 101 were extracted to undetectable levels after FFPE processing and fluorescence in situ hybridization (FISH) HER2 amplification status was unaffected by the NLM imaging protocol. This method enables real-time histological guidance of surgical resections.

In **Chapter 3**, we developed technology and methods for a prospective 98 patient interventional randomized controlled trial at BIDMC on patients who will receive a lumpectomy for breast cancer. In this trial, a pathologist evaluates breast surgical margins with NLM intraoperatively to provide real-time feedback to the surgeon. The hypothesis is that NLM evaluation of surgical margins will reduce the rate of indication for repeat surgeries. Several patients who have participated in this study have been saved from repeat surgeries due to additional surgical resections, guided by NLM imaging. We are currently recruiting additional patients to

participate in this study at BIDMC. Full study results will be reported after the conclusion of the study.

In **Chapter 4**, we developed and characterized NLM for evaluation of prostatectomy tissue. A 3-pathologist blinded reading was conducted with 122 freshly excised prostate specimens from 40 patients undergoing radical prostatectomy. All pathologists achieved a 95% or greater sensitivity with 100% specificity for detecting cancer on NLM compared with FFPE H&E. Pooled sensitivity and specificity was 97.3% (93.7–99.1%; 95% confidence interval) and 100.0% (97.0–100.0%), respectively. Interobserver agreement for NLM reading had a Fleiss $\kappa = 0.95$. Differences between NLM images and FFPE H&E slides, including cytoplasmic color and stromal density, were observed, however NLM images could be interpreted with minimal training. NLM enabled visualization of benign, atrophic and hyperplastic glands and stroma, ejaculatory ducts, vasculature and inflammatory changes. NLM enabled identification of typical and variants of adenocarcinoma. Perineural invasion and extraprostatic extension could also be assessed. The high cancer detection accuracy and rapid specimen preparation suggest that NLM may be useful for intraoperative evaluation in radical prostatectomy.

In **Chapter 5**, we assessed the feasibility of rapid intraprocedural biopsy analysis using NLM. A total of 170 biopsies were collected from 63 patients who underwent targeted in-bore MRI or MRI-ultrasound fusion biopsy. Genitourinary pathologists evaluated the biopsies on an NLM instrument in real time then subsequently by FFPE histology and diagnoses were compared. Pathologists achieved a 92.4% sensitivity (85.0-96.9%, 95% confidence intervals) and 100.0% specificity (94.3-100.0%) for detecting carcinoma compared to FFPE histology. The agreement between the Grade Group determined by NLM versus FFPE histology had an unweighted Cohen's Kappa of 0.588. The average NLM evaluation time was 2.10 minutes per biopsy (3.08 minutes for

the first 20 patients, decreasing to 1.54 minutes in subsequent patients). NLM enabled rapid evaluation of prostate biopsies, making it a promising technique to improve biopsy procedures and patient care.

In **Chapter 6**, we developed staining and optical clearing techniques for rapid three-dimensional analysis of renal biopsies. Archival renal paraffin blocks from 12 patients were deparaffinized and stained with Hoechst and Eosin for fluorescent nuclear and cytoplasmic/stromal contrast, then optically cleared using benzyl alcohol benzyl benzoate (BABB). 3D NLM images of entire biopsy fragments were acquired using NLM. Cysts, glomeruli, exudative lesions, and Kimmelstiel-Wilson nodules were segmented in 3D and their volumes, diameters, and percent composition could be easily obtained. Rapid optical clearing and NLM imaging enables more thorough biopsy examination and is a promising technique for analysis of archival paraffin blocks.

Rapid imaging of surgical and biopsy tissue with NLM is not limited to the applications investigated here. Taken together, the NLM imaging technology and evaluation methods developed in this thesis may more generally enable more accurate, faster, and simplified surgeries and clinical procedures.

References

1. Kumar V, Abbas AK, Aster JC. *Robbins and Cotran Pathologic Basis of Disease*. 9th ed. Elsevier/Saunders; 2015.

2. Novis D, Zarbo R. Interinstitutional comparison of frozen section turnaround time - A College of American Pathologists Q-probes study of 32,868 frozen sections in 700 hospitals. *Arch Pathol Lab Med*. 1997;121(6):559-567.

3. Bancroft J, Gamble M. *Theory and Practice of Histological Techniques*. 6th ed. Churchill Livingstone/Elsevier; 2008.

4. Denk W, Strickler J, Webb W. Two-photon laser scanning fluorescence microscopy. *Science (80-)*. 1990;248(4951):73-76.

5. Xu C, Webb WW. Measurement of two-photon excitation cross sections of molecular fluorophores with data from 690 to 1050 nm. *J Opt Soc Am B*. 1996;13(3):481.

6. Giacomelli MG, Husvogt L, Vardeh H, Faulkner-Jones BE, Hornegger J, Connolly JL, Fujimoto JG. Virtual Hematoxylin and Eosin Transillumination Microscopy Using Epi-Fluorescence Imaging. *PLoS One*. 2016;11(8):e0159337.

7. Cahill LC, Fujimoto JG, Giacomelli MG, Yoshitake T, Wu Y, Lin DI, Ye H, Carrasco-Zevallos OM, Wagner AA, Rosen S. Comparing histologic evaluation of prostate tissue using nonlinear microscopy and paraffin H&E: a pilot study. *Mod Pathol*. 2019;32(8):1158-1167.

8. Cahill LC, Giacomelli MG, Yoshitake T, Vardeh H, Faulkner-Jones BE, Connolly JL, Sun C-K, Fujimoto JG. Rapid virtual hematoxylin and eosin histology of breast tissue specimens

using a compact fluorescence nonlinear microscope. *Lab Investig*. 2018;98(1):150-160.

9. Wang M, Kimbrell HZ, Sholl AB, Tulman DB, Elfer KN, Schlichenmeyer TC, Lee BR, Lacey M, Brown JQ. High-Resolution Rapid Diagnostic Imaging of Whole Prostate Biopsies Using Video-Rate Fluorescence Structured Illumination Microscopy. *Cancer Res*. 2015;75(19):4032-4041.

10. Wang M, Tulman DB, Sholl AB, Kimbrell HZ, Mandava SH, Elfer KN, Luethy S, Maddox MM, Lai W, Lee BR, Brown JQ. Gigapixel surface imaging of radical prostatectomy specimens for comprehensive detection of cancer-positive surgical margins using structured illumination microscopy. *Sci Rep*. 2016;6(May):27419.

11. Fereidouni F, Harmany ZT, Tian M, Todd A, Kintner JA, McPherson JD, Borowsky AD, Bishop J, Lechpammer M, Demos SG, Levenson RM. Microscopy with ultraviolet surface excitation for rapid slide-free histology. *Nat Biomed Eng*. 2017;1(12):957-966.

12. Glaser AK, Reder NP, Chen Y, McCarty EF, Yin C, Wei L, Wang Y, True LD, Liu JTC. Light-sheet microscopy for slide-free non-destructive pathology of large clinical specimens. *Nat Biomed Eng*. 2017;1(7):0084.

13. Puliatti S, Bertoni L, Pirola GM, Azzoni P, Bevilacqua L, Eissa A, Elsherbiny A, Sighinolfi MC, Chester J, Kaleci S, Rocco B, Micali S, Bagni I, Bonetti LR, Maiorana A, Malvehy J, Longo C, Montironi R, Bianchi G, Pellacani G. Ex vivo fluorescence confocal microscopy: the first application for real-time pathological examination of prostatic tissue. *BJU Int*. 2019;124(3):469-476.

14. Giacomelli MG, Yoshitake T, Cahill LC, Vardeh H, Quintana LM, Faulkner-Jones BE, Brooker J, Connolly JL, Fujimoto JG. Multiscale nonlinear microscopy and widefield white

light imaging enables rapid histological imaging of surgical specimen margins. *Biomed Opt Express*. 2018;9(5):2457.

15. Yoshitake T, Giacomelli MG, Quintana LM, Vardeh H, Cahill LC, Faulkner-Jones BE, Connolly JL, Do D, Fujimoto JG. Rapid histopathological imaging of skin and breast cancer surgical specimens using immersion microscopy with ultraviolet surface excitation. *Sci Rep*. 2018;8(1):4476.

16. Zynger DL, Parwanit A. *Prostate Pathology*. (Suster S, ed.). Demos Medical Publishing; 2014.

17. Humphrey PA. *Prostate Pathology*. American Society for Clinical Pathology; 2003.

18. Epstein JI, Netto GJ. *Biopsy Interpretation of the Prostate*. Wolters Kluwer Health; 2014.

19. Tao YK, Shen D, Sheikine Y, Ahsen OO, Wang HH, Schmolze DB, Johnson NB, Brooker JS, Cable AE, Connolly JL, Fujimoto JG. Assessment of breast pathologies using nonlinear microscopy. *Proc Natl Acad Sci*. 2014;111(43):15304-15309.

20. Fujimoto JG, Giacomelli MG, Yoshitake T, Cahill LC. Method and apparatus for imaging unsectioned tissue specimens. Published online 2019:US Patent US20190377170A1.

21. American College Of Radiology. Practice guideline for the management of ductal carcinoma in-situ of the breast (DCIS). *J Am Coll Surg*. 2007;205(1):145-161.

22. American College of Radiology. Practice Guideline for the Breast Conservation Therapy in the Management of Invasive Breast Carcinoma. *J Am Coll Surg*. 2007;205(2):362-376.e2.

23. Sabel MS, Rogers K, Griffith K, Jagsi R, Kleer CG, Diehl KA, Breslin TM, Cimmino VM, Chang AE, Newman LA. Residual disease after re-excision lumpectomy for close margins.

J Surg Oncol. 2009;99(2):99-103.

24. Kobbermann A, Unzeitig A, Xie X-J, Yan J, Euhus D, Peng Y, Sarode V, Moldrem A, Marilyn Leitch A, Andrews V, Stallings C, Rao R. Impact of Routine Cavity Shave Margins on Breast Cancer Re-excision Rates. *Ann Surg Oncol*. 2011;18(5):1349-1355.

25. Morrow M, Jagsi R, Alderman AK, Griggs JJ, Hawley ST, Hamilton AS, Graff JJ, Katz SJ. Surgeon Recommendations and Receipt of Mastectomy for Treatment of Breast Cancer. *JAMA*. 2009;302(14):1551-1556.

26. McCahill LE, Single RM, Aiello Bowles EJ, Feigelson HS, James TA, Barney T, Engel JM, Onitilo AA. Variability in Reexcision Following Breast Conservation Surgery. *JAMA*. 2012;307(5):467-475.

27. Fleming FJ, Hill ADK, Mc Dermott EW, O'Doherty A, O'Higgins NJ, Quinn CM. Intraoperative margin assessment and re-excision rate in breast conserving surgery. *Eur J Surg Oncol*. 2004;30(3):233-237.

28. Huston TL, Pigalarga R, Osborne MP, Tousimis E. The influence of additional surgical margins on the total specimen volume excised and the reoperative rate after breast-conserving surgery. *Am J Surg*. 2006;192(4):509-512.

29. Ferreiro J, Gisvold J, Bostwick D. Accuracy of frozen-section diagnosis of mammographically directed breast biopsies. Results of 1,490 consecutive cases. *Am J Surg Pathol*. 1995;19(11):1267-1271.

30. Menes TS, Tartter PI, Mizrachi H, Smith SR, Estabrook A. Touch Preparation or Frozen Section for Intraoperative Detection of Sentinel Lymph Node Metastases From Breast

Cancer. *Ann Surg Oncol*. 2003;10(10):1166-1170.

31. Allen TC. The Incredible Shrinking Billing Codes. *Arch Pathol Lab Med*. 2014;138(5):593-594.

32. Boppart SA, Richards-Kortum R. Point-of-care and point-of-procedure optical imaging technologies for primary care and global health. *Sci Transl Med*. 2014;6(253):253rv2-253rv2.

33. Leigh SY, Liu JTC. Multi-color miniature dual-axis confocal microscope for point-of-care pathology. *Opt Lett*. 2012;37(12):2430-2432.

34. Bini J, Spain J, Nehal K, Hazelwood V, DiMarzio C, Rajadhyaksha M. Confocal mosaicing microscopy of human skin ex vivo: spectral analysis for digital staining to simulate histology-like appearance. *J Biomed Opt*. 2011;16(7):076008.

35. Chung VQ, Dwyer PJ, Nehal KS, Rajadhyaksha M, Menaker GM, Charles C, Jiang SB. Use of Ex Vivo Confocal Scanning Laser Microscopy during Mohs Surgery for Nonmelanoma Skin Cancers. *Dermatologic Surg*. 2004;30(12p1):1470-1478.

36. Gareau DS, Karen JK, Dusza SW, Tudisco M, Nehal KS, Rajadhyaksha M. Sensitivity and specificity for detecting basal cell carcinomas in Mohs excisions with confocal fluorescence mosaicing microscopy. *J Biomed Opt*. 2009;14(3):34012-34017.

37. Yoshitake T, Giacomelli MG, Cahill LC, Schmolze DB, Vardeh H, Faulkner-Jones BE, Connolly JL, Fujimoto JG. Direct comparison between confocal and multiphoton microscopy for rapid histopathological evaluation of unfixed human breast tissue. *J Biomed Opt*. 2016;21(12):126021.

38. Fu HL, Mueller JL, Javid MP, Mito JK, Kirsch DG, Ramanujam N, Brown JQ. Optimization of a Widefield Structured Illumination Microscope for Non-Destructive Assessment and Quantification of Nuclear Features in Tumor Margins of a Primary Mouse Model of Sarcoma. Brody JP, ed. *PLoS One*. 2013;8(7):e68868.

39. Schlichenmeyer TC, Wang M, Elfer KN, Brown JQ. Video-rate structured illumination microscopy for high-throughput imaging of large tissue areas. *Biomed Opt Express*. 2014;5(2):366-377.

40. Orringer DA, Pandian B, Niknafs YS, Hollon TC, Boyle J, Lewis S, Garrard M, Hervey-Jumper SL, Garton HJL, Maher CO, Heth JA, Sagher O, Wilkinson DA, Snuderl M, Venneti S, Ramkissoon SH, McFadden KA, Fisher-Hubbard A, Lieberman AP, Johnson TD, Xie XS, Trautman JK, Freudiger CW, Camelo-Piragua S. Rapid intraoperative histology of unprocessed surgical specimens via fibre-laser-based stimulated Raman scattering microscopy. *Nat Biomed Eng*. 2017;1(February):0027.

41. Tu H, Liu Y, Turchinovich D, Marjanovic M, Lyngsø JK, Lægsgaard J, Chaney EJ, Zhao Y, You S, Wilson WL, Xu B, Dantus M, Boppart SA. Stain-free histopathology by programmable supercontinuum pulses. *Nat Photonics*. 2016;10(8):534-540.

42. Szu-Yu Chen, Shee-Uan Chen, Hai-Yin Wu, Wen-Jeng Lee, Yi-Hua Liao, Chi-Kuang Sun. In Vivo Virtual Biopsy of Human Skin by Using Noninvasive Higher Harmonic Generation Microscopy. *IEEE J Sel Top Quantum Electron*. 2010;16(3):478-492.

43. Tang S, Liu J, Krasieva TB, Chen Z, Tromberg BJ. Developing compact multiphoton systems using femtosecond fiber lasers. *J Biomed Opt*. 2009;14(3):030508.

44. Millard AC, Wiseman PW, Fittinghoff DN, Wilson KR, Squier JA, Müller M. Third-

harmonic generation microscopy by use of a compact, femtosecond fiber laser source. *Appl Opt*. 1999;38(36):7393.

45. Jacques SL. Optical properties of biological tissues: a review. *Phys Med Biol*. 2013;58(14):5007-5008.

46. Balu M, Saytashev I, Hou J, Dantus M, Tromberg BJ. Sub-40 fs, 1060-nm Yb-fiber laser enhances penetration depth in nonlinear optical microscopy of human skin. *J Biomed Opt*. 2015;20(12):120501.

47. Kobat D, Durst ME, Nishimura N, Wong AW, Schaffer CB, Xu C. Deep tissue multiphoton microscopy using longer wavelength excitation. *Opt Express*. 2009;17(16):13354.

48. Olson E, Levene MJ, Torres R. Multiphoton microscopy with clearing for three dimensional histology of kidney biopsies. *Biomed Opt Express*. 2016;7(8):3089.

49. Ragazzi M, Piana S, Longo C, Castagnetti F, Foroni M, Ferrari G, Gardini G, Pellacani G. Fluorescence confocal microscopy for pathologists. *Mod Pathol*. 2013;27(3):1-12.

50. Gareau D, Bar A, Snaveley N, Lee K, Chen N, Swanson N, Simpson E, Jacques S. Tri-modal confocal mosaics detect residual invasive squamous cell carcinoma in Mohs surgical excisions. *J Biomed Opt*. 2012;17(6):066018.

51. Robertson T, Bunel F, Roberts M. Fluorescein Derivatives in Intravital Fluorescence Imaging. *Cells*. 2013;2(3):591-606.

52. Li CI, Uribe DJ, Daling JR. Clinical characteristics of different histologic types of breast cancer. *Br J Cancer*. 2005;93(9):1046-1052.

53. Li CI, Malone KE, Porter PL, Weiss NS, Tang M-TC, Cushing-Haugen KL, Daling JR.

Relationship Between Long Durations and Different Regimens of Hormone Therapy and Risk of Breast Cancer. *JAMA*. 2003;289(24):3254-3263.

54. Giacomelli MG, Yoshitake T, Husvogt L, Cahill L, Ahsen O, Vardeh H, Sheykin Y, Faulkner-Jones BE, Hornegger J, Brooker J, Cable A, Connolly JL, Fujimoto JG. Design of a portable wide field of view GPU-accelerated multiphoton imaging system for real-time imaging of breast surgical specimens. In: Periasamy A, So PTC, König K, eds. *Progress in Biomedical Optics and Imaging - Proceedings of SPIE*. Vol 9712. ; 2016:97121G.

55. Zheng Z, Yabroff KR, Guy GP, Han X, Li C, Banegas MP, Ekwueme DU, Jemal A. Annual Medical Expenditure and Productivity Loss Among Colorectal, Female Breast, and Prostate Cancer Survivors in the United States. *J Natl Cancer Inst*. 2016;108(5):djv382.

56. Metcalfe LN, Zysk AM, Edelman G, Vu L, Cittadine AJ, Hyer KB, Thompson AM. Beyond the margins: Economic costs and complication rates associated with repeated breast-conserving surgeries. In: *J. Clin. Oncol. 34*. ; 2016:suppl 1050.

57. Uecker JM, Bui EH, Foulkrod KH, Sabra JP. Intraoperative assessment of breast cancer specimens decreases cost and number of reoperations. *Am Surg*. 2011;77(3):342-344.

58. Chien AT, Rosenthal MB. Medicare's Physician Value-Based Payment Modifier — Will the Tectonic Shift Create Waves? *N Engl J Med*. 2013;369(22):2076-2078.

59. Siegel RL, Miller KD, Fuchs HE, Jemal A. Cancer Statistics, 2021. *CA Cancer J Clin*. 2021;71(1):7-33.

60. Bill-Axelson A, Holmberg L, Garmo H, Taari K, Busch C, Nordling S, Häggman M, Andersson S-O, Andrén O, Steineck G, Adami H-O, Johansson J-E. Radical Prostatectomy

or Watchful Waiting in Prostate Cancer — 29-Year Follow-up. *N Engl J Med*. 2018;379(24):2319-2329.

61. Dell'Oglio P, Karnes RJ, Joniau S, Spahn M, Gontero P, Tosco L, Fossati N, Kneitz B, Chlosta P, Graefen M, Marchioro G, Bianchi M, Sanchez-Salas R, Karakiewicz PI, Poppel H Van, Montorsi F, Briganti A. Very long-term survival patterns of young patients treated with radical prostatectomy for high-risk prostate cancer. *Urol Oncol Semin Orig Investig*. 2016;34(5):234.e13-234.e19.

62. Hamilton ZA, Kane CJ. Nerve-sparing Technique During Radical Prostatectomy and its Effect on Urinary Continence. *Eur Urol*. 2016;69(4):590-591.

63. Michl U, Tennstedt P, Feldmeier L, Mandel P, Oh SJ, Ahyai S, Budäus L, Chun FKH, Haese A, Heinzer H, Salomon G, Schlomm T, Steuber T, Huland H, Graefen M, Tilki D. Nerve-sparing surgery technique, not the preservation of the neurovascular bundles, leads to improved long-term continence rates after radical prostatectomy. *Eur Urol*. 2016;69(4):584-589.

64. Bianco FJ, Scardino PT, Eastham JA. Radical prostatectomy: Long-term cancer control and recovery of sexual and urinary function ("trifecta"). *Urology*. 2005;66(5 SUPPL.):83-94.

65. Sacco E, Prayer-Galetti T, Pinto F, Fracalanza S, Betto G, Pagano F, Artibani W. Urinary incontinence after radical prostatectomy: incidence by definition, risk factors and temporal trend in a large series with a long-term follow-up. *BJU Int*. 2006;97(6):1234-1241.

66. Catalona WJ, Carvalhal GF, Mager DE, Smith DS. Potency, continence and complication rates in 1,870 consecutive radical retropubic prostatectomies. *J Urol*. 1999;162(2):433-438.

67. Sanda MG, Dunn RL, Michalski J, Sandler HM, Northouse L, Hembroff L, Lin X, Greenfield TK, Litwin MS, Saigal CS, Mahadevan A, Klein E, Kibel A, Pisters LL, Kuban D, Kaplan I, Wood D, Ciezki J, Shah N, Wei JT. Quality of Life and Satisfaction with Outcome among Prostate-Cancer Survivors. *N Engl J Med*. 2008;358(12):1250-1261.

68. Quinlan DM, Epstein JI, Carter BS, Walsh PC. Sexual Function following Radical Prostatectomy: Influence of Preservation of Neurovascular Bundles. *J Urol*. 1991;145(5):998-1002.

69. Rabbani F, Stapleton AMF, Kattan MW, Wheeler TM, Scardino PT. Factors predicting recovery of erections after radical prostatectomy. *J Urol*. 2000;164(6):1929-1934.

70. Kundu SD, Roehl KA, Eggener SE, Antenor JA V., Han M, Catalona WJ. Potency, continence and complications in 3,477 consecutive radical retropubic prostatectomies. *J Urol*. 2004;172(6 I):2227-2231.

71. Budäus L, Isbarn H, Schlomm T, Heinzer H, Haese A, Steuber T, Salomon G, Huland H, Graefen M. Current Technique of Open Intrafascial Nerve-Sparing Retropubic Prostatectomy. *Eur Urol*. 2009;56(2):317-324.

72. Ohori M, Kattan MiW, Koh H, Maru N, Slawin KM, Shariat S, Muramoto M, Reuter VE, Wheeler TM, Scardino PT. Predicting the Presence and Side of Extracapsular Extension: A Nomogram for Staging Prostate Cancer. *J Urol*. 2004;171(5):1844-1849.

73. Steuber T, Graefen M, Haese A, Erbersdobler A, Chun FK-H, Schlom T, Perrotte P, Huland H, Karakiewicz PI. Validation of a Nomogram for Prediction of Side Specific Extracapsular Extension at Radical Prostatectomy. *J Urol*. 2006;175(3):939-944.

74. Partin AW, Kattan MW, Subong EN, Walsh PC, Wojno KJ, Oesterling JE, Scardino PT, Pearson JD. Combination of prostate-specific antigen, clinical stage, and Gleason score to predict pathological stage of localized prostate cancer. A multi-institutional update. *JAMA*. 1997;277(18):1445-1451.

75. Augustin H, Eggert T, Wenske S, Karakiewicz PI, Palisaar J, Daghofer F, Huland H, Graefen M. Comparison of accuracy between the Partin tables of 1997 and 2001 to predict final pathological stage in clinically localized prostate cancer. *J Urol*. 2004;171(1):177-181.

76. Schlomm T, Tennstedt P, Huxhold C, Steuber T, Salomon G, Michl U, Heinzer H, Hansen J, Budäus L, Steurer S, Wittmer C, Minner S, Haese A, Sauter G, Graefen M, Huland H. Neurovascular Structure-adjacent Frozen-section Examination (NeuroSAFE) Increases Nerve-sparing Frequency and Reduces Positive Surgical Margins in Open and Robot-assisted Laparoscopic Radical Prostatectomy: Experience After 11 069 Consecutive Patients. *Eur Urol*. 2012;62(2):333-340.

77. von Bodman C, Brock M, Roghmann F, Byers A, Löppenberg B, Braun K, Pastor J, Sommerer F, Noldus J, Palisaar RJ. Intraoperative Frozen Section of the Prostate Decreases Positive Margin Rate While Ensuring Nerve Sparing Procedure During Radical Prostatectomy. *J Urol*. 2013;190(2):515-520.

78. Vasdev N, Agarwal S, Rai BP, Soosainathan A, Shaw G, Chang S, Prasad V, Mohan-S G, Adshead JM. Intraoperative Frozen Section of the Prostate Reduces the Risk of Positive Margin Whilst Ensuring Nerve Sparing in Patients with Intermediate and High-Risk Prostate Cancer Undergoing Robotic Radical Prostatectomy: First Reported UK Series. *Curr Urol*. 2016;9(2):93-103.

79. Rais-Bahrami S, Levinson AW, Fried NM, Lagoda GA, Hristov A, Chuang Y, Burnett AL, Su LM. Optical Coherence Tomography of Cavernous Nerves: A Step Toward Real-Time Intraoperative Imaging During Nerve-Sparing Radical Prostatectomy. *Urology*. 2008;72(1):198-204.

80. Fried NM, Rais-Bahrami S, Lagoda GA, Chuang AY, Su LM, Burnett AL. Identification and imaging of the nerves responsible for erectile function in rat prostate, in vivo, using optical nerve stimulation and optical coherence tomography. *IEEE J Sel Top Quantum Electron*. 2007;13(6):1641-1645.

81. Aron M, Kaouk JH, Hegarty NJ, Colombo, Jr. JR, Haber G-P, Chung BI, Zhou M, Gill IS. Second Prize: Preliminary Experience with the Niris ™ Optical Coherence Tomography System during Laparoscopic and Robotic Prostatectomy. *J Endourol*. 2007;21(8):814-818.

82. D'Amico a V, Weinstein M, Li X, Richie JP, Fujimoto J. Optical coherence tomography as a method for identifying benign and malignant microscopic structures in the prostate gland. *Urology*. 2000;55(5):783-787.

83. Periasamy A, Skoglund P, Noakes C, Keller R. An Evaluation of Two-Photon Excitation Versus Confocal and Digital Deconvolution Fluorescence Microscopy Imaging in Xenopus Morphogenesis. 1999;181(July):172-181.

84. Helmchen F, Denk W. Deep tissue two-photon microscopy. *Nature*. 2005;2(12):932-940.

85. Yadav R, Mukherjee S, Hermen M, Tan G, Maxfield FR, Webb WW, Tewari AK. Multiphoton Microscopy of Prostate and Periprostatic Neural Tissue: A Promising Imaging Technique for Improving Nerve-Sparing Prostatectomy. *J Endourol*. 2009;23(5):861-867.

86. Durand M, Jain M, Aggarwal A, Robinson BD, Srivastava A, Smith R, Sooriakumaran P, Loeffler J, Pumill C, Amiel J, Chevallier D, Mukherjee S, Tewari AK. Real-time in vivo periprostatic nerve tracking using multiphoton microscopy in a rat survival surgery model: A promising pre-clinical study for enhanced nerve-sparing surgery. *BJU Int*. 2015;116(3):478-486.

87. Tewari AK, Shevchuk MM, Sterling J, Grover S, Herman M, Yadav R, Mudalair K, Srivastava A, Rubin MA, Zipfel WR, Maxfield FR, Xu C, Webb WW, Mukherjee S. Multiphoton microscopy for structure identification in human prostate and periprostatic tissue: implications in prostate cancer surgery. *BJU Int*. 2011;108(9):1421-1429.

88. Cahill LC, Wu Y, Yoshitake T, Ponchiardi C, Giacomelli MG, Wagner AA, Rosen S, Fujimoto JG. Nonlinear microscopy for detection of prostate cancer: analysis of sensitivity and specificity in radical prostatectomies. *Mod Pathol*. 2020;33(5):916-923.

89. Yossepowitch O, Briganti A, Eastham JA, Epstein J, Graefen M, Montironi R, Touijer K. Positive surgical margins after radical prostatectomy: A systematic review and contemporary update. *Eur Urol*. 2014;65(2):303-313.

90. Gillitzer R, Thuroff C, Fandel T, Thomas C, Thuroff JW, Brenner W, Wiesner C, Jones J, Hansen T, Hampel C. Intraoperative peripheral frozen sections do not significantly affect prognosis after nerve-sparing radical prostatectomy for prostate cancer. *BJU Int*. 2011;107(5):755-759.

91. Beyer B, Schlomm T, Tennstedt P, Boehm K, Adam M, Schiffmann J, Sauter G, Wittmer C, Steuber T, Graefen M, Huland H, Haese A. A feasible and time-efficient adaptation of NeuroSAFE for da Vinci robot-assisted radical prostatectomy. *Eur Urol*. 2014;66(1):138-

144.

92. Lepor H, Kaci L. Role of intraoperative biopsies during radical retropubic prostatectomy. *Urology*. 2004;63(3):499-502.

93. Heinrich E, Schön G, Schiefelbein F, Michel MS, Trojan L. Clinical impact of intraoperative frozen sections during nerve-sparing radical prostatectomy. *World J Urol*. 2010;28(6):709-713.

94. Nunez AL, Giannico GA, Mukhtar F, Dailey V, El-Galley R, Hameed O. Frozen section evaluation of margins in radical prostatectomy specimens: A contemporary study and literature review. *Ann Diagn Pathol*. 2016;24:11-18.

95. Preisser F, Theissen L, Wild P, Bartelt K, Kluth L, Köllermann J, Graefen M, Steuber T, Huland H, Tilki D, Roos F, Becker A, Chun FKH, Mandel P. Implementation of Intraoperative Frozen Section During Radical Prostatectomy: Short-term Results from a German Tertiary-care Center. *Eur Urol Focus*. Published online March 2019.

96. Loeb S, Carter HB, Berndt SI, Ricker W, Schaeffer EM. Complications After Prostate Biopsy: Data From SEER-Medicare. *J Urol*. 2011;186(5):1830-1834.

97. Essink-Bot ML, De Koning HJ, Nijs HGT, Kirkels WJ, Van Der Maas PJ, Schröder FH. Short-term effects of population-based screening for prostate cancer on health-related quality of life. *J Natl Cancer Inst*. 1998;90(12):925-931.

98. Gustafsson O, Theorell T, Norming U, Perski A, Öhström M, Nyman C. Psychological reactions in men screened for prostate cancer. *Br J Urol*. 1995;75(5):631-636.

99. Welch HG, Fisher ES, Gottlieb DJ, Barry MJ. Detection of Prostate Cancer via Biopsy in

the Medicare-SEER Population During the PSA Era. *JNCI J Natl Cancer Inst*. 2007;99(18):1395-1400.

100. National Cancer Institute Office of Biorepositories and Biospecimen Research. *Summary: National Cancer Institute Biospecimen Best Practices Forum*.; 2007.

101. Khleif SN, Doroshow JH, Hait WN. AACR-FDA-NCI Cancer Biomarkers Collaborative Consensus Report: Advancing the Use of Biomarkers in Cancer Drug Development. *Clin Cancer Res*. 2010;16(13):3299-3318.

102. Masood S, Feng D, Tutuncuoglu O, Fischer G, Bakhshandeh M, Bertholf RL, Wolfson D. Diagnostic value of imprint cytology during image-guided core biopsy in improving breast health care. *Ann Clin Lab Sci*. 2011;41(1):8-13.

103. Jacobs TW, Silverman JF, Schroeder B, Raza S, Baum JK, Schnitt SJ. Accuracy of Touch Imprint Cytology of Image-Directed Breast Core Needle Biopsies. *Acta Cytol*. 1999;43(2):169-174.

104. Yang C, Humphrey PA. False-Negative Histopathologic Diagnosis of Prostatic Adenocarcinoma. *Arch Pathol Lab Med*. 2020;144(3):326-334.

105. Mannweiler S, Pummer K, Auprich M, Galle G, Méhes G, Ratschek M, Tsybrovskyy O, Moinfar F. Diagnostic Yield of Touch Imprint Cytology of Prostate Core Needle Biopsies. *Pathol Oncol Res*. 2009;15(1):97-101.

106. Tong LCB, Rudomina D, Rekhtman N, Lin O. Impact of touch preparations on core needle biopsies. *Cancer Cytopathol*. 2014;122(11):851-854.

107. Rekhtman N, Kazi S, Yao J, Dogan S, Yannes A, Lin O, Silk M, Silk T, Durack JC.

Depletion of Core Needle Biopsy Cellularity and DNA Content as a Result of Vigorous Touch Preparations. *Arch Pathol Lab Med*. 2015;139(7):907-912.

108. Epstein JI, ed. *The Gleason Grading System. A Complete Guide for Pathologists and Clinicians*. Wolters Kluver Health | Lipincott Williams & Wilkins; 2013.

109. van Royen ME, Verhoef EI, Kweldam CF, van Cappellen WA, Kremers GJ, Houtsmuller AB, van Leenders GJLH. Three-dimensional microscopic analysis of clinical prostate specimens. *Histopathology*. 2016;69(6):985-992.

110. Turkbey B, Rosenkrantz AB, Haider MA, Padhani AR, Villeirs G, Macura KJ, Tempany CM, Choyke PL, Cornud F, Margolis DJ, Thoeny HC, Verma S, Barentsz J, Weinreb JC. Prostate Imaging Reporting and Data System Version 2.1: 2019 Update of Prostate Imaging Reporting and Data System Version 2. *Eur Urol*. 2019;76(3):340-351.

111. Rocco B, Chiara M, Sandri M, Spandri V, Cimadamore A, Volavsek M, Mazzucchelli R, Lopez-beltran A, Eissa A, Bertoni L, Azzoni P, Reggiani L, Maiorana A, Puliatti S, Micali S, Paterlini M, Iseppi A, Rocco F, Pellacani G, Chester J, Bianchi G, Montironi R. Digital Biopsy with Fluorescence Confocal Microscope for Effective Real-time Diagnosis of Prostate Cancer : A Prospective , Comparative Study. *Eur Urol Oncol*. Published online 2020:1-8.

112. Marenco J, Calatrava A, Casanova J, Claps F, Mascaros J, Wong A, Barrios M, Martin I, Rubio J. Evaluation of Fluorescent Confocal Microscopy for Intraoperative Analysis of Prostate Biopsy Cores. *Eur Urol Focus*. Published online 2020:9-14.

113. Lopez-Beltran A, Mikuz G, Luque RJ, Mazzucchelli R, Montironi R. Current practice of Gleason grading of prostate carcinoma. *Virchows Arch*. 2006;448(2):111-118.

114. Reder NP, Glaser AK, McCarty EF, Chen Y, True LD, Liu JTC. Open-Top Light-Sheet Microscopy Image Atlas of Prostate Core Needle Biopsies. *Arch Pathol Lab Med*. 2019;143(9):1069-1075.

115. Verhoef EI, van Cappellen WA, Slotman JA, Kremers G-J, Ewing-Graham PC, Houtsmuller AB, van Royen ME, van Leenders GJLH. Three-dimensional analysis reveals two major architectural subgroups of prostate cancer growth patterns. *Mod Pathol*. 2019;32(7):1032-1041.

116. Norton JM, Ketchum CJ, Narva AS, Star RA, Rodgers GP. Complementary Initiatives from the NIDDK to Advance Kidney Health. *Clin J Am Soc Nephrol*. 2017;12(9):1544-1547.

117. Gipson PE, Gipson DS. Focal segmental glomerulosclerosis. In: *Nephrology Secrets*. Vol 12. Elsevier; 2012:212-216.

118. Korbet S. Primary Focal Glomeruloscierosis. *J Am Soc Nephrol*. 1998;9:1333-1340.

119. Schachter AD. Computational simulation of renal biopsy accuracy in focal segmental glomerulosclerosis. *Pediatr Nephrol*. 2006;21(7):953-957.

120. Fogo A, Glick AD, Horn SL, Horn RG. Is focal segmental glomerulosclerosis really focal? Distribution of lesions in adults and children. *Kidney Int*. 1995;47(6):1690-1696.

121. Irfan Warraich AK. ANCA Associated Glomerulonephritis- An In-Depth Review. *J Nephrol Ther*. 2014;04(01):1-13.

122. Iwakiri T, Fujimoto S, Kitagawa K, Furuichi K, Yamahana J, Matsuura Y, Yamashita a, Uezono S, Shimao Y, Hisanaga S, Tokura T, Wada T, Kitamura K, Asada Y. Validation of a newly proposed histopathological classification in Japanese patients with anti-neutrophil

cytoplasmic antibody-associated glomerulonephritis. *BMC Nephrol*. 2013;14(1):125.

123. Bajema IM, Hagen EC, Hansen BE, Hermans J, Noel LH, Waldherr R, Ferrario F, van der Woude FJ, Bruijn JA. The renal histopathology in systemic vasculitis: an international survey study of inter- and intra-observer agreement. *Nephrol Dial Transplant*. 1996;11(10):1989-1995.

124. Restrepo-Escobar M, Granda-Carvajal PA, Jaimes F. Systematic review of the literature on reproducibility of the interpretation of renal biopsy in lupus nephritis. *Lupus*. 2017;26(14):1502-1512.

125. Weening JJ. The Classification of Glomerulonephritis in Systemic Lupus Erythematosus Revisited. *J Am Soc Nephrol*. 2004;15(2):241-250.

126. Wilhelmus S, Alpers CE, Cook HT, Ferrario F, Fogo AB, Haas M, Joh K, Noël L-H, Seshan S V., Bruijn JA, Bajema IM. The Revisited Classification of GN in SLE at 10 Years: Time to Re-Evaluate Histopathologic Lesions. *J Am Soc Nephrol*. 2015;26(12):2938-2946.

127. Ward A, Rosen DM, Law CC, Rosen S, Faulkner-Jones BE. Oxalate nephropathy: a three-dimensional view. *Kidney Int*. 2015;88(4):919.

128. Roberts N, Magee D, Song Y, Brabazon K, Shires M, Crellin D, Orsi NM, Quirke R, Quirke P, Treanor D. Toward Routine Use of 3D Histopathology as a Research Tool. *Am J Pathol*. 2012;180(5):1835-1842.

129. Brändle K. A new method for aligning histological serial sections for three-dimensional reconstruction. *Comput Biomed Res*. 1989;22(1):52-62.

130. Clarke GM, Eidt S, Sun L, Mawdsley G, Zubovits JT, Yaffe MJ. Whole-specimen

histopathology: a method to produce whole-mount breast serial sections for 3-D digital histopathology imaging. *Histopathology*. 2007;50(2):232-242.

131. Puelles VG, Fleck D, Ortz L, Papadouri S, Strieder T, Böhner AMC, van der Wolde JW, Vogt M, Saritas T, Kuppe C, Fuss A, Menzel S, Klinkhammer BM, Müller-Newen G, Heymann F, Decker L, Braun F, Kretz O, Huber TB, Susaki EA, Ueda HR, Boor P, Floege J, Kramann R, Kurts C, Bertram JF, Spehr M, Nikolic-Paterson DJ, Moeller MJ. Novel 3D analysis using optical tissue clearing documents the evolution of murine rapidly progressive glomerulonephritis. *Kidney Int*. 2019;96(2):505-516.

132. Hasegawa S, Susaki EA, Tanaka T, Komaba H, Wada T, Fukagawa M, Ueda HR, Nangaku M. Comprehensive three-dimensional analysis (CUBIC-kidney) visualizes abnormal renal sympathetic nerves after ischemia/reperfusion injury. *Kidney Int*. 2019;96(1):129-138.

133. Torres R, Velazquez H, Chang JJ, Levene MJ, Moeckel G, Desir G V, Safirstein R. Three-Dimensional Morphology by Multiphoton Microscopy with Clearing in a Model of Cisplatin-Induced CKD. *J Am Soc Nephrol*. 2016;27(4):1102-1112.

134. Puelles VG, Moeller MJ, Bertram JF. We can see clearly now: optical clearing and kidney morphometrics. *Curr Opin Nephrol Hypertens*. 2017;26(3):179-186.

135. Dent JA, Polson AG, Klymkowsky MW. A whole-mount immunocytochemical analysis of the expression of the intermediate filament protein vimentin in Xenopus. *Development*. 1989;105(1):61-74.

136. Olson E, Levene MJ, Torres R. Multiphoton Microscopy with Clearing for Renal Pathology. 2016;2016:4-6.

137. Rosenberg AZ, Palmer M, Merlino L, Troost JP, Gasim A, Bagnasco S, Avila-Casado C, Johnstone D, Hodgin JB, Conway C, Gillespie BW, Nast CC, Barisoni L, Hewitt SM. The application of digital pathology to improve accuracy in glomerular enumeration in renal biopsies. *PLoS One*. 2016;11(6):1-12.